

X-ray Spectroscopic and Timing Studies of Galactic Black Hole Binaries

by

Jon Matthew Miller

A.B., The University of Pennsylvania (1997)

Submitted to the Department of Physics
in partial fulfillment of the requirements for the degree of

Doctor of Philosophy in Physics

at the

MASSACHUSETTS INSTITUTE OF TECHNOLOGY

[September 2002]

June 2002

ARCHIVES

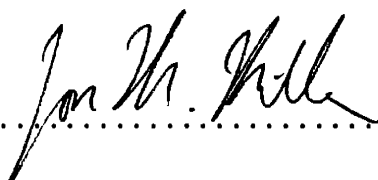
MASSACHUSETTS INSTITUTE
OF TECHNOLOGY

MAY 05 2003

LIBRARIES

© Jon Matthew Miller, MMII. All rights reserved.

The author hereby grants to MIT permission to reproduce and
distribute publicly paper and electronic copies of this thesis document
in whole or in part.

Author 

Department of Physics

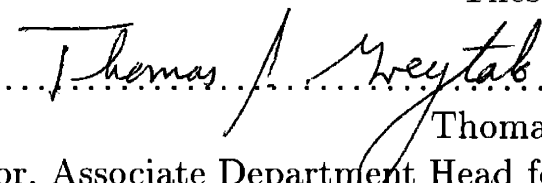
June 24, 2002

Certified by...  7/12/02

Walter H. G. Lewin

Professor

Thesis Supervisor

Accepted by 

Thomas J. Greytak

Chairman, Professor, Associate Department Head for Education

RECEIVED

RECEIVED
MAY 20 1964
RECEIVED

X-ray Spectroscopic and Timing Studies of Galactic Black Hole Binaries

by

Jon Matthew Miller

Submitted to the Department of Physics
on June 24, 2002, in partial fulfillment of the
requirements for the degree of
Doctor of Philosophy in Physics

Abstract

In rare cases, optical observations of Galactic binary star systems which are bright in the X-ray portion of the electromagnetic spectrum dynamically constrain the mass of one component to be well above theoretical limits for a neutron star. These systems — and systems with similar X-ray properties — are classified as black hole binaries. In this thesis, I report on observations of black hole binaries made with satellite observatories in the X-ray band. The region closest to the black hole is revealed in X-rays due to the viscous heating of matter that is accreted from the companion star. X-ray observations of these systems may therefore reveal General Relativistic effects. A fundamental and testable prediction of General Relativity is that matter may orbit more closely around black holes with significant angular momentum. I have investigated the possibility of black hole “spin” and the geometry of accretion flows in these systems using X-ray continuum spectroscopy, fast variability studies, and the shape of iron fluorescent emission lines in this band. I present evidence for black hole spin in XTE J1550–564, XTE J1650–500, and XTE J1748–248. Spin is not required by high-resolution spectral analysis of the archetypical Galactic black hole — Cygnus X-1 — but a thermal accretion disk plus hot corona geometry is confirmed. Studies of XTE J1118+480 and GRS 1758–258 at low X-ray luminosity reveal that models for radiatively-inefficient accretion do not satisfactorily describe the geometry in these systems.

Thesis Supervisor: Walter H. G. Lewin
Title: Professor

0.1 Acknowledgments

Mentors, colleagues, and friends have all supported and aided me in my years at MIT.

First, I wish to thank my advisor, Walter H. G. Lewin, for providing me with advice and mentoring, with exciting new data to work on, and with a variety of freedoms not normally afforded to graduate students. I think he has also imparted to me some “killing instinct” as he calls it, and also the sense that one needs to stay on the cutting edge. I look forward to continuing to work together in the future. On a more personal note, I am especially thankful that Walter held onto his faith in my abilities (especially because I was largely unproven at the time) despite my repeated failures in the MIT general exam process as a junior graduate student.

Within the Lewin group, I am indebted to Derek Fox as a mentor and a friend. It was Derek who guided my first analysis project and helped me to learn the ropes for the first time (and the second, and third, and Nth). David Pooley has been a strong friend and colleague within this group. I am grateful for his copious scientific and computing help, and hope that I return as much as I get.

If a fourth person could sign this thesis, it should be Rudy Wijnands, who came to MIT (from Amsterdam) for three years as a Chandra Fellow. Rudy taught me how to quickly identify the central result in an analysis, how to drive at it with a sharp focus, and to recognize that any solid result should be published quickly. To date, I think we have published nearly 20 papers together.

Often, I have worked within a large collaboration, and a few of the people involved are deserving of special recognition. Perhaps chief among these is Andrew Fabian, whose scientific guidance and support have helped me tremendously. I aspire to have Andy’s breadth one day. Michiel van der Klis has continually provided guidance as well, and shared his time and insights extremely generously. Tiziana Di Matteo introduced me to reflection models and how Galactic black holes and AGN relate. Phil Charles and Rob Fender have been instrumental in helping me to see beyond X-rays. Bryan Gaensler has acted as a mentor and friend, and I look forward to working with him at the CfA. I am grateful to Herman Marshall and Norbert Schulz for their

patient help with Chandra gratings analysis. Mike Nowak only came to MIT in my last year, but it has been fun working with him already. I am grateful to Claude Canizares, who let me participate in many HETGS group meetings, which proved to be really valuable to me. Many times, Ron Remillard provided solid advice, a second opinion, and other insights. MIT is known for X-ray binaries; Ron is fundamental to that effort, and MIT would do well to recognize that by offering him the permanent position he richly deserves.

Fellow astrograds Michael Malm, Glen Monnelly, Michael Munro, and Mike Pivovarovoff helped me stumble through classes, general exams, analyses, and the exits of several Boston-area bars. Thanks guys!

A number of friends from high school and college kept a smile on my face through the good and the bad of MIT. I cannot compactly express my gratitude fully, but I think they know, and so will just mention them by name. Thanks and cheers to: Kristen Bauza (Mellican), Michael Binetti, James Bruening, Michael Dugan, Jessie Dugan, Steven Guillen, Jason Isadore, Ryan Kniewel, Jane Loman, Marty Mellican, Takashi Murata, Christopher Olechowski, Colleen Olechowski, and Thomas Shin.

Elizabeth Lauritsen was a source of love and support through many general exam failures, and eventual victories. More important than any of the countless ways she helped me through MIT, she made life outside of MIT rich, exciting, and very happy. Thanks, Beth! Thanks is also due to the Lauritsen family for their caring and support.

Finally, I wish to thank my family: my father Jon, my mother Liz, and my sister Kate. My parents gave me opportunities and encouragement that few kids get and it made all the difference for me. My sister is brilliant: if we both stay in science, I know that it's only a matter of time before I will stand in her shadow. But more than that, she's a really caring, sensitive woman, and she was there for me through these years. Thanks, family!

Contents

0.1	Acknowledgments	5
1	Introduction	17
1.1	Accretion Power	17
1.2	Accretion in the Milky Way: X-ray Binaries	19
1.3	Black Hole X-ray Binaries	21
1.3.1	Stellar-mass Black Hole “States”	23
1.3.2	Models for Accretion Flows and State Transitions	25
1.4	Investigating the Accretion Flow Geometry and General Relativity in Galactic Black Holes	27
1.4.1	Quasi-Periodic Oscillations	27
1.4.2	Continuum Spectroscopy	28
1.4.3	Fe $K\alpha$ Line Spectroscopy	29
1.4.4	X-ray “Reflection”	31
1.5	Instrumentation	32
1.5.1	<i>The Rossi X-ray Timing Explorer</i>	32
1.5.2	A Small Digression: Contemporary X-ray Missions	34
1.5.3	<i>The Chandra X-ray Observatory</i>	35
1.5.4	<i>The XMM-Newton X-ray Observatory</i>	36
1.6	Investigation	37
1.7	Bibliography	39
2	<i>RXTE</i> Spectroscopy of XTE J1748–288	41
2.1	Abstract	41

2.2	Introduction	42
2.3	Observations and Spectral Analysis	46
2.3.1	Observations	46
2.3.2	Gain Drift and Response Matrices	46
2.3.3	Calibration via the Crab Nebula	47
2.3.4	PCA Calibration Sources	48
2.3.5	ASCA-measured N_H	48
2.3.6	Fitting Method	49
2.4	Results	50
2.4.1	Continuum Components	50
2.4.2	Line Components	52
2.4.3	Reflection	55
2.5	Discussion	56
2.5.1	The Fe $K\alpha$ Fluorescent Line	56
2.5.2	Disk Reflection and Ionization	57
2.5.3	Implications for Geometry and Accretion Flow	59
2.5.4	Constraints on the BH Mass	62
2.5.5	Comparison to Recent Evidence of Lines in BHXBs	63
2.6	Conclusions	63
2.7	Bibliography	70
3	Fast Quasi-Periodic Variability in the X-ray Lightcurve of the 2000 Outburst of XTE J1550–564	73
3.1	Abstract	73
3.2	Introduction	74
3.3	Observations	76
3.4	Analysis and Results	77
3.5	Discussion	81
3.6	Bibliography	86

4	<i>Chandra</i> and <i>RXTE</i> Spectroscopy of the Galactic Microquasar XTE J1550–564 in Outburst	87
4.1	Abstract	87
4.2	Introduction	88
4.3	Outburst History and Observation	90
4.4	Data Reduction	92
4.4.1	<i>RXTE</i> Modes and Selections	92
4.4.2	<i>Chandra</i> Modes and Selections	93
4.5	Analysis and Results	95
4.5.1	Testing for narrow features.	98
4.6	Discussion	99
4.7	Bibliography	102
5	<i>XMM-Newton</i> Grating Spectroscopy of GRS 1758–258 in a Peculiar Off/Soft State	105
5.1	Abstract	105
5.2	Introduction	106
5.3	Observations and Data Analysis	107
5.4	Results	108
5.5	Discussion	112
5.6	Bibliography	118
6	Extremely Weak Reflection Features in the X-ray Spectrum of XTE J1118+480: Possible Evidence for X-ray-Emitting Jets?	119
6.1	Abstract	119
6.2	Introduction	120
6.3	Observation and Data Reduction	122
6.4	Analysis and Results	123
6.4.1	Fits with a simple power-law	125
6.4.2	Fits with “Pexrav” and “Pexriv”	126
6.4.3	Fits with the “Constant Density Ionized Disc Model”	127

6.5	Discussion	129
6.6	Bibliography	133
7	Resolving the Composite Fe $K\alpha$ Line in the Galactic Black Hole	
	Cygnus X-1 with <i>Chandra</i>	135
7.1	Abstract	135
7.2	Introduction	136
7.3	Observation and Instrumental Configuration	138
7.4	Analysis	141
7.5	Results	143
	7.5.1 The Continuum Spectrum	143
	7.5.2 The Fe $K\alpha$ Line Region	147
7.6	Discussion	150
7.7	Conclusions	153
7.8	Bibliography	156
8	Evidence of Spin and Energy Extraction in a Galactic Black Hole	
	Candidate:	
	The <i>XMM-Newton</i>/EPIC-pn Spectrum of XTE J1650–500	159
8.1	Abstract	160
8.2	Introduction	160
8.3	Observation and Data Reduction	162
8.4	Analysis and Results	163
8.5	Discussion	167
8.6	Bibliography	171
9	Conclusions	173
9.1	The Impact of This Work	173
	9.1.1 General Relativistic Effects Near the Black Hole	173
	9.1.2 Galactic Black Hole Accretion Flow Geometry	175
	9.1.3 Connections Between Galactic Black Holes and AGN	176

9.2	Some Possible Ways Forward	177
9.2.1	Extending Diagnostics to Lower Luminosity	178
9.2.2	High-Resolution X-ray Spectroscopy	179
9.2.3	Reflection	180
9.2.4	Jet-Based X-ray Emission	181
9.2.5	Future X-ray Missions	181
9.3	Bibliography	183

List of Figures

1-1	A “True” Color Image from the <i>Chandra</i> Deep Field North	18
1-2	A Typical Black Hole X-ray Binary System	19
1-3	An Advection-Dominated Accretion Flow Model	24
1-4	The Role of Jets in Galactic Black Holes	25
1-5	Simultaneous Quasi-Periodic Oscillations in GRO J1655–40	27
1-6	A Relativistic Model for Broad Fe K α Emission Lines	30
1-7	X-ray Reflection	31
1-8	The <i>Rossi</i> X-ray Timing Explorer	33
1-9	The <i>Chandra</i> X-ray Observatory	35
1-10	The <i>XMM-Newton</i> X-ray Observatory	37
2-1	Checks on the Instrumental Calibraion	46
2-2	Typical Spectra and Data/Model Profiles from the VHS and LS	51
2-3	Fe K α Emission Line and Reflection Parameters	58
2-4	Data/Model Ratios Across the Outburst	60
3-1	The RXTE/ASM Lightcurve of the 2000 Outburst of XTE J1550–564 . . .	76
3-2	QPO Frequency, RWHM, and RMS Versus Time and Flux	79
3-3	QPO Frequency, FWHM, and RMS Versus Three Hardness Ratios . . .	81
3-4	Simultaneous High Frequency QPOs	83
4-1	The RXTE/ASM Lightcurve of the the 2000 Outburst of XTE J1550–564 .	90
4-2	The <i>Chandra</i> Counts Spectrum of XTE J1550–564 Near the Instru- mental Si Edge	94

4-3	<i>Chandra</i> and <i>RXTE</i> Spectra Fit Jointly and the Data/Model Ratio .	98
4-4	Upper Limits on the Strength of Narrow Emission Lines	100
5-1	The <i>XMM-Newton</i> /RGS Spectra of GRS J1758–258	110
5-2	Upper Limits on the Strength of Narrow Line Features	112
5-3	The <i>XMM-Newton</i> /RGS Lightcurve of GRS 1758–248	113
5-4	Constraints on the Inner Disk Radius and Black Hole Spin	115
6-1	<i>Chandra</i> and <i>RXTE</i> Spectra of XTE J1118+480	124
6-2	The Constant Density Ionized Disk Reflection Model	128
7-1	The <i>RXTE</i> /ASM Lightcurve of Cygnus X-1	139
7-2	The Full <i>Chandra</i> Spectrum of Cygnus X-1	143
7-3	The Spectrum in the Fe K α Line Region	146
7-4	The Data/Model Ratio in the Fe K α Line Region	151
8-1	The Skewed Fe K α Line Profile in XTE J1650–500	169
8-2	A Model for the Skewed Fe K α Line	170
9-1	Evidence for a Relativistic Fe K α Emission Line at Low Source Luminosity	178
9-2	Narrow Absorption Lines in XTE J1650–500	180

List of Tables

2.1	The <i>RXTE</i> /PCA observation log	65
2.2	Spectral Component Paramters of XTE J1748–288	66
2.2	Spectral Component Paramters of XTE J1748–288	67
2.3	Fe $K\alpha$ Emission Line Paramters	68
2.4	Three Methods to R_{in} in the VHS	69
2.5	LS Observations Fit With the Diskline Model	69
3.1	High Frequency QPOs in XTE J1550–564	85
4.1	<i>Chandra</i> and <i>RXTE</i> Observation Log	92
4.2	Joint Spectral Fit Results	96
4.3	Unabsorbed Fluxes Measured in Joint Spectral Fits	97
5.1	The Results of Fits to the RGS Spectra of GRS 1758–258	117
6.1	Observations of XTE J1118+480	122
6.2	The Results of Fits to the XTE J1118+480 Spectra with Reflection Models	129
7.1	Models for the 0.65-10.0 keV Spectrum of Cygnus X-1	155

Chapter 1

Introduction

1.1 Accretion Power

Accretion onto a compact object (a white dwarf, neutron star, or a black hole) is an extremely efficient physical process. For a mass m initially at infinity, the upper bound on the energy released as it falls onto the surface of a white dwarf or neutron star is given by: $\Delta E_{\text{accretion}} = GMm/R_{\text{surface}}$, where G is the gravitational constant, M is the mass of the star, and R_{surface} is the radius of the stellar surface. For a neutron star, $R_{\text{surface}} \sim 10$ km and $M \sim 1.4 M_{\odot}$ are reasonable (Shapiro & Teukolsky 1983), and 10^{20} erg/g may be released (in contrast, the fusion of hydrogen into helium gives approximately only one-twentieth of this yield). The accretion luminosity is just given by: $L_{\text{accretion}} = GM\dot{m}/R_{\text{surface}}$, where \dot{m} is the mass accretion rate. The situation is likely more complicated for black holes: the lack of a solid surface makes it possible for matter to reach the event horizon without releasing all of its accretion energy. An efficiency is added to the luminosity equation for black holes: $L_{\text{accretion}} = \eta \dot{m} c^2$, where $\eta = 0.1$ is typically assumed based on a number of observational results and theoretical arguments (Frank, King, & Raine 1992). The X-ray emission observed in steadily accreting objects is due to viscosity in the accretion flow.

Accretion power is not limited to stellar-mass objects. Compact energy sources are observed in the center of approximately 1–10% of galaxies (Fabian et al. 2000). These are termed active galactic nuclei, or AGN. Observations across the astrophysical



Figure 1-1 A “true” color image from the 1 Msec *Chandra* exposure covering the *Hubble* Deep Field North (Brandt et al. 2001). Red sources are strongest in soft X-rays, green sources strongest in intermediate X-rays, and blue sources strongest in hard X-rays; 370 sources are clearly detected in 450 arcmin².

bandpass, but particularly in X-rays, have established that most AGN are powered by accretion onto a supermassive ($10^6\text{--}9 M_{\odot}$) black hole (see, e.g., Kormendy & Richstone 1995). Recently, *Chandra* observations of the so-called “X-ray background” have revealed that the “background” is actually comprised of discrete sources (see Figure 1-1) — AGN, galaxy clusters, and normal galaxies — clearly establishing the importance and ubiquity of accretion on cosmological scales (Brandt et al. 2001, Giacconi et al. 2002). With deeper surveys and future instruments, the role of accretion on these scales will be revealed even more dramatically.

1.2 Accretion in the Milky Way: X-ray Binaries

More than half of the stars in the Milky Way are found in binary stellar systems. In rare cases, one member of the binary can complete its nuclear burning cycle without destroying the bound system. The stellar endpoint may be white dwarf, neutron star, or black hole, depending on the progenitor mass. Neutron stars and black holes are especially luminous in X-rays as matter accretes from the companion, and are called X-ray binaries (XRBs). At present, approximately 300 such systems are known in the Milky Way. The companion star in most systems is of a low-mass type (with $M \leq 1 M_{\odot}$, the so-called low-mass X-ray binaries or LMXBs), although some systems harbor O, B/B(e), and Wolf-Rayet companions (with $M \simeq 20 M_{\odot}$ or more, the high-mass X-ray binaries or HMXBs).



Figure 1-2 A depiction of the black hole low-mass X-ray binary system GRO J1655–40, drawn to scale based on optical radial velocity measurements (courtesy of Robert Hynes; <http://www.astro.soton.ac.uk/~rih/binsim.html>.) Note the polar outflows; black holes for which discrete radio ejections are observed (sometimes with $v_{jet}/c > 0.9$; for a review, see Fender 2002) are called “microquasars.” The analogy to the supermassive black holes thought to power distant quasars applies to both the black hole mass and the scale of the jets.

Although some sources have been observed in X-rays since the dawn of X-ray astronomy, many XRBs are transients (the majority of transients are LMXBs, see Figure 1-2). These systems are observed to undergo periodic “outbursts” which can

be detected across the astrophysical bandpass. In soft X-rays (e.g., 2–10 keV), a source may suddenly increase in luminosity from a dormant state (“quiescence”) by six orders of magnitude (or more, especially in the case of black hole systems) in only days. Although exact decay light curves may vary, outbursts usually decay exponentially and last for weeks or even months. For neutron star systems, quiescent X-ray luminosities cluster around $L_X \simeq 10^{33} \text{ erg s}^{-1}$; black hole systems may typically be much fainter, with $L_X \simeq 10^{30-31} \text{ erg s}^{-1}$ (Garcia et al. 2001). The disparity may be due to the lack of a solid surface in black hole systems.

In X-rays, the clearest means of identifying an XRB as a neutron star system is the observation of Type-I X-ray bursts (for a review, see Lewin, van Paradijs, & Taam 1995). In systems with low surface magnetic fields (10^{8-9} Gauss, or less), accreted matter may accumulate on the surface, triggering a sudden thermonuclear fusion flash lasting only seconds or minutes but reaching $L_X \simeq 10^{38-39} \text{ erg s}^{-1}$ in soft X-rays. The clearest means of determining that an XRB harbors a black hole is to obtain an optical radial velocity measurement. By observing variations in the wavelength and intensity of an absorption line in the spectrum from the companion star, the mass function may be measured and a lower-limit on the mass of the compact object can be measured. As the theoretical upper-limit for the mass of a neutron star is only $3M_\odot$ (see, e.g., Shapiro & Teukolsky 1983), radial velocity measurements which exceed this value imply that a system harbors a black hole (see, e.g., van Paradijs & McClintock 1995). The nature of the compact object is unknown in many XRBs.

At present, there are 15 XRBs known in the Milky Way for which radial velocity measurements imply a black hole (Orosz 2002). Cygnus X-1 was the first system (Galactic or extra-galactic) to be recognized as harboring a black hole. This determination was based on optical radial velocity curves (Webster & Murdin 1972, Bolton 1972). Later, observations with *UHURU* revealed periods of correlated X-ray and radio intensity (Tananbaum et al. 1972). These periods have come to be known as “states” (for reviews, see Tanaka & Lewin 1995, Homan et al. 2001, Done 2002), each with a set of characteristic X-ray spectral and fast variability properties, and radio and optical properties. If an XRB displays these characteristic states, in the absence

of constraining radial velocity measurements or a known optical counterpart (due to heavy extinction in the Galactic center region, for instance), it may be classified as a black hole candidate (BHC). There are approximately as many BHCs as there are dynamically-constrained black holes.

1.3 Black Hole X-ray Binaries

AGN are the most luminous steady sources of accretion power: soft X-ray luminosities of $L_X \simeq 10^{45-47}$ erg s⁻¹ are typical (Fabian et al. 2000). However, their great distance makes them relatively weak X-ray sources in comparison to Galactic accretors. The peak X-ray luminosity of Galactic black holes is only $L_X \simeq 10^{38-39}$ erg s⁻¹, but their proximity makes them far brighter than AGNs. Thus, Galactic black holes represent accessible laboratories to study black hole physics.

Although the study of accretion flows (particularly across a factor of 10^6 in the mass accretion rate, as inferred in the outbursts observed in transient systems) is interesting unto itself, the most intriguing aspect of these systems may be the simple fact that they harbor a black hole. Black holes are intrinsically simple; they are completely characterized by their mass, angular momentum (or, simply, “spin”), and charge, much like a fundamental particle. In particular, spin can be probed effectively in X-rays as this parameter has a strong effect on the accretion flow geometry. The marginally stable circular orbit around a maximally-spinning black hole (a Kerr metric; $R_{MSCO} = 1 R_g$, where $R_g = GM_{BH}/c^2$) is six times closer to the black hole than around a non-spinning black hole (a Schwarzschild metric; $R_{MSCO} = 6R_g$) black hole. Often, black hole spin is discussed in terms of a dimensionless spin parameter j ($0 \leq j \leq 1$, and $j = cJ/GM_{BH}^2$, where J is angular momentum).

Convincing proof of curved spacetimes and General Relativity is scarce. Certainly, gravitational lenses (for a review, see Narayan 1998) provide proof of strong gravitational effects. On Galactic scales, however, the in-spiral of the Hulse-Taylor binary pulsar due to gravitational radiation (Hulse and Taylor 1975) stands apart as a convincing confirmation of General Relativistic predictions. Therefore, the confirmation

of a Kerr metric in a Galactic black hole system may be regarded as a particularly important goal.

The major obstacle to such efforts is that the instrument for probing General Relativistic effects in Galactic black holes — the accretion flow — may change drastically with the mass accretion rate (\dot{m} — assumed to be traced directly by the soft X-ray luminosity) observed across an outburst. For instance, if the accretion flow at low L_X is radiatively-inefficient and unable to support an accretion disk near to the black hole, we may not expect to observe General Relativistic effects in these regimes. Indeed, magneto-hydro-dynamics is likely to be important at all mass accretion rates, and this may induce a significant degree of chaos and limit the precision with which the accretion flow geometry can be diagnosed.

Despite these complexities, the correlated X-ray and radio intensities, or “states” first observed in Cygnus X-1 (Tananbaum 1972) are observed in *all* black hole binary systems. Indeed, the observation of states is the basis for which systems without a dynamical mass constraint are classified as black hole candidates. States imply that there is a degree of organization to the accretion flow geometry in these systems — apparently, only specific modes and structures are possible at certain mass accretion rates. Theoretical work on understanding the accretion flow geometry in Galactic black hole binaries have focused on these states.

A few basic structures are fundamental elements in most models for accretion flows in Galactic black holes. A soft thermal spectrum is expected from the accretion disk, and this is observed in most accreting systems. Shakura & Sunyaev (1973) have described a model for an optically-thick, geometrically thin disk which is a sum of blackbody components produced in narrow annuli. The temperature varies from a low value near the outer edge to a maximum at the inner edge of the disk. The temperature versus radius relation is a function of M_{BH} , \dot{m} , and in some cases α (a magnetic viscosity parameter).

However, the Shakura-Sunyaev disk model cannot account for the hard X-ray component observed in many spectra. Approximately described by a power-law ($f(E) \sim E^{-\Gamma}$), such spectral components often extend to 100–200 keV in Galac-

tic black holes, and in some cases past 800 keV (Tomsick et al. 1999). Cygnus X-1 has been detected out to 10 MeV (McConnell et al. 2000). The hard component is generally attributed to the Compton-upscattering of disk photons in an optically-thin corona. It is not clear if the corona is a central quasi-spherical volume interior to the disk, mostly interior to the disk but partially overlapping the inner disk regions, or a flattened volume which sandwiches the disk.

Finally, the importance of *outflows* has recently been realized. In bright states of some “microquasar” sources (see Figure 1-2), discrete jet ejections are observed in radio bands with measurable proper motion, implying jet velocities in excess of $0.9c$ (for a review, see Fender 2002). In lower-luminosity states, persistent radio fluxes and spectral indices imply the existence of slower, steady outflows. The nature of each of these fundamental structures may change with the mass accretion rate and with the source state.

1.3.1 Stellar-mass Black Hole “States”

The role of states in Galactic black hole binaries is described in many reviews (Tanaka & Lewin 1995; Homan et al. 2001; Done 2002). Presently, five states are recognized. Approximately in the order in which they might occur in a typical outburst (note: every outburst is unique in important ways), these states are:

- *the Very High State (VHS)* – The X-ray spectrum is a combination of a blackbody ($kT \simeq 0.3\text{--}2.0$ keV), and a power-law ($\Gamma = 2.0\text{--}2.5$). The power density spectrum (PDS) shows either power-law or band-limited (1%–15% rms, with a break at 1–10 Hz) noise. Quasi-periodic oscillations (QPOs) in the X-ray intensity are often observed with frequencies between 1–10 Hz. In some cases, high-frequency QPOs are observed in this state (30–450 Hz). Discrete jet ejections are sometimes observed in this state.
- *the High/Soft State (HS)* – The X-ray spectrum is dominated by the blackbody component ($kT \simeq 0.5\text{--}1.0$ keV); the hard power-law component ($\Gamma \simeq 2.5\text{--}3.0$) is very weak. The noise in the PDS is power-law-like but very weak (2%–3% rms). There is no evidence for jets in this state; indeed radio emission is quenched in this state.
- *the Intermediate State (IS)* – Similar to the VHS, but the overall X-ray lumi-

osity is lower. The identification of a source state as an IS depends partially on first observing the VHS previously. However, following a clear HS, a less-luminous state with a harder spectrum or QPOs may be identified as the IS even if a VHS has not been observed.

- *the Low/Hard State (LS)* – The X-ray spectrum is strongly dominated by a hard power-law ($\Gamma \simeq 1.5\text{--}2.0$). If a blackbody is present, it is very weak and cool ($kT \leq 0.5$ keV). The PDS shows strong, band-limited noise (20%–50% rms) with a break below 1 Hz. Steady outflows or weak jets are implied in this state by radio fluxes and spectral indices.

- *the Quiescent/Off State (QS)* – Active accretion ceases in this state. The spectrum is assumed to be a hard power-law ($\Gamma \simeq 1.5\text{--}2.0$). However, the very low luminosity of this state makes strong constraints on the spectral shape impossible. Similarly, in most cases little or no variability is observed, but upper-limits are not constraining.

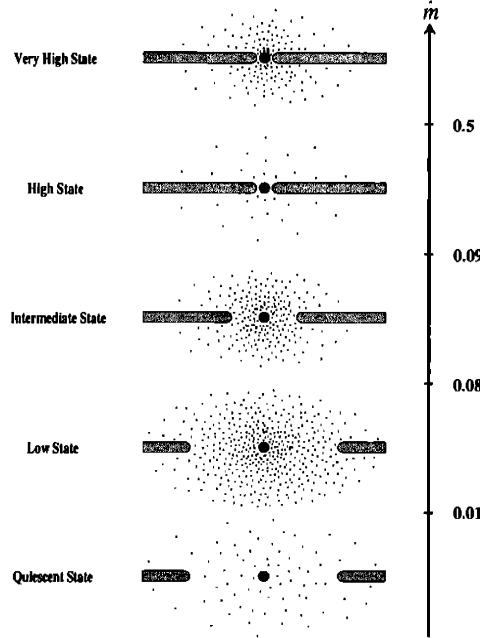


Figure 1-3 The evolution of the accretion flow geometry with \dot{m} (in Eddington units) assumed by an advection-dominated accretion flow model (see text; Esin, McClintock, & Narayan 1997). As \dot{m} (assumed to be traced by the soft X-ray luminosity) falls, the disk recedes radially and is replaced by an optically-thin corona.

Representations of the accretion flow geometries assumed by prevalent models are

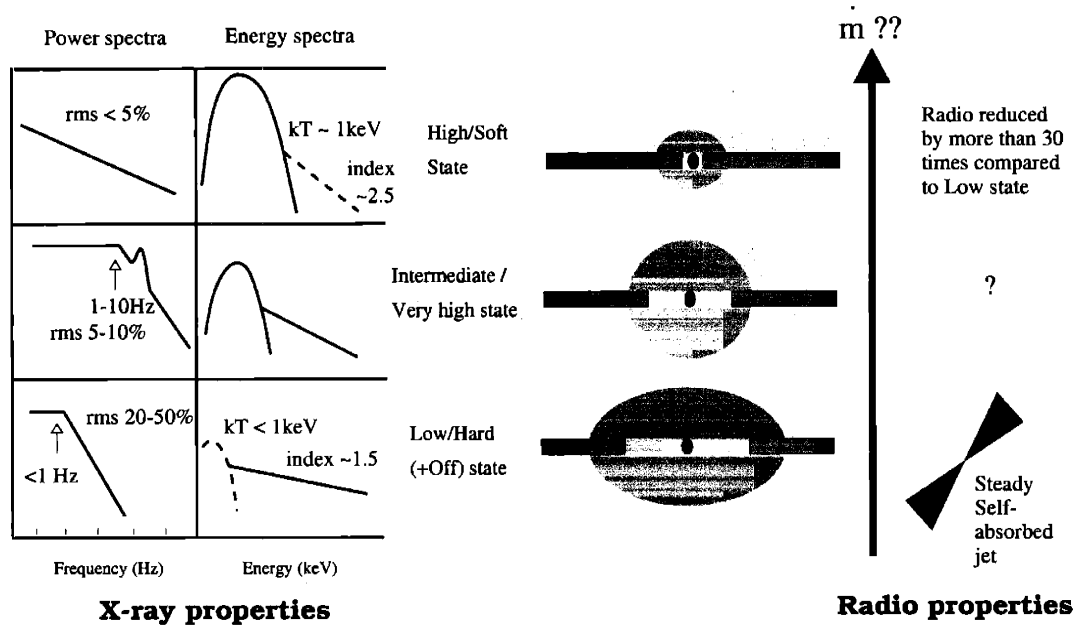


Figure 1-4 A second depiction of X-ray states. At left, the power density spectra and energy spectra associated with black hole states. At right, a schematic which includes the role of jet outflows (Fender 2002).

shown in Figure 1-3 and Figure 1-4.

1.3.2 Models for Accretion Flows and State Transitions

It is possible that at low mass accretion rates, accretion via a Shakura-Sunyaev (1973) disk may not be possible due to inefficient cooling in the flow. Ichimaru (1977) first suggested that the LS of Cygnus X-1 may contain an advection-dominated accretion flow (ADAF), in which accreted matter flows radially onto the black hole before radiating. Narayan & Yi (1994) suggested that ADAFs may be important in AGNs and other settings, and further-developed ADAFs theoretically.

Esin, McClintock, & Narayan (1997) developed a model for the stellar-mass black hole states which relies upon only the mass accretion rate and the ADAF-disk transition radius. This model predicts that at high mass accretion rates (in the VHS,

HS, or IS), the accretion disk may extend inward to the marginally stable circular orbit around the black hole. However, at lower mass accretion rates (in the IS, LS, and QS), the inner disk is replaced with an ADAF; the disk may be truncated at $10^{2-4} R_g$, depending on the accretion rate.

Blandford and Begelman (1999) recognized that matter accreting in an ADAF may become unbound, and escape the system in the form of an outflow or jet. These advection-dominated inflow-outflow solutions (ADIOS) may provide a connection between the observed hard X-ray spectra and outflows (Fender 2002) implied by radio observations in the LS. These models may also apply to AGNs, and in particular to low-luminosity AGN (LLAGN).

Synchrotron emission is very likely the mechanism giving rise to radio emission in outflows and jets in Galactic black holes (Fender 2002). Based partially on the strong observational connection between hard X-ray emission and outflows inferred in radio bands, Markoff, Falcke, & Fender (2001) have proposed that this synchrotron spectrum may extend smoothly from radio bands to X-rays. This may give rise to a hard power-law spectrum. It is not clear if this process may account for all of the hard X-ray emission observed in stellar-mass black holes, but it may account for a significant fraction.

These models may describe the large-scale structures in Galactic black hole accretion flows. However, they do not provide a mechanism for the strong short-term X-ray variability often observed. The viscous timescale in a Shakura-Sunyaev disk is on the order of weeks; very little (if any) variability may be expected from a flow which simply streams onto the black hole (as per ADAF or ADIOS flows). Magnetic flares — either extending above the disk, or connecting the disk and corona, may explain strong short-timescale variability. Beloborodov (1999) has described a model for Cygnus X-1 in which magnetic flares from the disk not only fuel the corona, but may even give rise to outflows and jets. This may suggest an alternative to ADAF and ADIOS models: it is possible that a disk may extend close to the marginally stable orbit at all accretion rates, but that the flaring geometry may change and account for different states.

1.4 Investigating the Accretion Flow Geometry and General Relativity in Galactic Black Holes

Many methods exist for investigating the innermost accretion flow geometry in X-rays in stellar-mass accreting black holes. Among these are continuum X-ray spectroscopy, fast variability studies, broad Fe $K\alpha$ line studies, and high-resolution spectroscopy.

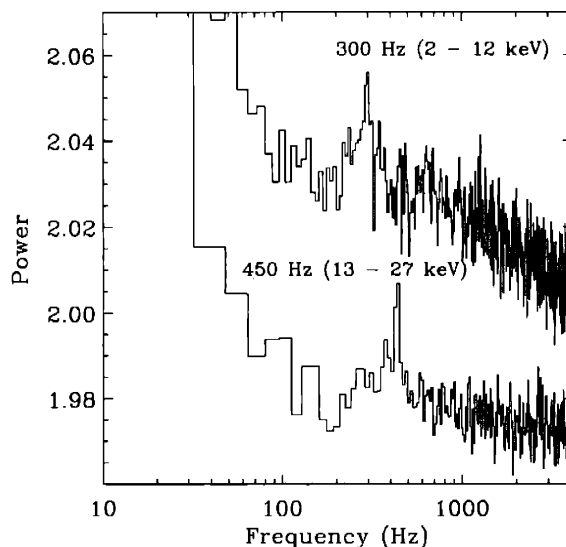


Figure 1-5 Simultaneous high-frequency quasi-periodic oscillations (QPOs) in the Galactic black hole GRO J1655-40 (Strohmayer 2001). The 450 Hz QPO may indicate that the black hole has significant angular momentum.

1.4.1 Quasi-Periodic Oscillations

The Keplerian orbital frequency at the marginally stable circular orbit around a Schwarzschild (non-spinning) black hole is:

$$R_{MSCO} = 6 (GM_{BH}/c^2) \simeq 220 (10 M_{\odot}/M_{BH}) \text{ Hz}.$$

In a handful of black holes, quasi-periodic oscillations (QPOs) with such frequencies are observed in the X-ray lightcurve when source luminosity is high and when a hard

component is a significant fraction of the energy spectrum (see Figure 1-5). These QPOs may plausibly be associated with the inner disk. In systems wherein the mass of the black hole has been constrained via optical radial velocity curves, high-frequency QPOs can be used to constrain the inner radial extent of the accretion disk. If a frequency is observed that is higher than that expected at $R_{in} = 6 R_g$, then the disk may extend closer to the black hole, perhaps indicating black hole spin.

Several models have been proposed to describe QPO frequencies in stellar-mass black holes. Notable among these is the relativistic precession frequency model (RPF; Stella, Vietri, & Morsink 1999). The RPF model explains QPO frequencies in terms of the Keplerian frequency at the inner disk edge, a periastron precession frequency, and a nodal precession frequency (for orbits slightly out of the plane of the disk). This model can reproduce the frequencies observed in some systems, but it is not predictive. Moreover, like other models, in the RPF model it is not clear what physical process might produce the observed modulations.

1.4.2 Continuum Spectroscopy

The multi-color disk blackbody model (MCD; Mitsuda et al. 1984) is based on the Shakura-Sunyaev accretion disk model. The normalization of this modified blackbody distribution gives a measure of the inner accretion disk radius:

$$N = ((R_{in}/\text{km})/(D/10 \text{ kpc}))^2 \cos(\theta)$$

where R_{in} is the inner disk extent in km, D is the distance to the source in kpc, and θ is the inclination of the system. Below ~ 10 keV, the energy spectra of stellar-mass black holes can often be fit with an MCD-plus-power-law model, and so this measure of the inner disk extent is common.

In some cases, the inner radius inferred from the MCD model is only a few km,

or less. The marginally stable orbit around a non-spinning black hole goes as

$$R_{MSCO} \simeq 8.7 \text{ km } (M_{BH}/M_{\odot}),$$

so radii less than a few km cannot be physical. Shimura & Takahara (1995) have noted that if Comptonization of the inner disk is accounted for, the inner disk extent may be 2.9 times higher than the value given by the MCD model. Other authors have noted more subtle deficiencies with this model (see, e. g., Merloni, Fabian, & Ross 2000).

The hard component in the energy spectra of stellar-mass black holes can often be modeled with a power-law. This component frequently extends to 200 keV, and may extend to 800 keV or 1 MeV in some cases. Sometimes an exponentially cut-off power-law is required. The hard component likely originates in a hot, optically-thin plasma. The cut-off energy (often near 100 keV) may correspond to the temperature of the electrons in such a corona.

1.4.3 Fe K α Line Spectroscopy

Fe K α emission lines are observed in bright states of some stellar-mass black holes and in many AGNs (Fe I–XXVI K α occur between 6.40–6.97 keV; Kaastra & Mewe 1993). In some cases, the observed profile is very broad, or even skewed and red-shifted. It is likely that these lines are produced by irradiation of the inner disk, and shaped by Doppler shifts and gravitational red-shifts. Although Compton scattering in a disk atmosphere as part of the irradiation process can broaden an emission line, the observed widths often exceed expectations for Compton scattering.

For an intrinsically narrow emission line, approaching and receding emitting material would cause the line to be shifted symmetrically about its neutral energy. However, near to a black hole, matter orbits at a significant fraction of c and Doppler beaming is important. Therefore, the blue-shifted wing of an emission line produced in a disk around a black hole is expected to be stronger than the red-shifted wing.

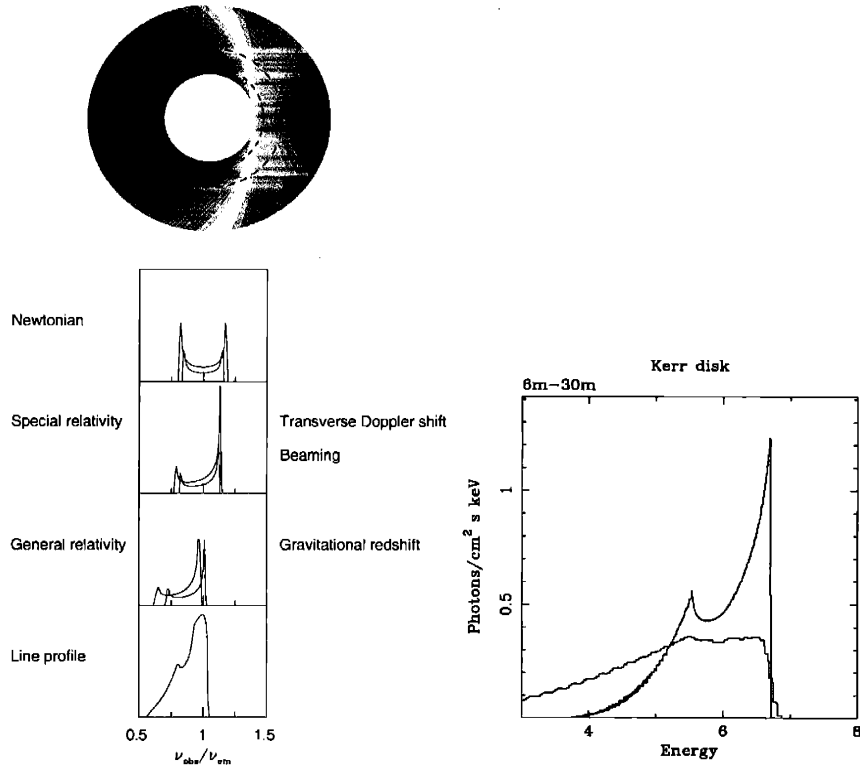


Figure 1-6 An interpretation of the broad Fe $K\alpha$ lines observed in AGN and Galactic black holes. Above left: The inner region of an accretion disk, color-coded to indicate the relative importance of gravitational red-shift and Doppler shifts. Below left: contributions to the broad line profile from various effects for the two radii indicated in the plot above. At right: the double-peaked Fe $K\alpha$ line profile produced in a disk around a non-rotating Schwarzschild black hole (6–30 R_g) and the flattened profile expected for maximally-rotating (1.2–30 R_g) Kerr black hole (Fabian et al. 2000).

The inner part of the accretion disk as a whole sits within the black hole potential well (which is even deeper if the black hole spins); this acts to (red-) shift the overall line profile to a lower energy. The observed line profile is a sum of the lines produced at various radii near to the black hole with varying contributions from gravitational and Doppler shifts (see Figure 1-6).

Fabian et al. (1989) calculated the broad line profiles expected for Schwarzschild geometries, and Laor (1991) calculated the profiles expected from a disk around a Kerr (spinning) black hole. Via these models, one can constrain the ionization state of the inner disk, the inner and outer line-emitting radii (and thereby the spin parameter),

and the inclination of the system.

1.4.4 X-ray “Reflection”

Numerous models have been developed which aim to self-consistently calculate the X-ray spectrum expected for a geometry in which soft seed photons are Compton-upscattered in a hot, optically-thin corona. Many of these models provide a measure of the size of the corona and its optical depth. While these are interesting constraints, such models often fail to account for Fe $K\alpha$ emission lines and trends in the high energy continuum.

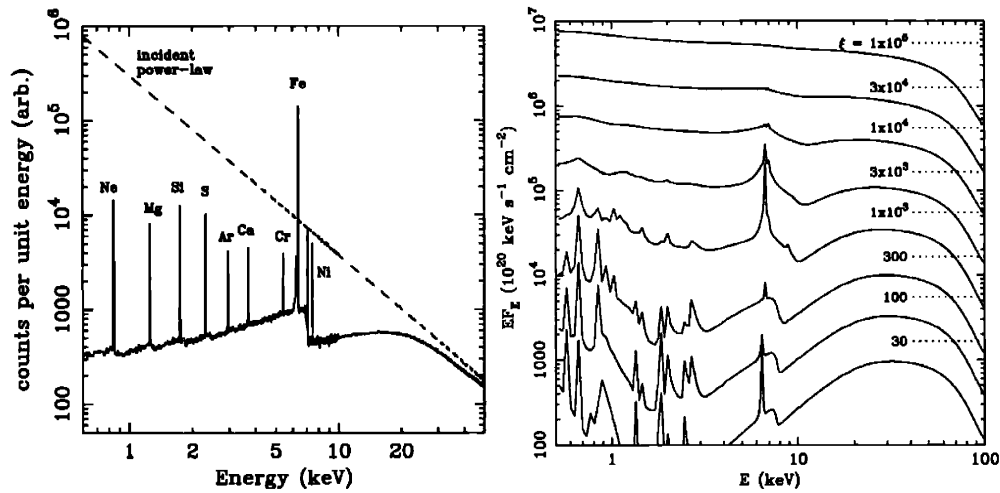


Figure 1-7 X-ray reflection. At left: The spectral response of a neutral accretion disk to irradiation by an incident power-law X-ray spectrum. At right: The response of the disk is sensitive to its ionization state (see text; Fabian et al. 2000).

George & Fabian (1991) realized that Fe $K\alpha$ emission lines and high energy features might arise jointly if the corona irradiates the accretion disk. That is, Fe $K\alpha$ lines may be but a part of the larger spectral signature of an irradiated accretion disk; the other prominent feature is the “Compton hump,” which is actually due to the Compton-backscattering of incident hard X-rays. The total irradiation and reprocessing scheme is known as “X-ray reflection,” and many models have been developed to describe the accretion flow geometry implied by this process (see Figure 1-7).

The most sophisticated reflection models can constrain the inner extent of the accretion disk (important for measuring black hole spin), the spectral index of an

irradiating source (assuming a power-law or cut-off power-law), the geometry of the irradiating source (discrete and central, quasi-spherical and central, or distributed above the disk as a pancake), and the ionization state of the disk (the ionization parameter is defined via $\xi = L_X/nR^2$, where L_X is the X-ray luminosity, n is the hydrogen number density, and R is radius). Thus, such models can be powerful tools for diagnosing the accretion flow geometry in stellar-mass black holes.

1.5 Instrumentation

At the time of writing, a number of X-ray observatories are available that make it possible to approach the study of Galactic black holes from different angles. It must be noted that this is likely to be a very special epoch in the study of these systems, due to the variety of instrumentation available to observers. In the sections that follow, the instrumentation aboard the observatories used to obtain data are described briefly.

1.5.1 *The Rossi X-ray Timing Explorer*

The *Rossi X-ray Timing Explorer* (*RXTE*, see Figure 1-8) was launched on December 30, 1995. This instrument is optimized for timing studies and broad-band spectroscopy at moderate resolution. It has the largest collecting area of any X-ray satellite yet launched. The pointed instruments have a large field of view (the FWHM is one degree); the monitoring instrument covers approximately 80% of the sky every orbit. *RXTE* has opened-up the timescales expected for Keplerian orbits in the innermost regions of accreting Galactic systems.

The *RXTE* All-Sky Monitor (ASM; Levine et al. 1996) consists of three wide-angle shadow cameras with position-sensitive Xenon proportional counters. The total collecting area is 90 cm². Every 90 minutes, 80% of the sky is observed with the ASM, with a sensitivity of 30 mCrab in the 1.5–12 keV band. Although the positional sensitivity of this instrument is coarse ($3' \times 15'$), it has proven essential for monitoring both bright Galactic sources and AGNs. The incredible database of observations

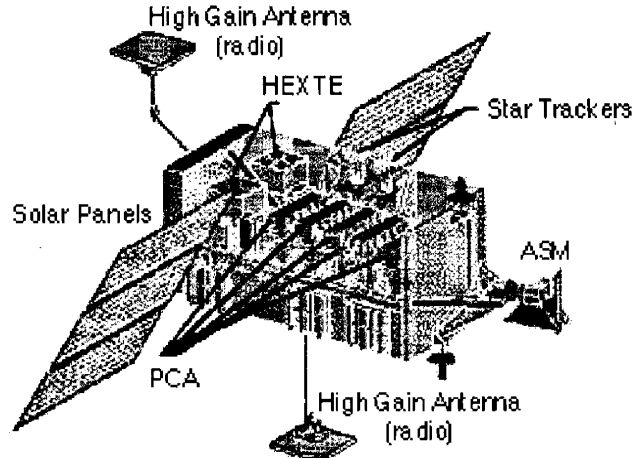


Figure 1-8 An artist's conception of *RXTE* in flight (NASA/GSFC HEASARC).

made with this instrument will likely be important for many years after the end of this mission.

The Proportional Counter Array (PCA; Jahoda et al. 1996) consists of five counters with a total collecting area of 6500 cm^2 in the 2–60 keV band. Each proportional counter unit (PCU) has 4 layers (1 propane veto, 3 xenon), and achieves a maximum time resolution of $\sim 1 \mu\text{s}$. The sensitivity of this instrument is 0.1 mCrab with a background of 2 mCrab (2–60 keV). The energy resolution of the PCA is $\leq 18\%$ at 6 keV. Throughout the lifetime of the PCA, the gain has drifted and it has occasionally been necessary to adjust the gain to account for this effect (some of the papers in this thesis refer to “gain epochs” – each has a slightly different instrumental response function). At the time of writing (April–May 2002), the effective lower energy range of the PCA is 2.5–3.0 keV.

The *RXTE* High Energy X-ray Timing Experiment (HEXTE; Rothschild et al. 1998) covers the 15–250 keV bandpass with $8 \mu\text{s}$ time resolution. Two clusters of 4 NaI/CsI scintillation counters are combined for a total effective area of 1600 cm^2 . In this energy range, 1 Crab is equivalent to 360 counts/s/cluster; the background is 50 counts/s/cluster.

1.5.2 A Small Digression: Contemporary X-ray Missions

Analysis of data from these missions is not presented in this thesis. However, as the papers in this work refer to results from these missions, it is worth noting their relative strengths and characteristics.

In many ways, the Dutch–Italian *BeppoSAX* satellite (1996–2002; Boella et al. 1997) has functioned as a counterpart to *RXTE*. Although the timing capabilities of *BeppoSAX* are inferior to *RXTE*, it has a complementary energy range (0.1–200 keV), which is useful for checking broad-band spectroscopic results. Moreover, *BeppoSAX* carries two semi-focused instruments at low energies and the resolution at 6 keV is 8% — nearly three times better than *RXTE*. The *BeppoSAX* Wide Field Cameras (WFCs) have functioned in the same way as the *RXTE*/ASM.

The German *Roentgensatellit* (or *ROSAT*; 1991–1999; Trumper et al. 1991) was built for X-ray imaging. The spatial resolution of the Position-Sensitive Proportional Counter (PSPC) offered a much-improved look at pulsar nebulae and supernova remnants in X-rays, revealing them dramatically. The *ROSAT* Bright Source Catalog will remain a useful tool for years to come. The imaging capacity of *ROSAT* makes it a precursor to *Chandra*.

The Japanese–American Advanced Satellite for Cosmology and Astrophysics (or *ASCA*; 1993–2000; Tanaka, Inoue, & Holt 1994) was the first focusing X-ray observatory with charge-coupled devices (CCDs) in the focal plane. The Solid-state Imaging Spectrometer (or SIS) provided high spectral resolution (number) at 6 keV. Unfortunately, pointing restrictions imposed by the orbit chosen for *ASCA*, limited the number of Galactic transients observed. CCDs are read-out at a fixed rate; a count rate that is too high makes it impossible for the instrument to distinguish between detecting one photon of energy $N \times E$ or N photons of energy E within the exposure time window. This made it impossible to observe many bright Galactic sources with the SIS, although many AGNs were observed to great effect. Although *ASCA* had imaging capabilities it is identified with the spectroscopic results it obtained from observations of AGNs. In this sense it was a precursor to *XMM-Newton*.

1.5.3 The Chandra X-ray Observatory

Originally designated the Advanced X-ray Astrophysics Facility and renamed for Subramanyan Chandrasekhar, *Chandra* (see, e.g., Weisskopf et al. 2002) launched on July 23, 1999. It consists of a single Wolter type-I X-ray telescope with 4 nested mirror shells. The High Resolution Mirror Assembly (HRMA) produces images of exquisite arcsecond resolution and sub-arcsecond positional accuracy. Either one of two X-ray detectors may be inserted into the focal plane:

The High Resolution Camera (HRC) consists of two micro-channel plates and offers better positional sensitivity than its counterpart instrument but only crude spectral information. It was not used for any analysis presented in this thesis and will not be discussed further.

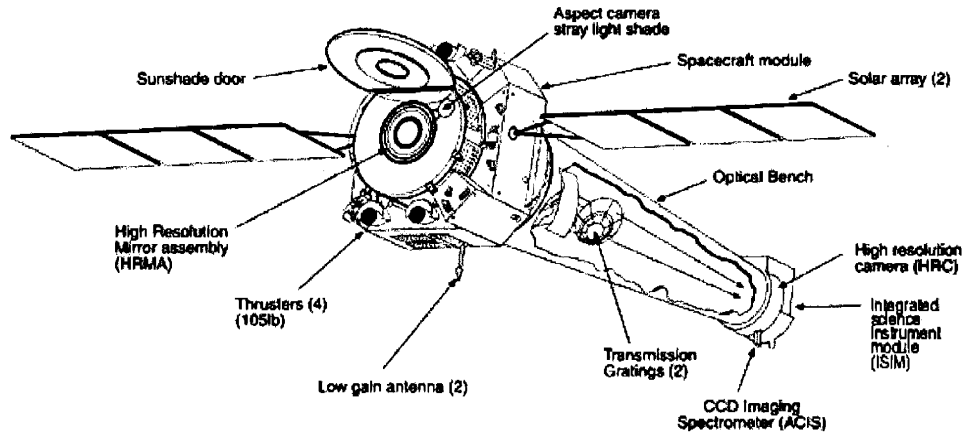


Figure 1-9 A schematic of the *Chandra* X-ray Observatory (NASA/CXC).

The Advanced CCD Imaging Spectrometer (ACIS) offers sub-arcsecond positional sensitivity and excellent spectral resolution in the 0.3–10.0 keV band. The ACIS-I (Imaging) array consists of 4 front-side-illuminated CCDs arranged in a square and is optimized for imaging surveys. The ACIS-S (Spectroscopy) array consists of 4 front-side-illuminated and 2 back-side-illuminated CCDs arranged in a row. The back-side-illuminated CCDs offer improved sensitivity at low energies. A variety of sub-arrays can be used with the ACIS arrays to obtain shorter frame-times. In continuous-clocking (CC) mode, spectral information is collapsed into one dimension

and the framerate is reduced to 2.8 ms. The effective area of the ACIS CCDs peaks between 1–2 keV.

Either one of two dispersive gratings may be inserted in front of the X-ray detectors. The work reported in this thesis made use of the ACIS-S detector to read-out dispersed spectra. With the ACIS-S array, the Low Energy Transmission Grating Spectrometer (LETGS) offers a uniform resolution of 0.05 Å across the 1.2–65 Å (0.2–10 keV) bandpass. The High Energy Transmission Grating Spectrometer (HETGS) consists of the Medium Energy Gratings (MEG; 2.5–31 Å or 0.4–5.0 keV) and the High Energy Gratings (HEG; 1.2–15 Å, or 0.8–10.0 keV). The MEG and HEG offer uniform resolutions of 0.01 Å and 0.005 Å, respectively, across their bandpass.

1.5.4 *The XMM-Newton X-ray Observatory*

Originally designated the X-ray Multi-Mirror mission, and later named for Isaac Newton, *XMM-Newton* (see Figure 1-10 ; Jansen et al. 2001) was launched on 10 December, 1999. It consists of three Wolter type-I X-ray telescopes, with different instruments at their foci. A 30 cm optical/UV telescope with a CCD at its focal plane (called the Optical Monitor) also flies aboard *XMM-Newton*, but was not used in any analysis presented in this thesis. This observatory offers good spatial resolution (there are 58 nested mirror shells; the FWHM of the PSF is 6”), but it is its large collecting area (4650 cm²) in total, the most of any focusing X-ray observatory yet flown).

Each of the X-ray telescopes has a 30’ field of view. In two of the three telescopes, a Metal Oxide Semi-conductor (MOS; Turner et al. 2001) CCD camera sits at the focus, and in the other a “pn” (Studer et al. 2001) camera sits at the focus. The cameras are known as the European Photon Imaging Cameras (and therefore as the EPIC-MOS and EPIC-pn cameras). Each camera has moderate spectral resolution ($E/\Delta E \sim 20 - 50$) in the 0.15–15 keV band. The MOS cameras are optimized for imaging large fields. The pn camera is optimized for brighter sources and can operate in several modes with short read-out times (though information is read-out in only one dimension in “timing” and “burst” mode). In “timing” mode the CCD framerate

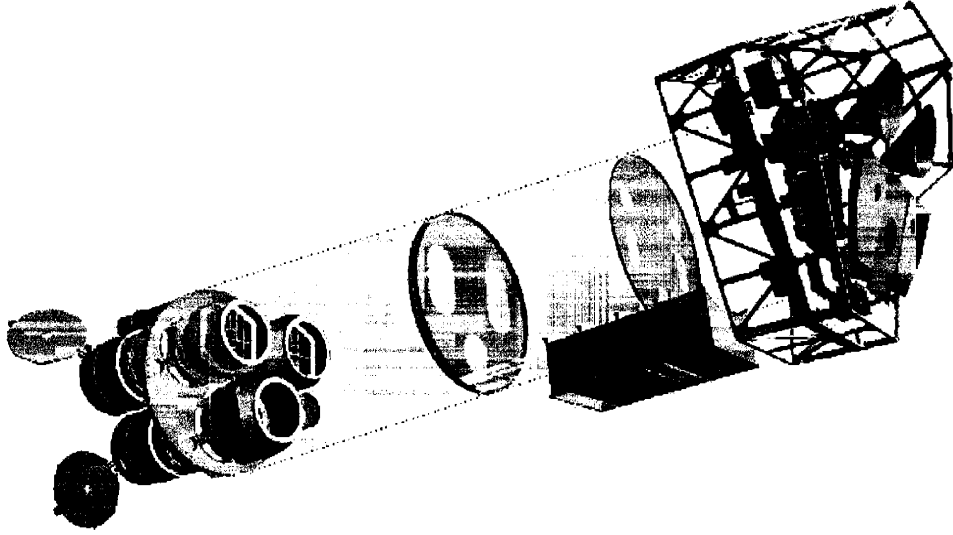


Figure 1-10 A schematic of the *XMM-Newton* X-ray Observatory (Jansen et al. 2001). To the left: the three mirror modules; to the right: the focal plane instruments.

is 0.03 ms; the frametime in “burst” mode is 0.007 ms but the duty cycle is only $\sim 3\%$. The effective area of each camera is approximately 1550 cm^{-2} , and peaks in the 1–2 keV band.

In the telescopes with MOS cameras at the focus, half of the incident light is intercepted by a Reflection Grating Spectrometer (RGS; den Herder et al. 2001). The dispersed spectrum is read-out by a separate series of MOS CCDs. This instrument disperses photons in the 5–38 Å range (0.35–2.5 keV) with a resolution of $\lambda/\Delta\lambda \sim 100 - 800$ in this range. This range contains a number of the K and/or L-shell transitions from C, N, O, Ne, Mg, Si, S, Ca, and Fe. The effective area of each RGS unit (140 cm^2) peaks at 15 Å.

1.6 Investigation

The following chapters describe efforts to investigate evidence for black hole spin and the geometry of low-luminosity accretion flows using the diagnostic tools and instruments described in the preceding sections. They are presented chronologically from the time each analysis was first undertaken to demonstrate the evolution and progress within the field over a three-year period (1999–2002). Three Galactic black

holes (XTE J1118+480, XTE J1550–564, and Cygnus X-1) and three black hole candidates (XTE J1650–500, XTE J1748–288, and GRS 1758–258) are considered. In XTE J1550–564 (see Chapter 3), QPOs are found in the X-ray lightcurve which suggest black hole spin. Investigations of the Fe $K\alpha$ emission line profiles revealed in spectra of XTE J1748–288 and XTE J1650–500 suggest black hole primaries with near-maximal spin parameters (see Chapter 2 and Chapter 8, respectively). Continuum spectroscopy of the accretion disk and a broad Fe $K\alpha$ emission line found in an intermediate-luminosity state of Cygnus X-1 both constrain the disk to remain close to the black hole; this stands in contrast to the geometry predicted by ADAF models (see Chapter 7). Similarly, disk spectroscopy suggests an ADAF geometry is unlikely to hold in a low-luminosity state of GRS 1758–258 (see Chapter 5). Reflection modeling of the spectrum of XTE J1118+480 suggests that jet outflows may contribute to the X-ray spectrum (see Chapter 6), a theoretical possibility which is only beginning to be addressed.

1.7 Bibliography

- Blandford, R. D., and Begelman, M. C., 1999, MNRAS, 303L, 1
- Beloborodov, A. M., 1999, ApJ, 510L, 123
- Boella, G., Butler, R. C., Perola, G. C., Piro, L., Scarsi, L., & Bleeker, J., 1997, A & AS, 122, 299
- Bolton, C. T., 1972, Nature, 235, 271
- Brandt, W. N., et al., 2001, AJ, 122, 2810
- Burke, B. E., et al., 1997, IEEE Trans. on Electron Devices, 44, 1633
- Done, C., 2002, in "Philosophical Transactions of the Royal Society," Series A: Mathematical, Physical, and Engineering Sciences, astro-ph/0203246
- Esin, A. A., McClintock, J. E., & Narayan, R., 1997, ApJ, 489, 865
- Fabian, A. C., Rees, M. J., Stella, L., and White, N. E., 1989, MNRAS, 238, 729
- Fabian, A. C., Iwasawa, K., Reynolds, C. S., and Young, A. J., 2000, PASP, 112, 1145
- Fender, R. P., 2002, in Lecture Notes in Physics 589, "Relativistic Flows in Astrophysics," ed. A. W. Guthmann et al. (New York: Springer), in press
- Frank, J., King, A., and Raine, D., 1992, Cambridge, UK: Cambridge University Press
- Garcia, M. R., McClintock, J. E., Narayan, R., Callanan, P., Barret, D., and Murray, S. S., 2001, ApJ, 553L, 47
- George, I. M., and Fabian, A. C., 1991, MNRAS, 249, 352
- Giacconi, R., et al., 2002, ApJS, 139, 369
- den Herder, J. W., et al., 2001, A & A, 365L, 7
- Homan, J., et al., 2001, ApJS, 132, 377
- Hulse, R. A., and Taylor, J. H., 1957, ApJ, 195L, 51
- Ichimaru, S., 1977, ApJ, 214, 840
- Jahoda, K., Swank, J. H., Giles, A. B., Stark, M. J., Strohmayer, T., Zhang, W., & Morgan, E. H., 1996, Proc. SPIE, 2808, 59
- Jansen, F., et al., 2001, A & A, 365L, 1
- Kaastra, J. S., and Mewe, R., 1993, A & AS, 97, 443
- van der Klis, M., et al., 1996, IAU Circ. 6319
- Kormendy, J., and Richstone, D., 1995, ARA & A, 33, 581
- Laor, A., 1991, ApJ, 376, 90
- Levine, A. M., Bradt, H., Cui, W., Jernigan, J. G., Morgan, E. H., Remillard, R. A., Shirey, R. E., & Smith, D. A., 1996, ApJ, 469, L33
- Lewin, W. H. G., van Paradijs, J., and Taam, R. E., 1995, in "X-Ray Binaries," ed. W. H. G. Lewin, J. van Paradijs, & E. P. J. van den Heuvel (Cambridge, UK: Cambridge University Press)
- Markoff, S., Falcke, H., and Fender, R., 2001, A & A, 372L, 25
- McConnell, M. L., et al., 2000, ApJ, 543, 928
- Merloni, A., Fabian, A. C., and Ross, R. R., 2000, MNRAS, 313, 193
- Miller, J. M., et al., 2001, ApJ, 563, 928
- Mitsuda, K., et al., 1984, PASJ, 36, 741
- Narayan, R., and Yi, I., 1994, ApJ, 428L, 13
- Narayan, R., 1998, NewAR, 42, 73

- Orosz, J., 2002, list of dynamically-constrained black holes available at:
<http://www.astro.uu.nl/~orosz/>
- van Paradijs, J., & McClintock, J. E., 1995, in "X-Ray Binaries," ed. W. H. G. Lewin, J. van Paradijs, & E. P. J. van den Heuvel (Cambridge, UK: Cambridge University Press)
- Rothschild, R. E., et al., 1998, *ApJ*, 496, 538
- Shakura, N. I., and Sunyaev, R. A., 1973, *A & A*, 24, 337
- Shapiro, S., & Teukolsky, S., 1983, "Black Holes, White Dwarfs, and Neutron Stars" (New York: Wiley)
- Shimura, T., & Takahara, F., 1995, *ApJ*, 445, 780
- Stella, L., Vietri, M., and Morsink, S. M., 1999, *ApJ*, 524L, 63
- Strohmayer, T. E., 2001a, *ApJ*, 552, L49
- Strohmayer, T. E., 2001b, *AdSpR*, 28, 511
- Studer, L., et al., 2001, *A & A*, 365L, 18
- Tanaka, Y., Inoue, H., & Holt, S. S., 1994, *PASJ*, 46, L37
- Tanaka, Y., and Lewin, W. H. G., 1995, in "X-Ray Binaries," ed. W. H. G. Lewin, J. van Paradijs, & E. P. J. van den Heuvel (Cambridge, UK: Cambridge University Press)
- Tananbaum, H., Gursky, H., Kellogg, E., Giacconi, R., and Jones, C., 1972, *ApJ*, 177L, 5
- Tomsick, J. A., Kaaret, P., Koreger, R. A., & Remillard, R. A., 1999, *ApJ*, 512, 892
- Trumper, J., et al., 1991, *Nature*, 349, 579
- Turner, M. J. L., 2001, *A & A*, 365L, 27
- Webster, B. L., and Murdin, P., 1971, *Nature*, 250, 183
- Weisskopf, M. C., Brinkman, B., Canizares, C., Garmire, G., Murray, S., and van Speybroeck, L. P., 2002, *PASP*, 114, 1
- Wijnands, R., and van der Klis, M., 1998, *Nature*, 394, 344

Chapter 2

RXTE Spectroscopy of XTE J1748–288

This chapter is based on the original paper:

“Relativistic Iron Emission and Disk Reflection in Galactic Microquasar XTE J1748-288,” Miller, J., M., Fox, D. W., Di Matteo, T., Wijnands, R., Belloni, T., Pooley, D., Kouveliotou, C., and Lewin, W. H. G., 2001, *The Astrophysical Journal*, Vol. 546, p. 1055,

with the permission of the publisher, *The Astrophysical Journal*.

2.1 Abstract

We report evidence for an Fe K α fluorescence line feature and disk reflection in the Very High, High, and Low State X-ray spectra of the galactic microquasar XTE J1748–288 during its June 1998 outburst. Spectral analyses are made on data gathered throughout the outburst by the *Rossi X-ray Timing Explorer* Proportional Counter Array. Gaussian line, relativistic disk emission line, and ionized disk reflection models are fit to the data. In the Very High State the line profile appears strongly redshifted, consistent with disk emission from the innermost stable orbits around a maximally rotating Kerr black hole. In the High State the line profile is

less redshifted and increasingly prominent. The Low State line profile is very strong (~ 0.5 keV equivalent width) and centered at 6.7 ± 0.10 keV; disk line emission model fits indicate that the inner edge of the disk fluctuates between ~ 20 and $\sim 100 R_g$ in this state. The disk reflection fraction is traced through the outburst; reflection from an ionized disk is preferred in the VHS and HS, and reflection from a relatively neutral disk is preferred in the LS. We discuss the implications of our findings for the binary system dynamics and accretion flow geometry in XTE J1748–288.

2.2 Introduction

Quasars and other Active Galactic Nuclei (AGN) are generally thought to be powered by accretion onto supermassive black holes at the centers of galaxies. They are well-studied across the full astronomical bandpass, from radio to gamma-ray wavelengths. At X-ray energies, attention in recent years has focused on the broad Fe $K\alpha$ fluorescence line seen in many AGN of the Seyfert 1 type (for a recent review, see Fabian et al. 2000). At the high spectral resolutions first achieved with the *ASCA* satellite, the line in these sources is revealed to have a strongly asymmetric profile that is consistent with emission from the innermost radii of a relativistic accretion disk (Tanaka et al. 1995; Mushotzky et al. 1995; Nandra et al. 1997). The theory for the emission mechanism holds that the X-rays originate by inverse-Compton processes acting in a hot corona above a cold (weakly ionized) accretion disk that produces thermal emission in the optical and ultraviolet; thus the theory is bolstered by observations of a reflected continuum above ~ 10 keV that flattens the intrinsic inverse-Compton power-law.

Within our Galaxy, radio and X-ray observations over the course of the past six years have identified a population of X-ray binaries, the galactic microquasars, that are similar to AGN in a number of important respects. First, these sources exhibit relativistic radio-emitting outflows (e.g., Mirabel & Rodriguez 1994) analogous to the megaparsec-scale radio jets of AGN. Second, the sources are thought to harbor black hole primaries: they exhibit the canonical X-ray spectral states of black hole candi-

dates (BHCs; see discussion below), and when dynamical mass estimates have been obtained they have supported this hypothesis (e.g., Orosz & Bailyn 1997). Finally, the sources exhibit strong X-ray variability on a broad range of timescales (hundreds of hertz to hundreds of days), also analogous to AGN. The name “microquasar” refers approximately to the relative mass difference between the two classes of object: the $\sim 10 M_{\odot}$ masses of the microquasars, on the one hand, and the 10^7 – $10^9 M_{\odot}$ masses of AGN, on the other. This relative mass scale in turn is expected to set the relative variability timescale.

In addition to the properties mentioned above, an important common characteristic of the microquasars (without yet an analogue in AGN) are X-ray quasi-periodic oscillations (QPOs) in the 30–300 Hz frequency range. These QPOs have been identified in the sources GRS 1915+105 (Morgan, Remillard, & Greiner 1997), GRO J1655–40 (Remillard 1997), XTE J1550–564 (Remillard 1999), XTE J1748–288 (Fox & Lewin 1998; Revnivtsev, Trudolyubov, & Borozdin 1999), and 4U 1630–47 (Cui et al. 1999a). The phenomenology of these QPOs is remarkably rich and continues to challenge both the observers seeking to characterize them (e.g., Reig et al. 2000; Sobczak et al. 2000), and the theorists seeking to explain them (e.g., DiMatteo & Psaltis 1999; Lehr, Wagoner, & Wilms 2000).

Not surprisingly, the microquasars have also been found to be a rich arena in which to study accretion physics and geometry via X-ray spectral features. *Rossi X-ray Timing Explorer* (*RXTE*; Bradt, Rothschild, & Swank 1993) Proportional Counter Array (PCA; Jahoda et al. 1996) observations of XTE J1550–564 are well-fit by including a Gaussian line feature at 6.5 keV with fixed width of 1.2 keV (FWHM) (Sobczak et al. 1999). Two line features, one at ~ 5.7 keV and one at ~ 7.7 keV, were observed in the 1996 outburst of 4U 1630–47 (Cui, Chen, & Zhang, 1999). The two lines are attributed to Doppler shifting of neutral Fe $K\alpha$ in either a Keplerian accretion disk or bipolar outflow. Balucinska-Church & Church (2000) report likely Fe $K\alpha$ emission from four spectra taken from GRO J1655–40.

XTE J1748–288 was discovered with the *RXTE* All Sky Monitor (ASM; Levine et al. 1996) on 4 June 1998 (Smith et al. 1998). Radio observations undertaken

with the Very Large Array (VLA) revealed an unresolved radio source with position coincident to that of the X-ray source (R.A. 17 : 48 : 05.06, Dec. $-28^{\circ}28'25''8$, J2000; Hjellming et al. 1998a). Subsequent radio observations revealed an extended source, exhibiting components with proper motion of 20–40 mas day $^{-1}$ (Rupen, Hjellming, & Mioduszewski 1998). Based on a 21-cm HI absorption measurement the distance to the source was estimated to be ≥ 8 kpc, implying that the intrinsic velocity of the jet components must be higher than $0.93c$ (Hjellming et al. 1999b). QPOs with centroid frequencies of ~ 0.5 Hz and ~ 32 Hz were reported in the power density spectrum (PDS) from 6 June 1998 (Fox and Lewin, 1998). The combination of relativistic radio jets and X-ray QPOs secured the identification of XTE J1748–288 as a Galactic microquasar. Multiple observations of the source were made with *RXTE* (Revnivtsev, Trudolyubov, & Borozdin 1999) and *ASCA* (Kotani et al. 2000); the source flux decayed below the ASM detection limit in September 1998.

The evolution of black hole X-ray binary (BHXB) outbursts is generally described in terms of several canonical spectral states, distinguished by the relative contribution from low energy and high energy X-rays within the 1–10 keV band. Typically, low energy X-rays (1–2 keV; the soft component) dominate the emission of a BHXB outburst near maximum, and as the outburst evolves the soft component grows weaker. Higher energy X-rays (5–10 keV; the hard component) become stronger and dominate as the overall flux decreases in the late stages of a BHXB outburst.

The canonical BHXB spectral states are the Very High State (VHS), the High or Soft State (HS), the Intermediate State (IS), the Low or Hard State (LS), and the Quiescent State (QS). In the LS, the X-ray spectrum is nearly a pure power-law, with photon index 1.5–2.5, often extending to hundreds of keV (Tanaka & Lewin 1995). In the HS, the 1–10 keV flux is an order of magnitude higher than in the LS due to the addition of a strong soft component. In the VHS the soft component is stronger still and may be accompanied by a substantial hard component; in addition, QPOs are often observed in this state. The IS is a transitional state between the LS and the HS (Mendez & van der Klis, 1997), not observed in all sources. Finally, the QS state is typified again by a non-thermal spectrum, with a flux level several orders of

magnitude below the lowest (LS) outburst flux.

Although the temporal and spectral behavior of BHXBs has been widely studied, the mechanism driving the state transitions is still unknown. The quasi-thermal radiation present in the VHS, HS, and IS is typically modeled as thermal emission from an optically-thick, geometrically-thin, multi-temperature accretion disk (Mitsuda et al. 1984). The power-law component, meanwhile, is generally attributed to inverse-Compton processing of lower-energy disk photons in an optically-thin corona above the accretion disk (Sunyaev & Titarchuk, 1980). If signs of hardening in the spectrum above ~ 10 keV are present and accompanied by a fluorescent Fe $K\alpha$ line, then – much as in AGN – these can be interpreted as the signature of Compton reflection from the cold matter in the disk (George & Fabian 1991).

Reflection features in the LS of BHXBs, however, are generally much less prominent than in AGN (Zycki et al. 1999), so it has been argued that at least in the LS, the geometrically-thin disk does not extend inward to the innermost stable orbit, but is truncated at hundreds or thousands of Schwarzschild radii (Esin et al. 1997). In the HS, the optically thick disk is postulated to move inwards so that the majority of the dissipated energy emerges in the form of a blackbody-like spectrum. Measuring reflection spectra in BHXBs may therefore be helpful in understanding the physical properties of BHXB accretion geometries.

Previous analysis of *RXTE* observations of XTE J1748–288 revealed Fe $K\alpha$ emission in the LS spectra of this source (Revnivtsev, Trudolyubov, & Borozdin 2000). Our fits to the same data revealed a strong LS iron feature, and in addition we found that it was possible to trace the feature backwards into the HS, and even the VHS. Here we present the results of 22 X-ray spectral observations spanning ~ 120 days of the 1998 outburst of XTE J1748–288. We investigate relativistically-skewed emission features and disk reflection in the spectra from this source.

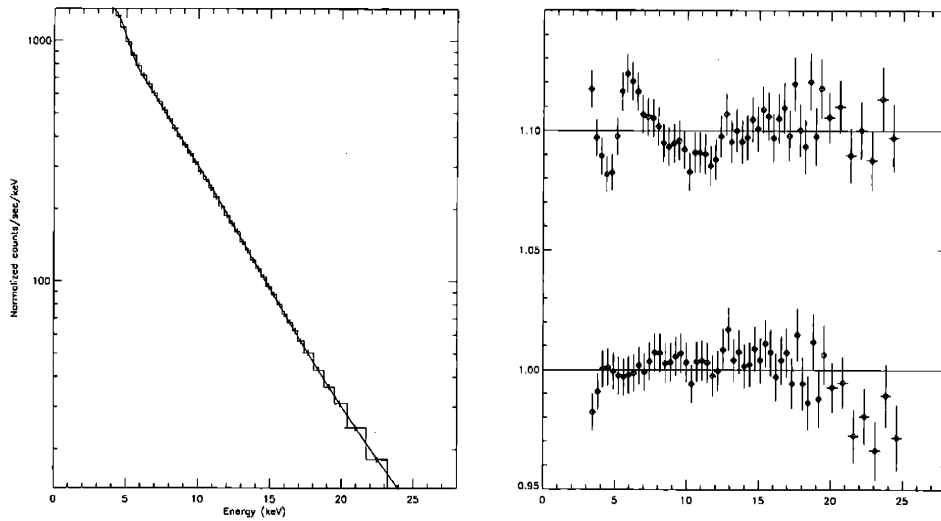


Figure 2-1 Checks on the instrumental calibration. At left: The crab nebula spectrum, observed in May 1998, fitted with a power-law and low-energy absorption. At right, the data/model ratios for fits using pcarsp-generated response matrix (top), and the static PCA response matrix (bottom).

2.3 Observations and Spectral Analysis

2.3.1 Observations

We include all of the publicly-available *RXTE* TOO data between peak bolometric luminosity and quiescence in our analysis. This embodies 22 pointed observations, effectively sampling the different spectral states across the outburst; see Table 2.6 for times and ObsIDs of these observations. The standard FTOOLS v.4.2 package was used to reduce the Standard-2 PCA data from these observations. All observations were dead-time corrected, and the background was calculated using the Very Large Events (or Bright Source) option within PCABACKEST.

2.3.2 Gain Drift and Response Matrices

The *RXTE* PCA instrument (Jahoda et al. 1996) consists of 5 individual proportional-counter detectors, the proportional counter units (PCUs). Due to gas exchange between propane and xenon layers in the detectors, the gain of the individual PCUs drifts. PCUs 0, 1, and 4 have very similar gain drift patterns, and a better overall

performance than PCUs 2 and 3 (Sobczak et al. 1999; Balucinska-Church & Church 2000). We have chosen to fit data from all layers (all propane layers and all xenon layers) of PCUs 0, 1, and 4 simultaneously.

Analysis of the data from an May 1998 observation of the Crab nebula with the response matrices calculated via the Ftool PCARMF (v3.5) shows substantial residual trends. These deviations are thought to represent defects in the response matrices themselves as the Crab is known to have a featureless power-law spectrum. We use response matrices generated by PCA calibration specialist Keith Jahoda that eliminate these residuals. They are available through the Goddard Space Flight Center ftp archive at:

`ftp://lheaftp.gsfc.nasa.gov/pub/keith/response_matrices_v2.2.1_v80.tar.`

A comparison of the data/model ratio using PCARSP-generated and Jahoda-generated (hereafter “static”) response matrices, presented in Figure 2-1, reveals that the static response matrices yield a much cleaner fit to the Crab data in the 3.5–10.0 keV band. For this reason, we use the static response matrices for all spectral fits.

2.3.3 Calibration via the Crab Nebula

We have analyzed every non-slewing observation of the Crab nebula from May to October 1998 to check for variations in the performance of the static response matrices over time.

These Crab fits were used to select an appropriate energy range for precision analysis of the data from XTE J1748–288. The bins between 2.0 and 3.5 keV varied drastically and randomly in fits to these Crab observations: the χ^2 statistic for these bins consistently fell in the range of ~ 40 – 100 . Therefore, we set a lower energy limit of 3.5 keV for our analysis. Above ~ 20 keV, neither type of response matrix satisfactorily fits the Crab. As this energy is high enough to constrain reflection features fit to the data, we fix 20 keV as the upper limit of our fitting range.

The addition of 1% systematic errors has become a standard practice when reducing PCA spectral data (see, e.g., Cui, Chen, & Zhang, 1999; Sobczak et al. 1999). Fits to the set of Crab observations mentioned above with this 1% systematic error

produced artificially low χ^2 values. We find that a systematic error of 0.75% yields fits to the Crab observations with $0.99 < \chi^2/(dof) < 1.0$; we therefore adopt this systematic error value for our fits. This step adds validity to the measures of statistical merit based on $\Delta(\chi^2)$ that we employ in our analysis.

2.3.4 PCA Calibration Sources

Onboard the PCA are several pellets of radioactive Americium, ^{241}Am , that are used for in-flight calibration. Data from these sources is accumulated every 128 seconds and telemetered as part of the Standard1 data. As the line emission energies of the source are precisely known, any drift in the measured energy of the lines over the lifetime of the satellite can be directly attributed to changes in the detector response.

We collected all of the calibration source data from the first (4 June) and last (26 September) days on which XTE J1748–288 was observed; analyzing this data in channel space we find that the centroids and widths of the ^{241}Am lines agree to $<1\%$ and $<2\%$, respectively, for these two days. We therefore expect that the PCA energy scale drift is less than 1% over the time *RXTE* conducted these observations. Assuming a linear scale, this represents a systematic drift of ≤ 0.06 keV for a line feature centered at 6.0 keV.

2.3.5 ASCA-measured N_H

As we determined, the *RXTE* effective sensitivity range does not extend below 3.5 keV during the time of our observations. We therefore rely on *ASCA* observations to measure the column density reliably. Kotani et al. (2000) report $N_H = 9.0 \times 10^{22} \text{ cm}^{-2}$ for a power-law index of $\alpha_{pl} = 2.9$, and N_H at $6.0 \times 10^{22} \text{ cm}^{-2}$ for $\alpha_{pl} = 2.7$, each with an error of approximately $\pm 30\%$. Both of these *ASCA*-measured power-law indices agree with the power-law indices we measure using *RXTE* data. We therefore fix the value of $N_H = 7.5 \times 10^{22} \text{ cm}^{-2}$ for all of our fits.

2.3.6 Fitting Method

Our spectral fits progressed through three increasingly complex spectral models, a process which we illustrate for two representative observations (obs. 3 and 19, from the VHS and LS, respectively) in Figure 2-2.

First, we fit the data with the canonical multicolor blackbody disk plus power-law model (top and second panels in Figure 2-2). The most striking feature in the data/model ratio plots for this model (second panel) is a broad excess between 4 and 7 keV for Obs. 3, and a distinct 6.7 keV line for Obs. 19. Our second model therefore adds one or two Gaussian components to the underlying continuum. In the case of Obs. 19 (and other LS observations), the fit is further improved by addition of a Gaussian at 8 keV; we discuss this feature in more detail below.

Two spectral features are expected to result from the reflection of hot X-rays from an accretion disk: fluorescent line emission, and a broad Compton-upscattering excess often referred to as a “reflection bump.” To be self-consistent, our final model (see Figure 2-2) therefore consists of the multicolor blackbody disk (Diskbb) component, two Gaussians, and a Pexriv component (Magdziarz & Zdziarski 1995). Pexriv incorporates an incident power-law source of photons, and the reflection of these photons off an ionized disk. For all fits with Pexriv, we fix the power-law cutoff energy at 200 keV, and the disk inclination at 45 degrees (as we do for disk line profiles). We report measurements of the disk reflection fraction ($f = \Omega/2\pi$) and ionization ($\xi = L_x/nr^2$). Pexriv reduces to a simple power-law in the absence of reflection.

We report the results of our continuum and Gaussian-line fits in Tables 2.2 and 2.3, respectively.

Models for emission line propagation from a relativistic spacetime generally predict a double-peaked line profile (see, e.g., Dabrowski et al. 1997, Martocchia et al. 2000). Noting that the double-peaked nature of the soft emission excess in the VHS might be due to relativistic skewing, we attempted to fit these spectra with a relativistic line feature, the Laor model from XSPEC (Laor, 1991). This is a general model and may be applied to Kerr geometries but reduces to a Schwarzschild geometry in the

minimal angular momentum limit. In the absence of optical or radio data to constrain the disk inclination angle, we fix this parameter at 45 degrees. In addition, the disk emissivity profile is fixed at r^{-2} , the inner emission radius of the disk to $1.235 R_g$ (as for a nearly-maximally rotating Kerr black hole), and the outer emission radius to $50.0 R_g$. The gravitational radius R_g is GMc^{-2} , where G is Newton’s gravitational constant, M is the mass of the compact object, and c is the speed of light (R_g is half of the Schwarzschild radius). Measurements of the inner disk radius in the VHS are reported in Table 2.4.

In the LS, models for accretion flow around black holes (Esin et al. 1997) suggest that the inner edge of the accretion disk does not extend as far inwards as in the VHS. Measurements of the inner disk radius derived from the normalization of the multicolor blackbody disk component suggest the same phenomenology. It follows that emission from the inner disk regions in the LS would not suffer the same degree of relativistic skewing. Thus, an additional fit is made to LS spectra with a model consisting of the “Diskline” line emission model within XSPEC (Fabian et al. 1989) and Pexriv. For these fits, we fix the disk emission profile to r^{-2} and the disk inclination to 45 degrees; and the outer disk radius to $10^4 R_g$. We fit for inner disk radius, line centroid energy, and the component normalization. The results of fits using this model are reported in Table 2.5.

2.4 Results

2.4.1 Continuum Components

The total 3.5–20.0 keV flux measured using our models peaks at $11.4 \times 10^{-9} \text{ erg cm}^{-2} \text{ s}^{-1}$ between outburst days 2 and 8, and is dominated by the hard power-law component. The soft multicolor disk blackbody flux is slightly less than half of the hard power-law flux in observations 3 and 4, but a smaller fraction in observations 5–8 (see Table 2.2). The normalization of the blackbody disk component is tightly constrained in this state, and is relatively constant. These relative flux measurements and very high

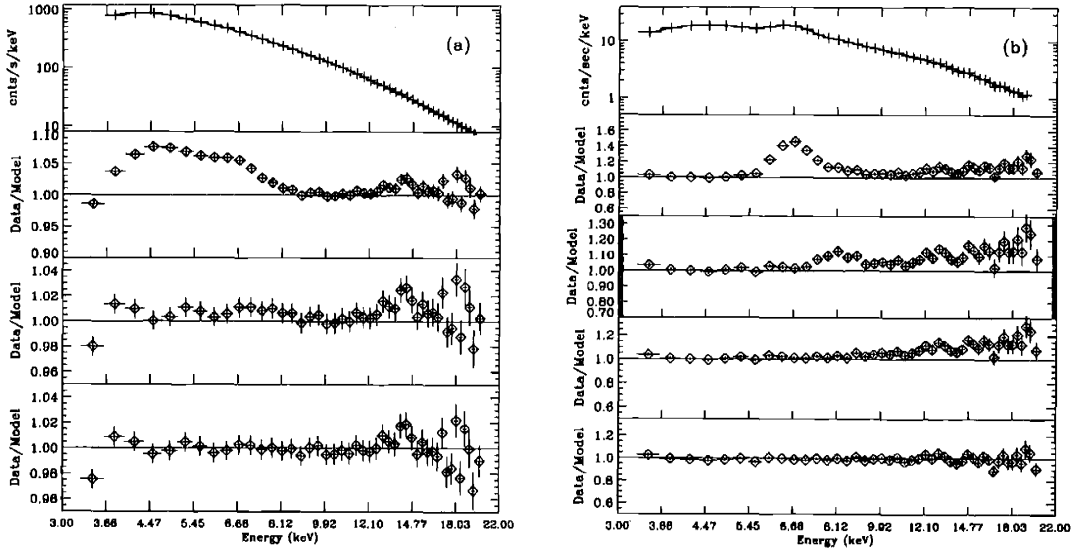


Figure 2-2 Typical spectra and data/model profiles from the VHS and LS. (a) Observation 3 (VHS). The top plot shows the spectrum for Observation 3, fit with a blackbody disk + 2 Gaussians + Pexriv model. The plots below are data/model ratio plots. Second from top, dbb + plaw; notice the double line peaks and the reflection above 10 keV. The third plot is the ratio for a model consisting of dbb + 2 Gaussians + plaw; the lines are fit well but the reflection is not. Finally, at bottom, the ratio for a model consisting of dbb + two gs + pexriv; this model fits the lines and continuum very well. (b) Observation 19 (LS). The top plot shows the spectrum for Observation 19, fit with a 2 Gaussians plus Pexriv model. The plots below are data/model ratio plots. Second from top, p-law; notice the very strong, broadened line and reflection. The third plot is the ratio for a model consisting of a Gaussian + plaw; the lines is fit well, but a higher energy line remains. Fourth, the ratio for a model with 2 g's + plaw; this is a good fit. At bottom, the ratio for a model consisting of two g's + reflection via pexriv.

overall flux level signify that XTE J1748–288 is in the VHS during observations 3–8. The disk blackbody temperature is well-measured, and decreases very slightly through this state, from 1.57 to 1.26 keV. The normalization of the hard power-law component is well-constrained; the spectral index hardens through the VHS (see Table 2.2, Figure 2-3).

Between observations 8 and 9, the hard power-law flux falls and the 3.5–20.0 keV spectrum becomes dominated by the soft component. The multicolor blackbody disk flux increases by a factor of ~ 4 between these observations. We interpret this change in continuum component flux as the VHS to HS transition. The blackbody disk temperature decreases from 1.29 to 0.91 keV through this state (see Table 2). The

normalization of the soft component peaks mid-way through the HS, dipping most dramatically in observation 15, just prior to the HS–LS transition. The power-law spectral index is softer than in the VHS at the beginning of the HS, but the index steadily hardens through the HS. Whereas the soft blackbody disk normalization peaks mid-way through this state, the hard power-law component normalization falls steadily throughout (see Table 2.2).

The multicolor blackbody disk temperature falls by half between observations 15 and 16, and the soft flux is nearly extinguished. This marks the HS to LS transition. Ginga observations of GS 1124–68 (Ebisawa et al. 1994) and GS 2023+338 (Zycki et al. 1999) yield LS disk temperatures of ~ 0.3 keV. We measure a disk component with similarly low temperature in observations 16, 17, and 18, but find no evidence of a disk flux in subsequent observations. It is therefore possible that the disk cools to a temperature well below the range of sensitivity of the PCA. The power-law spectral index is uniformly harder ($1.86 \leq \alpha_{pl,LS} \leq 2.08$) in the LS than in any observation in the VHS or HS. The normalization of the power-law component decreases throughout the LS, as does the overall flux. The power-law index measured with Pexriv hardens steadily, slightly increasing in the last two observations (see Table 2.2, Figure 2-3).

The multicolor blackbody disk model yields an inner accretion disk radius, with component normalization, source distance, and disk inclination as parameters. Fits with this model indicate that the inner disk radius is relatively constant at ~ 10 km in the VHS, and ~ 19 km for every observation made in the HS.

2.4.2 Line Components

Figure 2-4 shows the data/model ratios for the VHS and HS, and LS, respectively. The ratios are off-set from each other, but on the same relative scale. The models used here are the multicolor blackbody disk plus Pexriv for the VHS and HS, and Pexriv only for the LS. These figures serve to illustrate how the equivalent width, width, and centroid energy of the line features detailed in Table 2.3 vary across the outburst.

The bottom data/model ratio plot in Figure 2-4 corresponds to observation 23,

just before the source slipped beneath RXTE detection limits. The line feature is very strong, broadened, and single-peaked. Tracing backwards to the beginning of the LS (top of Figure 2-4), it is readily apparent that the line centroid energy is approximately constant, and the equivalent width is diminished in earlier observations. The width of the line feature is measured to be ~ 0.30 keV throughout, indicating that the line is resolved by the PCA in the LS (see Table 2.3).

The resolved line in the LS allows for tightly-constrained measurements via fits with the Diskline model. Centroid energy values fall within ± 0.1 keV of 6.7 keV, and the line equivalent width increases steadily from $\sim 200 \pm 20$ eV to $\sim 916 \pm 33$ eV. These measurements are in good agreement with the values obtained by fitting the line with a Gaussian profile. Most notably, the Diskline model measures the inner edge of the accretion disk, which remains relatively close to the innermost radius in the LS. Our fits indicate the inner edge of the disk is moving closer to the BH in observations 16, 17, and 18, from $63_{-31}^{+933} R_g$ to $\sim 6_0^{+15} R_g$. The inner edge then recedes back to $102_{-63}^{+140} R_g$ in observation 19. Following this sharp recession, we measure the inner disk radius to move steadily inward in subsequent observations, to $\sim 35_{-15}^{+34} R_g$ in observation 23.

Fits to the LS are improved by adding a higher-energy Gaussian line component to the spectral model at ~ 8.3 keV. This unresolved line feature is suggested at $>68\%$ confidence throughout the LS, and is consistent with fluorescent Ni $K\alpha$ emission from a highly-ionized species. The equivalent width of this line varies between 10–260 eV from observation 16 to observation 23. The presence of this line feature is visible in Figure 2-2 once the more intense line at ~ 6.7 keV has been fit, but is not visible in the plots in Figure 2-4 as it is far less intense than the lower energy line.

Following the data/model ratio from the beginning of the LS (top of the right panel in Figure 2-4) to the end of the HS (bottom of the left panel in Figure 2-4), the ~ 6.7 keV line feature is still very prominent, and can in fact be traced all the way back to the VHS (top of the left panel in Figure 2-4). Although the line feature is much weaker in the VHS than in the HS or LS, the constancy of the centroid energy and smooth evolution of the equivalent width clearly tie the line emission feature near

~6.7 keV in the HS and VHS to that in the LS.

A lower-energy line feature is present in the HS that is not seen in the LS. We distinguish these HS and VHS features as the “red” and “blue” lines. Fitting a model including two Gaussian lines to the HS, we find that the blue line feature is significant at greater than 90% confidence in all but one observation in the HS (obs. 10). The centroid energy of the blue line slowly increases from 6.4 to 6.7 keV from the beginning to the end of the HS. The equivalent width also increases steadily, from 39 to 347 eV (see Table 2.2, Figure 2-3). The red line is not significant at 90% confidence in obs. 10, but is measured in the three observations at the beginning of the HS.

Again tracing backwards in time (bottom to top) in the left panel of Figure 2-4, the rising equivalent width of the red component and the smeared profiles of both red and blue line features is clearly seen. In the VHS the line emission feature may be characterized as smeared and possibly double-peaked. Fits to the VHS spectra with a model including two Gaussian line emission features find the red line is significant at >99.9% confidence for every observation. The blue line is significant at >99.9% in all but obs. 6. Generally, the equivalent width and flux of the red line are greater than that of the blue line in the VHS.

The red line centroid energy decreases slightly through the VHS, but is consistent with 4.6 keV (see Figure 2-3). The centroid energy of the blue line varies in the VHS, steadily increasing from 5.8 to 6.6 keV (see Table 2.3). The red line width is inconsistent with zero in the VHS except in observations 3 and 6; the blue line except in observation 7. The red line is likely at the limit of the PCA resolution in the VHS; it is unresolved in the HS. The blue line is especially broad (0.8 keV) at the beginning of the VHS, becoming narrower throughout (to 0.4 keV in obs. 8).

Fits with the Laor relativistically-skewed line emission model show that the addition of a line feature emitted from a region between $1.2 R_g$ and $30.0 R_g$, with centroid energy of 5.7 keV, is significant at 90% confidence in observations 3, 4, and 8. Later observations cannot be fit as well with the Laor model. Indeed, we do not expect that the resolution of the PCA is sufficient to constrain Laor model parameters; fits with this model serve primarily as a consistency check.

The continuity of the changes in line parameters and profiles as we search backwards from the LS to the VHS indicates that the line-like excesses seen in Figure 2-4 are very likely manifestations of the same line emission feature.

Tracing the line feature(s) backwards in time from the LS, the equivalent width is observed to steadily decrease. It is important to note that the flux in the red line feature in the VHS is greater than the flux in the single-peaked/blue line feature in the LS (see Table 2.3). Considering the states separately, the flux of the lines is highest at the beginning of each spectral state, and gradually decreases throughout (see Table 2.3, Figure 2-3). More generally, the lines have the highest flux in the VHS at the beginning of the outburst. The line profile is possibly double-peaked in the VHS. As the outburst moves into the HS, the line profile becomes single-peaked and increases in equivalent width, though the line flux decreases steadily. Finally, as the outburst moves into the LS, the line equivalent width becomes very large (the soft blackbody disk continuum component disappears) and the line flux continues to decrease steadily.

Revnivtsev, Trudolyubov, & Borozdin (1999) only find evidence for a line component in the LS spectrum of XTE J1748–288, and suggest that the line is from diffuse galactic emission as the line flux is stable relative to the decline in the power-law flux. We disagree with this interpretation. Our finding that the line flux is highest at the beginning of each spectral state and decays until the end of the state demands that the spectral lines are produced by XTE J1748–288.

2.4.3 Reflection

The power-law continuum component *Pexriv* models the reflection of hot X-rays impinging on an ionized, optically-thick gas, often assumed to be an accretion disk. In the VHS, the reflection fraction f is small but non-zero at >90% confidence (except obs. 6; see Table 2.2, Figure 2-3). Measurements indicate that the disk is very ionized at the beginning of the VHS ($\xi \sim 7000$ in obs. 3). The ionization is constrained only in observations 3, 4, and 5. Thereafter in the VHS, and throughout the LS, the ionization is not tightly constrained but a highly-ionized disk is preferred at 90%

confidence. We therefore fixed the ionization ($\xi = 2000$) in fitting observations 6–15.

Across the VHS–HS transition, f varies discontinuously from ~ 0.04 in observation 8 to ~ 0.01 in observation 9. Throughout the HS, f increases to a value of ~ 0.11 in obs. 15. Perhaps due to the dominance of the soft component in the HS, f is consistent with no reflection throughout.

The reflection fraction f again varies sharply across the HS–LS transition, from ~ 0.11 in observation 15 to 0.45 ± 0.02 in observation 17. The value of f falls sharply in subsequent observations, to ~ 0.04 in observation 21, and becomes consistent with zero in obs. 23 (see Table 2.2, Figure 2-3). Measurements of ξ in the LS are consistent with a neutral disk, marking a sharp contrast to the highly-ionized disk required in the VHS and HS.

2.5 Discussion

2.5.1 The Fe $K\alpha$ Fluorescent Line

Based on the broadened, redshifted line emission profile observed by Iwasawa et al. in MCG–6-30-15 (1997), and on the profiles and equivalent widths calculated by many researchers (e.g. Magdziarz & Zdziarski 1995, Fabian et al. 1989, George & Fabian 1991, Dabrowski et al. 1997, Martocchia et al. 2000), we interpret the red and blue line features in the VHS of XTE J1748–288 as wings of a Doppler- and gravitationally-shifted Fe $K\alpha$ line emission profile. The line profiles (Figures 2-2 and 2-4; Table 2.3) are consistent with those calculated by Martocchia et al. (2000) for emission from the innermost region of an accretion disk orbiting a BH of high angular momentum, viewed at a modest inclination angle, with a source of hot X-rays located $\leq 10 R_g$ above the BH. The equivalent widths measured in the VHS are broadly consistent with those predicted by the model for a disk with outer emission radius near $100 R_g$, and viewed at an angle slightly below the 45 degree inclination we assumed.

Our fits to the VHS using the Laor model indicate that in this spectral state the

relativistically-skewed line is consistent with emission from an inner radius extending down to the marginally stable orbit for a maximally rotating Kerr black hole, $1.2 R_g$ (see Table 2.4), in obs. 3 and obs. 4. Measurements of the inner disk radius via the multicolor blackbody disk model in the VHS confirm that the disk may extend to the innermost stable orbit in a Kerr geometry.

Throughout the HS, the red wing of the profile becomes less prominent, and the blue wing strengthens. In particular, the centroid energy of the blue line shifts from 5.8 keV (beginning of the VHS) to 6.7 keV (end of the HS). Throughout the LS, the line profile is single-peaked, and measured at 6.70 ± 0.10 keV. This value is consistent with highly ionized species of iron. We suggest that this line is likely a complex of lithium-like, helium-like, and hydrogenic iron species (Fe XXIV-XXVI). The shift of line profile to higher centroid energies may be produced in two ways, either by an evolving ratio of iron ionizations contributing to the line profile, or by the disk mildly recessing from the BH. Given the inner disk radii we measure (see Table 2.2) across the outburst and the high ionization preferred in the VHS and HS, it is likely that the latter process dominates, but both may contribute.

Although unlikely given the relatively continuous evolution of the line profile (in contrast to the discontinuous nature of the jet, which is only reported in the VHS), it is nevertheless possible that the lines originate within the jet itself. It is also possible that the lines are produced within a hot coronal region, and the measured reflection is from a cold geometry apart from the disk.

2.5.2 Disk Reflection and Ionization

The reflection fractions we measure in the VHS and HS are smaller than the same parameter measured in observations of other BHXBs and AGN. Done, Madejski, & Zycki (2000) measure f between 0.55–1.25 in Seyfert 1 galaxy IC4329a. Zycki, Done, & Smith (1998) measure $f \sim 0.30$ in the VHS, and $f \sim 0.64$ in the HS of the 1991 outburst of GS 1124–68. Zycki et al. (1999) measure $f \sim 0.4 - 0.9$ during the decline of GS 2023+338 (this source was dominated by the hard power-law component through its decline, unlike XTE J1748–288 and GS 1124–68). The reflection fraction

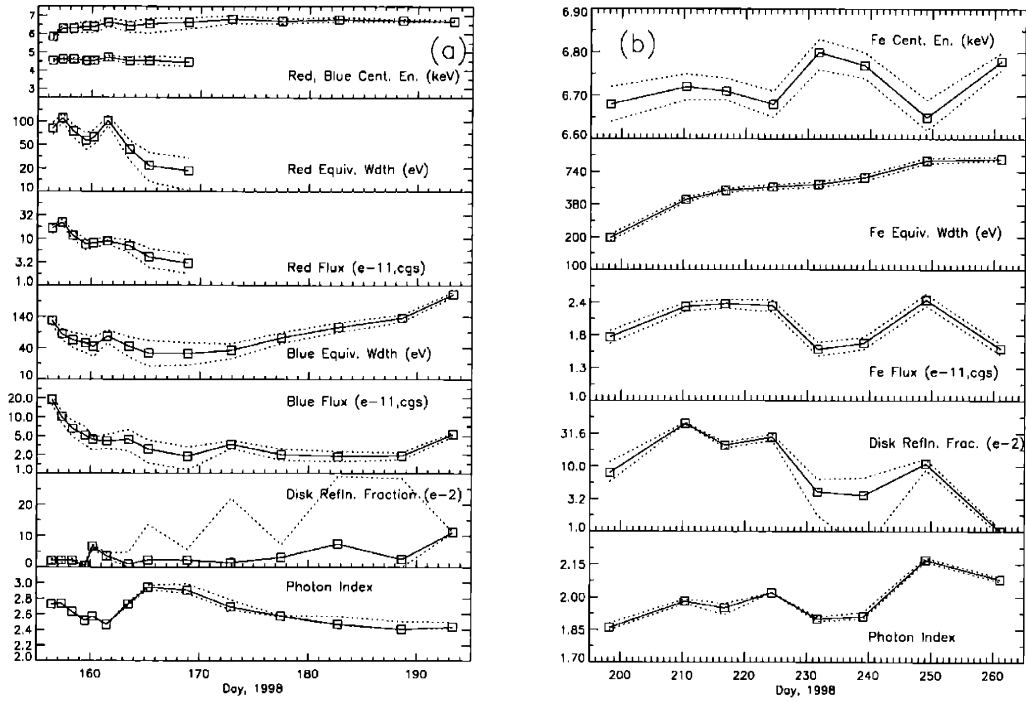


Figure 2-3 Line and Reflection Parameters. Measured values are connected by a continuous line, and 90% confidence limits by dotted lines. (a) VHS and HS. Top to bottom: red and blue wing centroid energy (top); red wing equivalent width; red wing flux; blue line equivalent width; blue wing flux; disk reflection fraction; and power-law photon index (bottom); vs Day of Outburst (days from 3.8 June 1998). The disk ionization parameter is high throughout the VHS and HS; $\xi \geq 2.0 \times 10^3$. (b) LS. Top to bottom: Fe $K\alpha$ centroid energy (top); Fe $K\alpha$ equivalent width; Fe $K\alpha$ flux; disk reflection fraction; and power-law photon index (bottom); vs Day of Outburst. The disk ionization parameter is low in the LS; $0 \leq \xi \leq 100$.

measured in the early LS observations of XTE J1748–288 is comparable to that measured in the LS of Cygnus X-1 by Gierlinski et al. (1999) $f_{cyl,LS} \sim 0.5 - 0.7$.

The low reflection fractions we measure are likely due to the high disk ionizations strongly preferred in the VHS and HS. The contrasting high reflection and negligible ionization at the beginning of the LS is not surprising; a similar phenomenology is noted by Zycki, Done, & Smith (1998) for the HS-LS transition in GS 1124–68. In a geometry where the disk is illuminated by a central source of hot X-rays, the disk should be most ionized when the hard X-ray flux is highest and when the disk is closest to the central source. The hard X-ray fluxes and inner disk radii measured in XTE J1748–288 support this picture. Moreover, the lines that we measure in the VHS and HS, though often significant at 99.9% confidence, are still weaker than

those seen in AGN spectra. Therefore, the strength of the two components predicted for reflection spectra – fluorescent line production and disk reflection, are at least qualitatively consistent.

Ross, Fabian, and Young (1999) note that even the small departures from uniformity that may occur in a highly ionized disk can account for the small reflection fraction often observed in such scenarios, without invoking reflection from the outer disk. This research, and that of Nayakshin, Kazanas, & Kallman (1999) finds that the hottest outer layers of the accretion disk are important in accurately determining disk reflection fractions. These studies find that *Pexriv* may be too basic in its treatment of Compton processes in these hot outer layers. At present, *Pexriv* is the best code publicly available. We look forward to the release of more sophisticated codes and to high resolution data from Chandra and XMM-Newton to constrain new models.

We also note that we are only able to obtain measurements for the reflection fraction inconsistent with zero when the hard flux dominates the 3.5-20.0 keV band-pass we fit. This condition is met throughout the VHS, in obs. 15 in the HS, and throughout the LS. With the exception of obs. 15, we are not able to place tight constraints on reflection in the HS. Many models for disk reflection are based upon AGN spectra (the codes we mention above are notable exceptions), which generally do not contain a soft component in the X-ray band. The extent to which the physical process of soft X-ray emission from the disk is responsible for confusing disk reflection measurements, relative to merely poor mathematical modeling, is unknown.

2.5.3 Implications for Geometry and Accretion Flow

DiMatteo & Psaltis (1999) establish a possible connection between QPO frequency and inner disk radius in BHXBs based on similar work on neutron star (NS) systems:

$$\left(\frac{R_{\text{in}}}{R_{\text{g}}}\right) \leq 27 \nu_1^{-0.35} \left(\frac{M}{2 M_{\odot}}\right)^{-2/3},$$

where ν_1 is the QPO frequency, R_{in} is the inner disk radius, R_{g} the gravitational

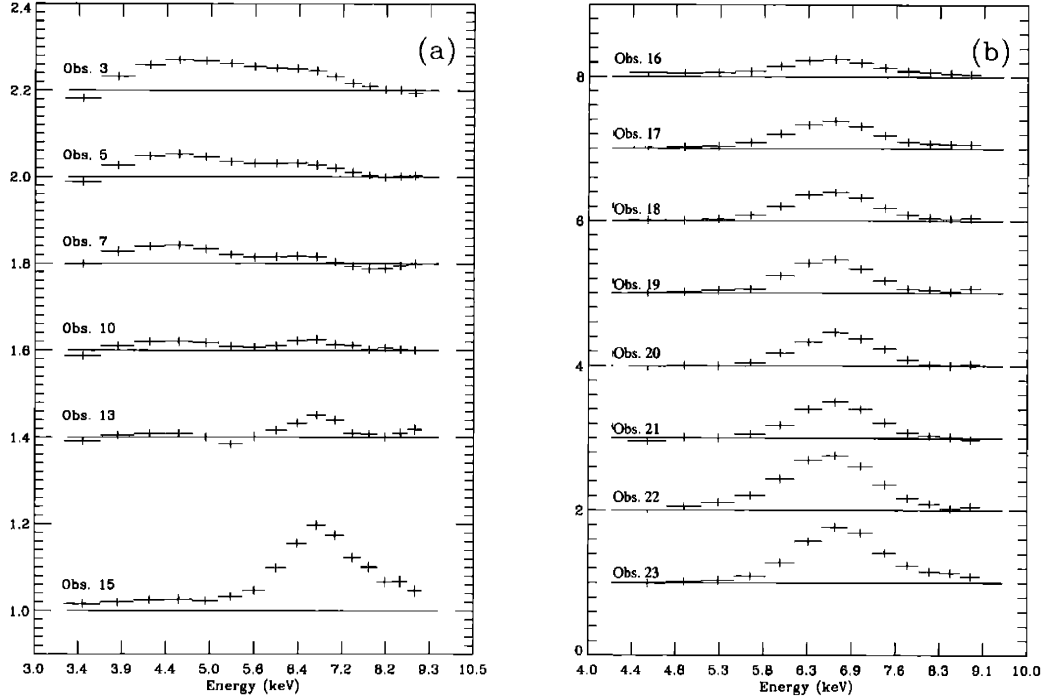


Figure 2-4 Data/model ratios across the outburst. (a) VHS and HS: Models include only the basic multicolor blackbody disk plus power-law components. Observations are offset with respect to each other for clarity; however, the absolute scale is the same for all. The emission excess in observation 3 (at top) is double-peaked, but by the middle of the HS it is clear the profile is becoming single-peaked. Finally, in observation 15 (at bottom) the line feature is very strong and broad. (b) LS: The model is the basic power-law only. It is clear that the line is very prominent relative to the continuum in the LS. Some variation in line centroid energies and widths can be discerned.

radius, M the mass of the black hole, and M_{\odot} a solar mass. For a measured QPO frequency, and a measured or assumed black hole mass, the inner radius can be determined via this equation. Inserting the 32 Hz QPO (Fox & Lewin, 1998) measured in the VHS of XTE J1748–288, and assuming a black hole mass of $10 M_{\odot}$, this equation predicts an upper limit for the accretion disk inner radius of $\sim 2.75 R_g$. This value supports the measurements we obtain via the Laor line model, and our comparison to the models of Martocchia et al. (2000).

The multicolor blackbody disk continuum model also provides a measure of the inner disk radius. A central black hole with a mass of $10 M_{\odot}$ has a gravitational radius of ~ 15 km; a central black hole with mass $5 M_{\odot}$ a gravitational radius of ~ 7.5 km. Fits using the multicolor blackbody disk model measure the inner disk radius in the

VHS to be ~ 10 km. Fits with the Laor disk line emission model in the VHS are consistent with an inner disk radius extending down to $1.2R_g$; this corresponds to ~ 18 km for $M_{BH} = 10 M_\odot$, and ~ 9 km for $M_{BH} = 5 M_\odot$. Finally, the connection noted by DiMatteo & Psaltis (1999) suggests an inner disk radius of $\sim 2.75R_g$, or 41.3 km and 20.6 km for $10 M_\odot$ and $5 M_\odot$ black holes, respectively. Although these methods do not yield exactly the same inner disk radii, they all indicate that the inner edge of the accretion disk extends below the marginally stable orbit for a non-rotating Schwarzschild black hole ($R_{ms,Sch} = 6R_g = 90$ km; for $M_{BH} = 10 M_\odot$, $R_{ms,Sch} = 6R_g = 45$ km, for $M_{BH} = 5 M_\odot$; see Table 2-4 for R_{in} results).

Narayan and Yi (1994) describe a solution for BH accretion geometry wherein a hot, optically thin, inefficiently-cooled plasma advects energy directly onto the BH. Originally developed to describe the presence of hard emission within the spectra of AGN, these Advection-Dominated Accretion Flow (ADAF) models successfully describe a number of AGN (see Narayan 1997 for a review). A natural application of this model is soft X-ray transients in quiescence, where \dot{m} is sufficiently small. BHXBs V404 Cygnus and A0620-00 are well fit by ADAF models in quiescence (Narayan, McClintock, & Yi 1996; Narayan, Barret, & McClintock 1997a).

Esin, McClintock, and Narayan (1997) describe an ADAF/thin-disk composite model tuned to explain the full spectral state evolution of BHXBs over a range of luminosities and \dot{m} . The parameter which drives the spectral transitions is the location of the ADAF/disk transition radius, R_{tr} . When R_{tr} is close to the BH, the emission is dominated by the disk. As the outburst evolves, cooling becomes less efficient, \dot{m} falls, the inner region becomes an ADAF, and R_{tr} increases. Esin et al. predict that in the VHS and HS, the disk may extend to the innermost stable orbit, but in the LS and QS R_{tr} is likely to be near $\sim 10^4 R_g$. This model is applied to the 1991 outburst of GS 1124–68, and describes all but the VHS. Subsequent application of the model to Cygnus X-1 in its LS indicates $R_{tr} \sim 100 R_g$ (Esin et al. 1998).

Zycki, Done, & Smith (1998) constrain the hot advection zone to lie within $\sim 20 - 100 R_g$ in the LS of GS 1124–68, based on smearing of the Compton up-scattering excess observed above ~ 10 keV. The inner radii we measure in the LS of

XTE J1748–288 via the multicolor blackbody disk model and the Diskline relativistic line model also constrain the inner disk edge to lie in this range. We therefore conclude that a large ($10^4 R_g$) inner advection region of the kind predicted by Esin, McClintock, and Narayan is not consistent with the LS of XTE J1748–288 but must be within $100 R_g$ (similar to Cygnus X-1) if such a geometry exists.

We make note of work by Merloni, Fabian, & Ross (2000), which finds that the multicolor blackbody disk model systematically underestimates the real inner disk radius, and can suggest inner disk motion at high accretion rates when in fact the disk is stable at the marginally stable orbit. In the VHS, we find that the multicolor blackbody disk radius is stable and corresponds to the marginally stable orbit for a Kerr black hole (see Table 2.4). The radii we measure via this model in the VHS are supported by radii derived via DiMatteo & Psaltis (1999), but may be an important caveat for HS measurements.

2.5.4 Constraints on the BH Mass

Combining the relation discussed by DiMatteo & Psaltis with the multicolor blackbody disk normalization in the VHS and the radio-band distance estimate, we obtain the following constraint for the mass of the central object in XTE J1748–288 :

$$M \geq 7.9 M_{\odot} \left(\frac{D}{8 \text{ kpc}} \right)^3 \left(\frac{\cos \theta}{\cos 45^\circ} \right)^{-3/2} \left(\frac{N}{100} \right)^{3/2} \left(\frac{\nu}{32 \text{ Hz}} \right)^{1.05},$$

where M is the mass of the compact object, M_{\odot} the solar mass, D the distance in kiloparsecs, N is the normalization of the Diskbb component (see Table 2.2), θ the disk inclination angle, and ν the QPO frequency. Although this calculation is subject to numerous uncertainties, including the uncertain color correction (Ebisawa et al. 1994), taken at face value it implies a black hole primary ($M > 4.5 M_{\odot}$) in XTE J1748–288 for a large parameter space including all likely values of D (>8 kpc from radio measurements) and $\cos \theta$ (<1).

2.5.5 Comparison to Recent Evidence of Lines in BHXBs

Cui, Chen, & Zhang (1999) find two co-moving line features placed quasi-symmetrically about 6.5 keV in the 1996 outburst of 4U 1630-47. It is suggested that each may be due to Doppler-shifted Fe K α emission (not principally gravitational redshifting, in the case of the reddened line).

Balucinska-Church & Church (2000) report on four spectra from GRO J1655-40, and find evidence for gravitationally redshifted and Doppler-broadened emission. Our finding that the red emission wing is more prominent than the blue emission wing early in the VHS of XTE J1748-288 is qualitatively similar to these results. Additionally, fits with Pexrvt to these observations of GRO J1655-40 find limits for disk reflection ($f < 1\%$) and ionization ($\xi < 10^4$). Like the HS of XTE J1748-288 these observations occur when the flux is dominated by the soft disk component, likely complicating efforts to measure any reflection.

Unfortunately, 4U 1630-47 and GRO J1655-40 are both known to be “dipping” sources (Kuulkers et al. 1988) – to experience periods of markedly different absorption during outburst – and this complicates efforts to trace spectral lines across a full outburst and thereby constrain accretion flow geometries.

2.6 Conclusions

We have analyzed the 22 publicly-available observations between maximum X-ray luminosity and quiescence from the outburst of galactic microquasar XTE J1748-288. The spectra can be categorized into Very High, High, and Low States based on the relative flux contributions from hard and soft continuum components. We trace emission lines through these spectral states, and find evidence for an Fe K α line that is gravitationally redshifted and Doppler shifted in the VHS, with a profile that is consistent with emission from the innermost stable orbit for a maximally rotating Kerr black hole. The line is less redshifted but increasingly prominent in the HS. Finally, in the LS, the line is centered at 6.7 ± 0.10 keV, and we measure a profile that is consistent with emission from a disk with inner radius between $R \sim 20$ and

$R \sim 100 R_g$.

We fit each observation with a power-law continuum model (Pexriv) that includes Compton reflection of hot incident X-rays from an ionized disk component, manifested spectrally as a broad excess above ~ 10 keV. This work represents the first trace of the disk reflection fraction across the full outburst of a BHXB. The fractions we measure in the VHS and HS are much smaller than those often measured in AGN, but well-constrained. We note that the Pexriv model may be too basic for accurate reflection measurements, and urge the public release of new codes.

The Fe $K\alpha$ line serves as a direct diagnostic of the accretion geometry. We consider our findings in the context of the ADAF model developed by Esin, McClintock, & Narayan (1997) to describe the spectral states of BHXBs. As the disk in XTE J1748–288 is measured to be a few tens of R_g from the BH in the LS, rather than 10^3 – $10^4 R_g$, we find that the predictions of this ADAF model are inconsistent with the accretion geometry of XTE J1748–288. We look forward to data from Chandra and XMM to obtain higher-resolution spectra of a BHXB in outburst.

Table 2.1 The *RXTE*/PCA observation log

No.	Obs.ID	Date, UT	Start Time	PCA Exp. (s)
1	30188-05-01-00	04/06/98	20:05:04	1760
2	30188-05-02-00	05/06/98	03:03:44	768
3	30171-02-01-00	06/06/98	09:41:20	2655
4	30185-01-01-00	07/06/98	07:56:32	2944
5	...-02-00	08/06/98	06:23:28	3027
6	...-03-00	09/06/98	12:48:00	3729
7	...-04-00	10/06/98	03:38:24	7721
8	...-05-00	11/06/98	12:52:16	3439
9	...-06-00	13/06/98	12:51:28	3114
10	...-07-00	15/06/98	04:53:36	1795
11	...-08-00	18/06/98	20:55:12	2327
12	...-09-00	22/06/98	22:30:08	3210
13	...-10-00	27/06/98	11:39:28	1647
13.1	...-10-01	02/07/98	18:18:24	1280
14	...-11-00	08/07/98	16:21:52	1295
15	...-12-00	13/07/98	06:44:00	2056
16	...-13-00	18/07/98	04:00:32	10585
17	...-14-00	30/07/98	09:44:48	6841
18	...-15-00	05/08/98	18:25:20	4333
19	...-16-00	13/08/98	10:17:36	1565
20	...-17-00	20/08/98	16:41:20	1704
21	...-18-00	25/08/98	03:32:00	1785
22	...-19-00	14/09/98	08:17:36	886
23	...-20-00	26/09/98	03:29:04	10287

Note. — Observations 1 and 2 are during the rise of the outburst. The remaining observations were made during the declining portion of the outburst, and are public data.

Table 2.2. Spectral Component Paramters of XTE J1748–288

(1) Obs.	(2) T_{DBB} (keV)	(3) Norm.	(4) R_{DBB} (km)	(5) Flux_{DBB} 10^{-9} cgs	(6) α_{pi}	(7) f 10^{-2}	(8) F-stat.	(9) ξ 10^3	(10) Norm.	(11) Flux_{pi} 10^{-9} cgs	(12) Flux_{tot} 10^{-9} cgs	(13) χ^2/dof
— Very High State —												
3	1.57(1)	90(3)	9.0(1)	3.6(1)	2.728(1)	2.1(6)	0.079	7^{+17}_{-6}	15.59(5)	7.82(2)	11.4(1)	1.02
4	1.53(1)	104(4)	9.7(1)	3.7(1)	2.736(1)	2.2(7)	0.036	3^{+8}_{-2}	15.48(5)	7.63(2)	11.3(1)	0.64
5	1.29(2)	108(9)	9.9(3)	1.5(1)	2.631(1)	2.2(6)	0.001	3^{+4}_{-2}	13.80(3)	8.43(2)	9.9(1)	0.49
6	1.19(2)	125(13)	10.6(5)	1.1(1)	2.515(1)	0.5(4)	0.403	2†	10.57(3)	8.15(2)	9.3(1)	0.45
7	1.22(2)	116(11)	10.2(4)	1.1(1)	2.571(1)	6.6(6)	<0.001	2†	11.07(2)	7.68(2)	8.8(1)	0.34
8	1.26(2)	88(6)	8.9(2)	1.0(1)	2.466(1)	3.6(9)	<0.001	2†	5.43(2)	4.64(2)	5.6(1)	0.51
— High State —												
9	1.29(1)	388(6)	18.7(2)	5.3(1)	2.73(2)	2^{+5}_{-2}	1.0	2†	3.62(2)	1.81(1)	7.1(1)	0.42
10	1.31(1)	370(6)	18.3(2)	5.5(1)	2.94(3)	2^{+12}_{-2}	1.0	2†	3.5(2)	1.15(8)	6.7(1)	0.69
11	1.26(1)	403(6)	19.1(1)	5.9(1)	2.90(6)	2^{+4}_{-2}	1.0	2†	2.1(3)	0.72(8)	6.6(1)	0.55
12	1.20(1)	436(8)	19.9(1)	3.8(1)	2.69(7)	1^{+21}_{-1}	1.0	2†	1.0(1)	0.53(1)	4.3(1)	0.70
13	1.15(1)	440(8)	20.0(1)	3.3(1)	2.58(1)	3^{+4}_{-1}	1.0	2†	0.87(8)	0.57(7)	3.9(1)	0.69
13.1	1.03(1)	450(10)	20.2(3)	1.6(1)	2.47(5)	7^{+32}_{-3}	1.0	2†	0.89(2)	0.68(1)	2.3(1)	0.45
14	0.98(1)	440(10)	20.0(3)	1.1(1)	2.41(7)	3^{+26}_{-3}	1.0	2†	0.63(7)	0.6(1)	1.7(1)	1.13
15	0.91(1)	390(10)	18.8(3)	0.56(5)	2.44(5)	11.1(1)	<0.001	2†	0.97(1)	0.87(2)	1.4(1)	0.94
— Low State —												
16	0.42(3)	7800^{+500}_{-3700}	84(36)	0.02(1)	1.86(2)	8^{+4}_{-2}	<0.001	0	0.32(1)	1(1)	1.1(1)	0.75
17	0.34(9)	$12900^{+164100}_{-5200}$	100^{+300}_{-20}	0.03(1)	1.98(1)	45(2)	<0.001	0	0.24(1)	0.64(1)	0.67(1)	0.62
18	0.34(8)	14400^{+73000}_{-7200}	100^{+300}_{-20}	0.02(1)	1.95(2)	21(2)	<0.001	0	0.20(1)	0.54(2)	0.57(1)	1.02
19	—	—	—	—	2.02(1)	28(3)	<0.001	0	0.21(1)	0.49(2)	0.51(1)	0.85

Table 2.2—Continued

(1) Obs.	(2) T_{DBB} (keV)	(3) Norm.	(4) R_{DBB} (km)	(5) Flux_{DBB} 10^{-9} cgs	(6) α_{pl}	(7) f 10^{-2}	(8) F-stat.	(9) ξ 10^3	(10) Norm.	(11) Flux_{pl} 10^{-9} cgs	(12) Flux_{tot} 10^{-9} cgs	(13) χ^2/dof
20	—	—	—	—	1.90(1)	4(2)	0.254	$0.15^{+0.85}_{-0.15}$	0.11(1)	0.32(1)	0.34(1)	0.78
21	—	—	—	—	1.91(1)	4(3)	1.0	$0^{+0.6}$	0.10(1)	0.28(1)	0.31(1)	0.72
22	—	—	—	—	2.17(1)	11(3)	<0.001	0	0.17(1)	0.28(1)	0.31(1)	0.77
23	—	—	—	—	2.08(1)	1.0(1)	1.0	0	0.10(1)	0.21(1)	0.23(1)	0.40

Note. — Spectral component parameters of XTE J1748–288. Basic model parameters and normalizations quoted with 90% confidence limits. Model components include a multicolor blackbody, a Gaussian, and Pexriv. All fluxes are measured in the 3.5–20.0 keV band, as are all model parameters and normalizations. Where errors are not quoted, the error does not affect the value of the last significant digit. Fits to the VHS and HS have 30 *dof* when red and blue lines are fit, and 36 *dof* when lines are not fit. Fits to the LS have 33 *dof* when the blue line is fit, 36 *dof* when they are not. Quoted χ^2 values are for models including lines. All observations fit with 0.75% systematic errors added, and (fixed) $N_H = 7.5 \times 10^{22} \text{ cm}^{-2}$. R_{DBB} is the disk-blackbody-derived inner radius, calculated for a disk inclination of 45 degrees (assumed), and a distance of 8 kpc. The Pexriv power-law cut-off energy is fixed at 200 keV, and the disk inclination at 45 degrees. f is the disk reflection fraction, $0.0 < f < 1.0$ corresponds to the range $0 - 2\pi$, and F-stat is the standard F statistic, measuring the significance of f (f is more significant for lower F). † denotes an observation where the ionization is fixed at 2000.

Table 2.3 Fe K α Emission Line Paramters

Obs.	Centroid Energy (keV)	Width (keV)	Eq.Width (eV)	Flux 10^{-11} cgs	χ^2/dof w/o line	χ^2/dof w/ line	F-stat.
— Red Wing —							
— Very High State —							
3	4.6(1)	$0.2^{+0.1}_{-0.2}$	76(15)	17(2)	4.19	1.02	<0.001
4	4.6(1)	0.4(1)	105(15)	22(3)	5.62	0.64	<0.001
5	4.6(3)	0.3(2)	69(14)	12(3)	2.97	0.49	<0.001
6	4.5(2)	$0.3^{+0.2}_{-0.3}$	51(14)	8(2)	1.87	0.45	<0.001
7	4.5(2)	0.3(3)	57(15)	8(2)	1.96	0.34	<0.001
8	4.7(1)	0.5(1)	96(14)	9(1)	4.62	0.50	<0.001
— High State —							
9	4.5(2)	0.3(3)	39(12)	7(2)	1.35	0.42	<0.001
10 [†]	4.5(3)	$0^{+0.5}$	23(9)	4(2)	1.00	0.69	0.14
11	4.5(2)	$0^{+0.5}$	20(9)	3(1)	0.83	0.45	0.04
12	—	—	—	—	—	—	—
13	—	—	—	—	—	—	—
13.1	—	—	—	—	—	—	—
14	—	—	—	—	—	—	—
15	—	—	—	—	—	—	—
— Blue Wing —							
— Very High State —							
3	5.8(1)	0.8(1)	120(20)	19(4)	5.42	1.02	<0.001
4	6.3(2)	0.4(2)	66(16)	10(2)	2.49	0.64	<0.001
5	6.3(3)	0.5(3)	51(19)	6(2)	1.57	0.49	<0.001
6	6.4(3)	0.5(4)	45(16)	5(2)	1.25	0.45	0.002
7	6.4(3)	0.4(4)	39(18)	4(1)	1.09	0.34	<0.001
8	6.6(2)	0.4(3)	60(18)	4(1)	2.00	0.50	<0.001
— High State —							
9	6.4(3)	$0.4^{+0.3}_{-0.4}$	39^{+19}_{-12}	4(2)	1.20	0.42	0.002
10 [†]	6.5(3)	$0.3^{+0.6}_{-0.3}$	30^{+20}_{-12}	3(1)	1.07	0.69	0.103
11	6.6(3)	$0.1^{+0.7}_{-0.1}$	29^{+15}_{-12}	2(1)	1.03	0.55	0.036
12	6.8(2)	$0.0^{+0.5}_{-0.1}$	33(10)	3(1)	1.31	0.70	0.036
13	6.7(1)	$0.0^{+0.3}_{-0.1}$	56^{+14}_{-11}	2(1)	2.19	0.69	<0.001
13.1	6.8(1)	0.2(2)	88^{+19}_{-16}	2.0(4)	3.13	0.45	<0.001
14	6.74(9)	0.2(2)	130(19)	2.0(3)	5.96	1.13	<0.000
15	$6.69^{+0.09}_{-0.04}$	0.2(1)	347(31)	4.8(5)	23.7	0.94	<0.001
— Low State —							
16	6.68(4)	$0.06^{+0.14}_{-0.06}$	193(13)	1.8(1)	16.9	0.75	<0.001
17	6.72(3)	0.30(5)	420(19)	2.3(1)	44.6	0.62	<0.001
18	6.71(3)	0.32(4)	508(22)	2.4(1)	50.1	1.02	<0.001
19	6.68(3)	0.20(8)	545(25)	2.3(1)	32.6	0.85	<0.001
20	6.80(3)	0.24(7)	574(30)	1.6(1)	27.0	0.78	<0.001
21	6.77(3)	0.24(6)	661(36)	1.7(1)	25.8	0.72	<0.001
22	6.65(4)	0.34^{+16}_{-12}	931(54)	2.5(1)	30.4	0.77	<0.001
23	6.78(3)	0.26(4)	967(40)	1.6(1)	30.5	0.40	<0.001

Note. — Line parameters, normalizations, and fluxes, are all quoted with 90% confidence limits. Fits to the VHS and HS have 30 *dof* when red and blue lines are fit, and 36 *dof* when lines are not fit. Fits to the LS have 33 *dof* when the blue line is fit, 36 *dof* when they are not. The *F*-statistic is the classic f-test statistic. Observations 12, 13, 13.1, 14, and 15 are not consistent with the inclusion of a red wing. † denotes observations where measurements constrain parameters but do not meet our criterion for statistical significance.

Table 2.4 Three Methods to R_{in} in the VHS

Obs.	$\nu_{QPO}^{(a)}$ (Hz)	$R_{in}^{(b)}$ (R_g)	$R_{in}^{(c)}$ (R_g)	$R_{in}^{(d)}$ (R_g)
3	31.6(2)	4.38(1)	2.8(1)	1.2(1)
4	31.3(2)	4.39(1)	2.8(1)	1.3(1)
5	23.7(1)	4.84(1)	3.0(1)	1.3(1)
6	20.2(1)	5.12(1)	3.2(1)	1.4(1)
7	20.0(1)	5.14(1)	3.2(1)	1.4(1)
8	22.6(2)	4.92(1)	3.1(1)	1.2(1)

Note. — Three Methods to R_{in} in the VHS. R_{in} values in R_g . In the VHS, the Laor relativistic disk line emission model can be fit to the Fe K_α profile with $R_{in} = 1.2 R_g$ with statistical significance comparable to that of the Gaussian model. The relation described by DiMatteo & Psaltis (1999) is shown in Equation 1 within the text. Given ν_{QPO} and assuming a BH mass, an inner disk radius may be derived assuming Keplerian orbits up to the marginally stable orbit. (a) QPO frequencies reported by Revnivtsev et al. 1999. (b) Calculated via Equation 1 for $M_{BH} = 5.0 M_\odot$. (c) Calculated via Equation 1 for $M_{BH} = 10.0 M_\odot$. (d) The multicolor blackbody disk radius.

Table 2.5 LS Observations Fit With the Diskline Model

Obs.	E_{cent} (keV)	R_{in} (R_g)	EW (eV)	Flux(3–25 keV) $10^{-11} cgs$	χ^2/dof (Gaussian)	χ^2/dof (diskline)
16	6.68(4)	63^{+933}_{-31}	200(12)	2.1(1)	0.75	0.55
17	6.72(3)	25^{+26}_{-19}	411(16)	2.5(1)	0.62	0.77
18	6.69(3)	6^{+15}_{-1}	533(19)	2.6(1)	1.02	0.81
19	6.70(4)	102^{+140}_{-63}	525(24)	2.6(1)	0.85	0.91
20	6.81(4)	22^{+33}_{-16}	612(29)	1.8(1)	0.78	0.89
21	6.78(3)	25^{+29}_{-19}	682(27)	1.8(1)	0.72	0.80
22	6.65(4)	14^{+12}_{-8}	915(41)	2.9(1)	0.77	0.96
23	6.79(3)	35^{+34}_{-15}	916(33)	2.0(1)	0.40	0.80

Note. — LS observations fit with the Diskline model. We fix R_{out} at $10^4 R_g$, the emissivity profile to r^{-2} , and the disk inclination at 45 degrees. With these parameters fixed, and using the pexriv parameters obtained via fitting with a Gaussian line model, we measure line centroid energy (E_{cent}), inner radius (R_{in}), equivalent width (EW), the 3.5–20.0 keV line flux, and the reduced χ^2 values for fits with a Gaussian, and with diskline. Errors are 90% confidence limits. Fits have 36 dof without the diskline model, 33 dof with the model. All fits with the diskline model are significant at greater than 99.9% confidence. Although the relative χ^2 values do not demand the diskline over the Gaussian model, the parameters of the diskline model are very well-constrained.

2.7 Bibliography

- Balucinska-Church, M., and Church, M. J., 2000, MNRAS 312, L55
Blandford, R. D., & Begelman, M. C., 1999 MNRAS 303L, 1B
Bradt, H. V., Rothschild, R. E., & Swank, J. H. 1993, A&AS, 97, 355
Cui, W., Zhang, S. N., and Chen, W., 1998, ApJ, 492, L53
Cui, W., Zhang, S. N., Chen, W., and Morgan, E. H., 1999a, ApJ. 512, L43
Cui, W., Chen, W., and Zhang, S. N., 1999, ApJ 529, 952
Dabrowski, Y., Fabian, A. C., Iwasawa, K., Lasenby, A. M., and Reynolds, C. S., 1997, MNRAS, 288, L11
DiMatteo, T., & Psaltis, D., 1999, ApJ 526L, 101D
Done, C., Madejski, G. M., and Zycki, P.T., 2000, astro-ph/0002023
Ebisawa, K., et al., 1994, PASJ, 46, 375
Esin, A. A., McClintock, J. E., and Narayan, R., 1997, ApJ 489, 865
Esin, A. A., Narayan, R., Cui, W., Grove, E. J., & Zhang, S. N., 1998, ApJ 505, 854
Fabian, A. C., Rees, M. J., Stella, L., and White, N. E., 1989, MNRAS, 238, 729
Fabian, A. C., Iwasawa, K., Reynolds, C. S., & Young, A. J., 2000, PASP, in press (astro-ph/0004366)
Fender, R., et al., 1999, ApJ 519, L165
Fender, R., 2000, astro-ph/9911176
Fox, D. W., & Lewin, W. H. G. 1998, IAUC 6992
George, I. M., & Fabian, A. C., 1991, MNRAS, 249, 352
Gierlinski, M., et al., 1997, MNRAS, 288, 958
Gierlinski, M., Zdziarski, A. A., Poutanen, J., Coppi, P. S., Ebisawa, K., and Johnson, W. N., 1999, MNRAS, 309, 496-512
Hjellming, R. M., et al., 1998a, IAUC 6937
Hjellming, R. M., et al., 1998b, American Astron. Soc. Meeting # 193, 103.08
Iwasawa, K., Fabian, A. C., Young, A. J., H. Inoue, & Matsumoto, C., 1999, MNRAS 306L, 19
Jahoda, K., Swank, J. H., Giles, A. B., Stark, M. J., Strohmayer, T., Zhang, W., & Morgan, E. H., 1996, SPIE, 2808, 59
Kotani, T., et al., 1999, in X-ray Astronomy 2000, a special issue of Astrophysical Letters and Communications, in press
Kuulkers, E., Wijnands, R., Belloni, T., Mendez, M., van der Klis, M., van Paradijs, J., 1998, ApJ 494 753
Laor, A., 1991, ApJ 376, 90
Levine, A. M., Bradt, H., Cui, W., Jernigan, J. G., Morgan, E. H., Remillard, R., Shirey, R. E., & Smith, D. A., 1996, ApJ, 469, L33
Magdziarz, P., & Zdziarski, A., 1995, MNRAS 273, 837
Martocchia, A., et al., 2000, MNRAS 312, 817
Mendez, M., and van der Klis, M., 1997, ApJ, 479, 926
Merloni, A., Fabian, A. C., & Ross, R. R., 2000, MNRAS 313, 193
Mirabel, I. F., & Rodriguez, L. F., 1994, Nature, 371, 46
Mitsuda, K., et al., 1984, PASJ, 36, 741
Morgan, E., Remillard, R., & Greiner, J., 1997, ApJ, 482, 993

- Mushotzky, R. F., Fabian, A. C., Iwasawa, K., Kunieda, H., Matsuoka, M., Nandra, K., and Tanaka, Y., 1995, *MNRAS*, 272, L9
- Nandra, K., George, I. M., Mushotzky, R. F., Turner, T. J., and Yaqoob, T., 1997, *MNRAS*, 476, 602
- Narayan, R., McClintock, J. E., and Yi, I., 1996, *ApJ*, 457, 821
- Narayan, R., Barret, D., and McClintock, J. E., 1997a, *ApJ*, 482, 448
- Narayan, R., & Yi, I., 1994, *ApJ*, 428, L13
- Narayan, R., 1997, in *IAU Colloq. 163, Accretion Phenomena and Related Outflows*, ed. D. T. Wickramasinghe et al., (Dordrecht: Kluwer), 75
- Nayakshin, S., Kazanas, D., & Kallman, T., 2000, *ApJ* 537, 833
- Orosz, J., & Bailyn, C., 1997, *ApJ*, 477, 876
- Reig, P., Belloni, T., van der Klis, M., Mendez, M., Kylafis, N., & Ford, E., 2000, *ApJ*, submitted (astro-ph/0001134)
- Remillard, R. A., Morgan, E. H., Greiner, J., 1997, *ApJ* 482, 993
- Remillard, R. A., 1999, *ApJ*, 517, L127
- Revnivtsev, M. G., Trudolyubov, S. P., and Borozdin, K. N., 2000, *MNRAS* 312 151
- Ross, R. R., Fabian, A. C., & Young, A. J., 1999, *MNRAS* 306, 461
- Rupen, M. P., Hjellming, R. M., and Mioduszewski, A. J., 1998, *IAUC* 8938
- Smith, D., Levine, A., and Wood, A., 1998, *IAUC* 6932
- Sobczak, G., McClintock, J. E., Remillard, R. A., Levine, A., Morgan, E. H., Bailyn, C. D., and Orosz, J. A., 1999, *ApJ*, L121-L125
- Sobczak, G. J., Remillard, R. A., Munro, M. P., McClintock, J. E., 2000, *ApJ*, submitted (astro-ph/0004215)
- Sunyaev, R. A., & Titarchuk, L. G., 1980, *A & A* 86, 121
- Tanaka, Y., et al., 1995, *Nat*, 375, 659
- Takaka, Y., and Lewin, W. H. G., in "X-ray Binaries", eds. W. H. G. Lewin, J. van Paradijs, & E. P. J. van den Heuvel (Cambridge U. Press, Cambridge)
- Zhang, S. N., Cui, W., and Chen, W., 1997, *ApJ*, 482, L155
- Zhang, S. N., et al., 2000, *Science*, in publication
- Zycki, P. T., Done, C., and Smith, D. A., 1998, *ApJ* 496, L25-L28
- Zycki, P. T., Done, C., and Smith, D. A., 1999, *MNRAS* 305, 231

Chapter 3

Fast Quasi-Periodic Variability in the X-ray Lightcurve of the 2000 Outburst of XTE J1550–564

This chapter is based on the original paper:

“High-Frequency Quasi-Periodic Oscillations in the 2000 Outburst of the Galactic Microquasar XTE J1550–564,” Miller, J. M., Wijnands, R., Homan, J., Belloni, T., Pooley, D., Corbel, S., Kouveliotou, C., van der Klis, M., and Lewin, W. H. G., 2001, *The Astrophysical Journal*, Vol. 563, p. 928,

with the permission of the publisher, *The Astrophysical Journal*.

3.1 Abstract

We present an analysis of the high frequency timing properties of the April-May 2000 outburst of the black hole candidate and Galactic microquasar XTE J1550–564, measured with the *Rossi X-ray Timing Explorer*. The rapid X-ray variability we measure is consistent with the source being in either the “very high” or “intermediate” black hole state. Strong (5–8% rms) quasi-periodic oscillations (QPOs) are found between

249-276 Hz; this represents the first detection of the same high frequency QPO in subsequent outbursts of a transient black hole candidate. We also present evidence for lower-frequency QPOs at approximately 188 Hz (3.5σ , single trial), also reported previously and likely present simultaneously with the higher-frequency QPOs. We discuss these findings within the context of the 1998 outburst of XTE J1550–564, and comment on implications for models of QPOs, accretion flows, and black hole spin.

3.2 Introduction

The sub-class of X-ray binaries identified as “microquasars” is growing steadily as efforts increase to observe both persistent and transient systems simultaneously in the X-ray and radio bands. Yet, only two transient black hole candidate (BHC) systems with apparently superluminal jet motion have been observed in repeated outbursts (separated by clear quiescent periods) reaching flux levels in excess of 0.5 Crab in soft X-rays: GRO J1655–40 and XTE J1550–564. Similar jets and luminosities have been observed by many in GRS 1915+105; this source has been in outburst continuously during the RXTE era.

The X-ray lightcurves of BHCs are usually described in terms of canonical states characterized by specific spectral and timing properties. The details of these states are discussed at length elsewhere (for reviews, see Tanaka & Lewin 1995, and van der Klis 1995; for a recent discussion see Homan et al. 2001). We merely note the states briefly: the Very High State (VHS) is often most luminous, may contain significant flux from both soft (<5 keV; usually a multi-color disk blackbody as per Mitsuda et al. 1984) and hard (>5 keV; usually a power-law) flux components, and quasi-periodic oscillations (QPOs) and/or significant timing noise; the High State (HS) is strongly dominated by the soft flux and has weak (\sim few per cent rms) power-law-like timing noise; the Intermediate State (IS) is very similar to the VHS but less luminous; the Low State (LS) is dominated by the hard component, has strong band-limited timing noise ($>20\%$ rms), and sometimes QPOs; and the Quiescent or “Off” State (QS),

which is characterized by a very weak spectral power-law.

The 1998–1999 outburst of XTE J1550–564 (Smith 1998) was one of the most remarkable yet observed from a BHC system. A quasi-periodic oscillation (QPO) with a frequency as high as 285 Hz was observed (Remillard et al. 1999a; Homan, Wijnands, & van der Klis 1999; Homan et al. 2001), X-ray state transitions were observed which challenge the primacy of the mass accretion rate \dot{m} in driving outbursts (Homan et al. 2001), and radio monitoring revealed jet production with apparent velocity of $v_{\text{jet}} > 2c$ (Hannikainen et al. 2001).

After a quiescent period of several months, on 2 April 2000, new activity in XTE J1550–564 was noticed with the *RXTE* All Sky Monitor (ASM, Levine et al. 1996; XTE J1550–564 Smith et al. 2000), and the ensuing outburst lasted more than 70 days. This outburst reached a peak flux of ~ 1 Crab in the ASM (1.5–12 keV, see Figure 3-1). The source was seen out to 300 keV with BATSE aboard *CGRO*, and simultaneously in optical bands (Masetti & Soria 2000; Jain, Bailyn, Orosz, et al. 2000). Evidence for emission from a compact jet (an inverted radio spectrum) was reported during the hard-X-ray-flux-dominated late decay phase of this outburst; a possible discrete ejection event may have been observed during the rapidly rising phase (Corbel et al. 2001).

On 28 January, 2001, activity was noticed in XTE J1550–564 for a third time. *RXTE* found the source to be in the LS, with timing noise of 40% rms and an energy spectrum characterized by a power-law with photon index $\Gamma = 1.52$ (Tomsick et al. 2001).

The second outburst met the trigger criteria for our *RXTE* Cycle 5 Target of Opportunity program to study a BHC in outburst (*Chandra* spectroscopy of this outburst is detailed in Miller et al. 2001b, and radio results in Corbel et al. 2001). We observed XTE J1550–564 with *RXTE* on 18 occasions totaling 54.9 ksec of data between 24 April and 12 May 2000. We report QPOs with a frequencies ranging between 249–278 Hz. This finding is discussed within the context of the previous outburst of XTE J1550–564, the behavior observed in GRO J1655–40 and GRS 1915+105, and models for the inner accretion environments in these and other BHC systems.

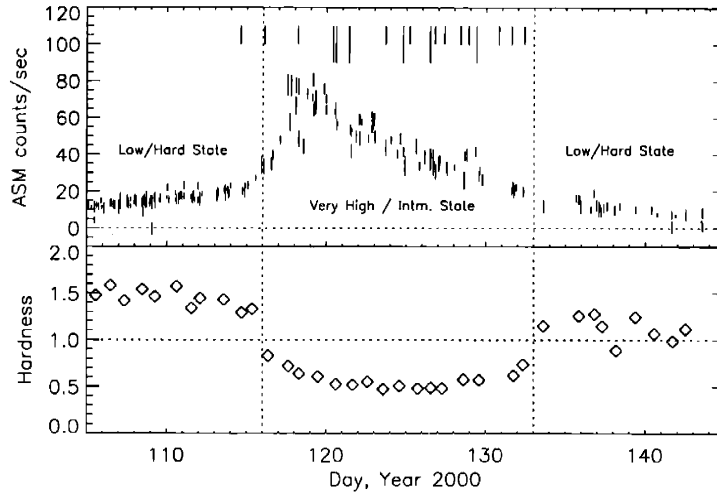


Figure 3-1 The ASM dwell-by-dwell lightcurve with errors (1.5–12 keV), and one-day averaged (5–12 keV)/(3–5 keV) hardness ratios, for the April-May 2000 outburst of XTE J1550–564 (see also Miller et al. 2001b, Corbel et al. 2001). The source rise is typical of the LS. It is followed by a VHS/IS episode where the flux softens as the overall flux increases rapidly, and finally decays in a LS into quiescence. The dashed vertical lines indicate the state transitions. All of the high frequency QPOs we report occur during the VHS/IS. Vertical marks at the top of the plot denote the days on which we observed XTE J1550–564; longer marks denote observations in which a high frequency QPO is found.

3.3 Observations

In stark contrast to the 1998–1999 outburst of XTE J1550–564, the 2000 outburst lightcurve roughly follows a fast-rise exponential-decay (or, “FRED”) profile. Based on the (5–12 keV)/(3–5 keV) hardness ratio accompanying the 1.5–12 keV ASM lightcurve in Figure 3-1, the spectral analysis presented in Miller et al. (2001b), and the timing results we detail in this work, we identify three outburst states: an initial LS, a VHS/IS, and a final LS. Whereas we can identify the middle state using timing, spectral, and hardness signatures, the initial and final state identifications are less certain. We have only one PCA observation in the initial LS, the latter LS identification is based only on the ASM hardness ratio as we have no PCA observations within this state (for timing studies of the LS, see Kalemci et al. 2001). The middle state is not a HS episode: the soft component does not strongly dominate the X-ray flux and power-law timing noise is not observed. This state is the most luminous within the 2000 outburst, but it is less luminous than the VHS reported in the 1998–

1999 outburst (fast QPOs were observed in both the VHS and IS during the 1998–1999 outburst). Although this state is more likely an IS episode, as a clear determination cannot be made we refer to the middle state simply as the VHS/IS.

In all observations, data were collected in the Standard 1 (1/8 second time resolution in one photon energy channel for the energy range 2–60 keV) and the Standard2f (129 channels for 2–60 keV, 16 seconds time resolution) modes. Simultaneously, data were collected in several single bit and event modes. In the first three observations wherein we report a high frequency QPO (see Table 3.1), these modes are SB_125us_0_17_1s (128 μ s time resolution in one 2–7.5 keV energy channel), SB_125us_18_35_1s (128 μ s time resolution in one 7.5–15 keV energy channel), and E_16us_16B_36_1s (16 μ s time resolution in 16 channels from 15–60 keV). In the latter five observations, these modes are SB_125us_0_13_1s (128 μ s time res. in one 2–6 keV energy channel), SB_125us_14_35_1s (128 μ s time resolution in one 6–15 keV energy channel), and E_8us_32M_36_1s (8 μ s time resolution in 32 channels from 15–60 keV). Due to the fact that the modes in the early observations do not cover exactly the same channels as the modes used in the latter observations, we cannot examine the energy dependence of the fast QPO in exactly the same energy ranges across the outburst, although the differences are very small.

3.4 Analysis and Results

We made power spectra, using 16 second data segments, of the combined single-bit and event modes data. In order to explore the high frequency regime in this outburst, we analyze the range 64–4096 Hz. Although we detect QPOs between 1–10 Hz similar to those reported in the first outburst of XTE J1550–564 (e.g., Homan et al. 2001), the analysis and interpretation of these features is complicated and left to future work.

We fitted the 64–4096 Hz range with a model consisting only of a Poisson noise component and a single Lorentzian; we obtain reduced χ^2 values roughly between 1–1.3 using this model (for 176 degrees of freedom). We report QPOs with frequencies

varying between 249–278 Hz, significant at $4.4\text{--}6.2\sigma$, exclusively in observations during the VHS/IS, though not in all VHS/IS observations. The significance of the QPOs is highest at the start of the VHS/IS and decreases steadily (though not monotonically) through the state. We report the QPO parameters in Table 3.1 in the energy band where the features are most significant (6–60 keV) for observations where a QPO is clearly present; the quoted errors are for $\Delta\chi^2 = 1$ (1σ).

The strength of the QPOs is also examined in the 2–60 keV, 2–6 keV, 6–15.3 keV, and 15.3–60 keV bands (bands chosen as single-bit and event mode binning allowed). As is typical for high frequency QPOs in BHCs, the QPOs are stronger in the higher energy bands and weaker when the 2–6 keV band is included. In Figure 3-2, we show how the QPO parameters vary as a function of time and as a function of 2–60 keV flux. The strength decreases with time, and increases with flux; these findings are consistent with the QPO significance decreasing as the VHS/IS flux decays. The QPO FWHM is constant. Within errors, the QPO frequency decreases monotonically with time, and increases monotonically with 2–60 keV flux.

We also analyzed the strength, FWHM, and frequency of the QPO versus three hardness ratios: (6–15 keV)/(2–6 keV), (15–60 keV)/(6–15 keV), and (15–60 keV)/(2–6 keV) (see Figure 3-3). The frequencies and strengths are weakly anti-correlated with increasing (6–15 keV)/(2–6 keV) hardness, weakly positively correlated with increasing (15–60 keV)/(6–15 keV) hardness, and weakly anti-correlated with increasing (15–60 keV)/(2–6 keV) hardness.

We measure upper limits on the strength of possible QPO features on days where the 268 Hz QPO is not clearly observed. For observations made on days (of the year 2000) 114.6, 116.1, 118.2, 123.7, we report 95% confidence upper limits for the 268 Hz QPO between 2.7–5.2% rms for a feature with FWHM fixed at 50 Hz in the 64–512 Hz range (6–60 keV). We note that the upper limit obtained for the only observation for which XTE J1550–564 is in the LS (day 114.6; see Figure 3-1) is 2.7%. For observations made on days 125.2, 126.8, 127.4, 128.4, 128.9, 130.8, 131.6, and 132.4, the 95% confidence upper limits range between 5.1–6.4% rms. Any fast QPO in these observations is significant at only the 2σ level, or less. Thus, the 268 Hz

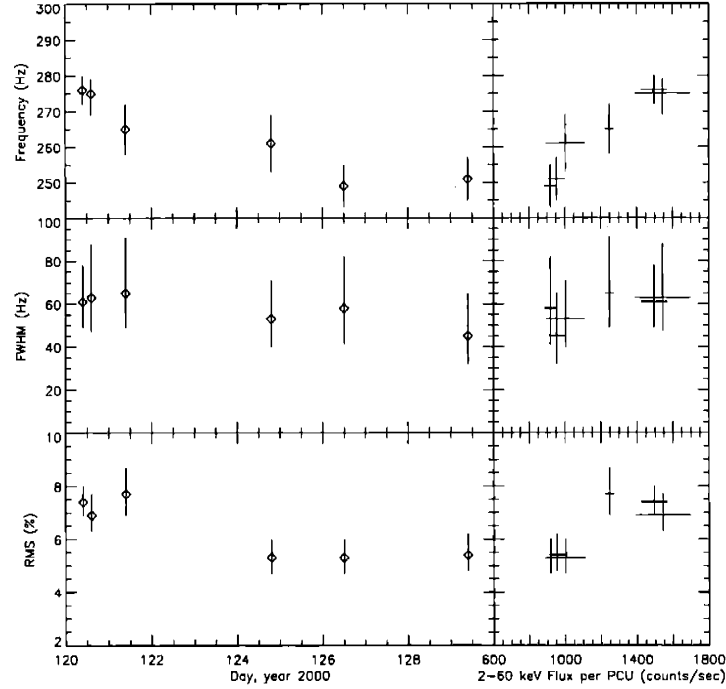


Figure 3-2 QPO frequency, FWHM, and rms plotted versus time and flux. Displayed errors in QPO parameters and flux are 1σ confidence errors.

QPO is only clearly detected in the observations which fall within the VHS/IS. At the time of writing, observations made during the LS episode following the VHS/IS are not yet public, however Kalemci et al. (2001) report on timing studies of the LS and find no evidence for the 268 Hz QPO.

We note evidence for a second fast QPO, at 188 ± 3 Hz. In simply adding all six observations in which we report the presence of the higher frequency QPO (see Figure 3-4), we find that the lower QPO is significant at 3.5σ (24^{+33}_{-9} Hz FWHM, $2.8^{+0.9}_{-0.4}\%$ rms) and the higher QPO is significant at 7.8σ (56^{+8}_{-7} Hz FWHM, $6.2^{+0.4}_{-0.4}\%$ rms). Adding all six observations with the higher frequency QPO gives 22 trials for the 268 Hz QPO and 48 trials for the 188 Hz QPO (quoted significances are single-trial). For convenience, we now refer to the higher-frequency feature as the 268 Hz QPO, and to the lower-frequency feature as the 188 Hz QPO. Like the 268 Hz QPO, the 188 Hz QPO is also strongest in the 6–60 keV band.

We investigated how the strength of the QPOs as seen in the summed data (see Figure 3-4) depends on energy in the 2–6 keV, 6–15.3 keV, and 15.3–60 keV bands (corresponding to the bands in Table 3.1). For the 188 Hz QPO in the 6–15.3 keV band we measure: 185^{+3}_{-3} Hz (frequency), 18^{+17}_{-8} Hz (FWHM), $2.7^{+0.6}_{-0.4}\%$ rms (strength). Assuming the frequency and width measured in the 6–60 keV band, we place 95% confidence upper limits on the strength of this QPO in the 2–6 keV band of 1.3% rms, and in the 15.3–60 keV band of 3.9%. The 268 Hz QPO is not significant in the 2–6 keV band, and we place a 95% confidence upper limit on its strength of 5.8% rms. For the 268 Hz QPO in the 6–15.3 keV band we measure: 265^{+3}_{-3} Hz (frequency), 59^{+10}_{-8} Hz (FWHM), and $6.5^{+0.4}_{-0.5}\%$ rms (strength). In the 15.3–60 keV band we measure: 267^{+10}_{-14} Hz (frequency), 40^{+25}_{-17} Hz (FWHM), and $6^{+1}_{-1}\%$ rms (strength). Particularly for the 188 Hz QPO, the upper limits we obtain are not very constraining.

In order to test whether the 188 Hz and 268 Hz QPOs are present simultaneously, we divided the 18 PCA observations into three equal time segments and three even count rate slices, and analyzed these six power density spectra. In general, in full observations wherein we clearly detect the 268 Hz QPO, the high-count-rate power density spectra (and time segments with a relatively higher count rate) suggest two QPOs consistent with the 188 Hz and 268 Hz QPOs we report. In these segments, we do not find evidence for an alternating presence of the two peaks as a function of time or count rate, or for a single broad QPO feature which would suggest that a single QPO moves in frequency between 188–268 Hz. Individual features are usually not significant in these slices due to limited statistics and upper limits on the rms of features are not constraining. In lower-count-rate segments of full observations, and in segments of observations wherein the 268 Hz QPO is not detected, if a feature is suggested it is consistent with the 268 Hz QPO and not with a broader feature which might indicate a single moving QPO. We find no time segment or count-rate slice in which a feature consistent with the 188 Hz QPO is present individually, or stronger than a feature consistent with the 268 Hz QPO. Although our investigation indicates the QPOs are more likely simultaneous, it is nevertheless possible that we have observed only one QPO feature which moves in frequency on short timescales.

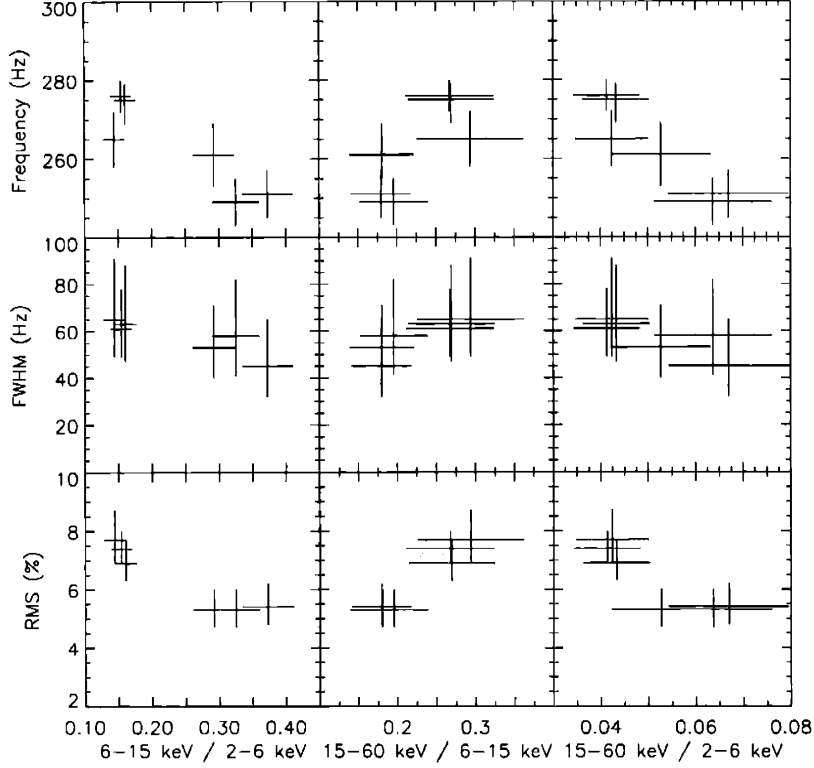


Figure 3-3 QPO frequency, FWHM, and rms plotted versus three hardness ratios. Displayed errors in QPO parameters and hardness ratios are 1σ confidence errors.

3.5 Discussion

The 268 Hz QPO likely represents the first detection of a high frequency QPO in outbursts of a transient BHC separated by a clear quiescent period. This QPO, and the 285 Hz QPO reported in the 1998–1999 outburst (Remillard et al. 1999a; Homan et al. 1999; Homan et al. 2001) are very likely the same QPO, as the frequency, FWHM, and strengths are very comparable. Yet, in a number of ways the 1998–1999 and 2000 outbursts of XTE J1550–564 are significantly different. In the former, a two-parameter model (e.g., \dot{m} and an as-yet unknown parameter) is required to describe the observed state transitions, the high frequency QPOs are correlated with spectral hardness, and the QPO parameters vary significantly with time. The 2000 outburst of XTE J1550–564 is consistent with a FRED lightcurve with state transitions accounted for only by variations in \dot{m} , the high frequency QPO parameters show no clear correlation with spectral hardness, and the QPO parameters vary little

over time. That the same high frequency QPO is observed in such different outbursts, however, likely indicates a fundamental similarity of the accretion flow environments.

We do not detect the high frequency QPO in the initial LS. This finding is consistent with timing studies of the LS following the outburst peak by Kalemci et al. (2001). If the QPO frequency is related to the Keplerian frequency at the innermost stable circular orbit around the black hole, this may suggest that the accretion disk is not filled entirely during the LS, and may recede slightly within the VHS/IS. Esin, McClintock, and Narayan (1997) describe an advection-dominated accretion flow (ADAF) model for BHCs. In this model, the accretion disk cannot cool efficiently at low \dot{m} and the accretion flow becomes quasi-spherical close to the BH (the inner disk radius is truncated at some distance from the marginally stable circular orbit). Thus, in this model, \dot{m} governs whether the inner region is hot and quasi-spherical, or an accretion disk. With the exception of the VHS, this model can describe the FRED lightcurve of GS 1124–68 (Ebisawa et al. 1994). As the 2000 outburst of XTE J1550–564 also follows a FRED lightcurve, it might be well-suited to ADAF modelling. The similarity of accretion flow environments implied by the detection of the same high frequency QPOs in the 1998–1999 and 2000 outbursts of XTE J1550–564 urges the modelling of non-FRED lightcurves with the ADAF model as well.

In the 1998–1999 outburst of XTE J1550–564, QPOs reported at roughly 185 Hz and 284 Hz (Remillard et al. 1999a; Homan et al. 1999) are likely not distinct, but are more likely the same high frequency QPO: Homan et al. 2001 note that within the hard states in the 1998–1999 outburst, the high frequency QPO may move between 102–284 Hz. Our investigation of the fast variability in the 2000 outburst of XTE J1550–564 suggests that two high frequency QPOs may be present simultaneously at approximately 188 Hz and 268 Hz.

This evidence for simultaneous high frequency QPOs in XTE J1550–564 is similar to the simultaneous high frequency QPOs in transient BHC/microquasar GRO J1655–40, at 450 Hz and 300 Hz (Strohmayer 2001a; the 300 Hz QPO was discovered earlier by Remillard et al. 1999b). In GRS 1915+105, a QPO at 40 Hz has been discov-

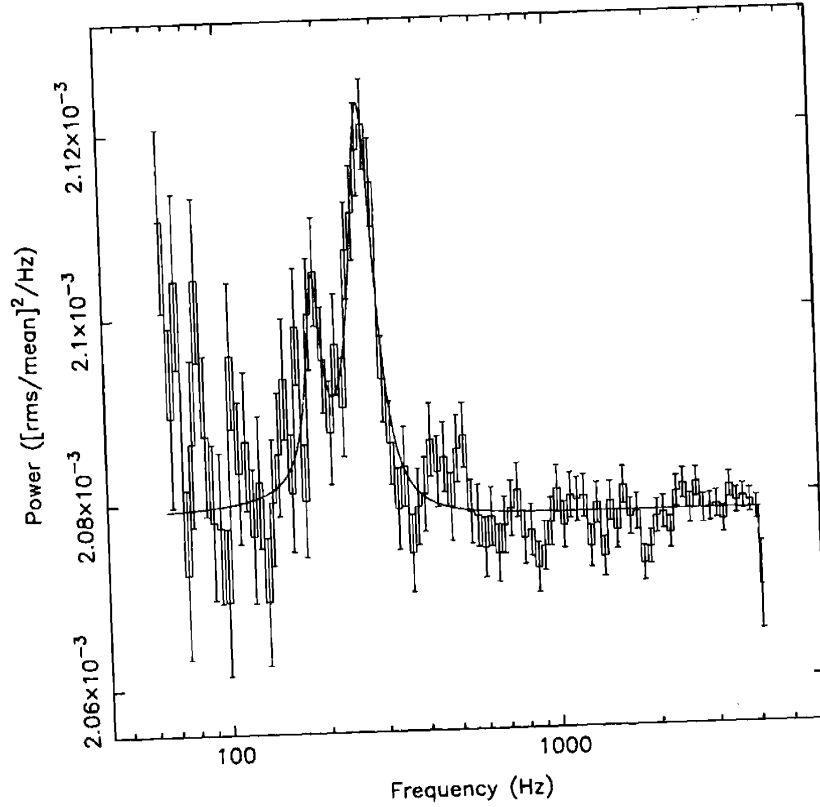


Figure 3-4 All observations with high frequency QPOs added together (6-60 keV, centroid frequencies not shifted). The higher-frequency QPO: 268 ± 3 Hz, 56^{+8}_{-7} Hz FWHM, $6.2^{+0.4}_{-0.4}\%$ rms, significant at 7.8σ . The lower-frequency QPO: 188 ± 3 Hz, 24^{+33}_{-9} Hz FWHM, $2.8^{+0.9}_{-0.4}\%$ rms, significant at 3.5σ . Quoted errors in QPO parameters are 1σ confidence errors, and significances are single-trial (here, there are 22 trials for the 268 Hz QPO, and 48 trials for the 188 Hz QPO).

ered (Strohmayer 2001b), present simultaneously with the previously-reported QPO at 67 Hz (Morgan, Remillard, and Greiner 1997). In all three systems, the QPO frequencies are roughly in the ratio of 3:2. In the case of GRO J1655-40, in the energy band where the 450 Hz QPO is strongest, it is stronger than the 300 Hz QPO. We do not find such a different dependence of QPO amplitude on energy for the two peaks in XTE J1550-564.

The presence of two high frequency QPOs in BHCs, present simultaneously, may be an emerging paradigm which will allow for new constraints on models for QPO production. If the QPOs observed in GRO J1655-40, GRS 1915+105, and XTE J1550-564 are analogous to the twin kHz QPOs often observed in neutron star systems, then models for the QPOs in neutron star systems which require reactions

with a solid stellar surface (e.g., the sonic point beat frequency model of Miller, Lamb, & Psaltis 1998) may be invalid. Models for QPOs in neutron star and BHC systems which instead rely upon General Relativistic frequencies at the inner accretion disk edge (e.g., the relativistic precession frequency model of Stella, Vietri, & Morsink 1999) are not excluded by the discovery of simultaneous high frequency QPOs in BHC systems.

If the 450 Hz QPOs represent a modulation at the innermost stable circular orbit of the accretion disk in GRO J1655–40, which is dynamically constrained to have a primary with mass of $M = 5.5 - 7.9 M_{\odot}$ (Shahbaz et al. 1999), this implies an angular momentum parameter $j = cJ/GM^2$ of 0.15–0.5 (Strohmayer 2001). Though certainly less concrete, the possibility of a black hole with significant angular momentum parameter had previously been inferred in spectral fits to data from GRO J1655–40 (Zhang, Cui, & Chen 1997; Balucinska-Church and Church 2000), and BHC XTE J1748–288 (Miller et al. 2001). The mass of the primary in XTE J1550–564 was constrained via optical work: $M_1 > 7.4 \pm 0.7 M_{\odot}$ (Orosz et al. 2001). Very recent work has found that the most likely mass of the compact object in XTE J1550–564 is $9.61 M_{\odot}$, with a 3σ range of $7.50 M_{\odot} \leq M_1 \leq 13.18 M_{\odot}$ (Orosz et al., private communication). Although the most likely mass suggests a black hole with non-zero j , the 3-sigma lower limit on the mass of the compact object does not require a black hole with significant angular momentum. This suggests that the presence of simultaneous high frequency QPOs may not be a unique signature of a black hole with non-zero angular momentum. The relativistic precession QPO model (Stella et al. 1999) suggests that these black hole systems may all have significant angular momentum. We look forward to combining the high-resolution spectroscopy available with *Chandra* and *XMM-Newton* with the timing resolution of *RXTE* to further probe the question of black hole spin.

Table 3.1 High Frequency QPOs in XTE J1550–564

Day (2000)	Frequency (Hz)	FWHM (Hz)	rms (6-60 keV) (%)	rms (2-60 keV) (%)	rms (2-6 keV) (%)	rms (6-15.3 keV) (%)	rms (15.3-60) (%)
120.4†	276(4)	61^{+17}_{-12}	7.4(6) [6.2 σ]	2.6(2)	2.0(2)	7.0(5)	4(4)
120.6†	275^{+4}_{-6}	40^{+25}_{-16}	$6.9^{+0.8}_{-0.6}$ [5.8 σ]	1.9(2)	1.5(2)	6.5(5)	7(2)
121.4†	265(7)	65^{+26}_{-16}	$7.7^{+1.0}_{-0.8}$ [4.8 σ]	3.2(2)	2.7(3)	7.4(7)	8(4)
124.8	261(8)	53^{+18}_{-13}	$5.3^{+0.7}_{-0.6}$ [4.4 σ]	2.1(3)	1.8(5)	5.0(6)	6(5)
126.5	249(6)	58^{+24}_{-17}	$5.6^{+0.7}_{-0.6}$ [4.7 σ]	2.6(2)	1.9(4)	5.4(4)	7(3)
129.4	251(6)	45^{+20}_{-13}	$5.4^{+0.8}_{-0.6}$ [4.5 σ]	2.0(4)	<2.7	4.7(6)	12(2)

Note. — QPO parameters for those observations wherein a high frequency QPO is detected. Detailed above are the day of the year 2000 on which the observation was made, and the Frequency, FWHM, and rms amplitude of each QPO, in 5 energy bands. The rms values noted in other bands are measured by fixing the frequency and FWHM to that measured in the band where the QPO is most significant. Errors are 1σ confidence intervals, customary for timing studies. † denotes observations made in an instrumental mode that samples the full PCA energy bandpass at a slightly different binning. The bands for these observations are (in the order that appears left-to-right above): 8-57 keV, 2-57 keV, 2-8 keV, 8-15.3 keV, and 15.3-57 keV. 95% confidence upper limits (6–60 keV) on the strength of a high frequency QPO in observations made on days 114.6, 116.1, 118.2, and 123.7 range between 2.7-5.2% rms. We find upper limits in the range of 5.1–6.4% rms for a high frequency QPO in observations made on days 125.2, 126.8, 127.4, 128.4, 128.9, 130.8, 131.6, and 132.4 (any feature would be significant at less than 2σ).

3.6 Bibliography

- Balucinska-Church, M. and Church, M. J. 2000, MNRAS, 312, L55
- Corbel, S., et al. 2001, ApJ, in press
- Ebisawa, K. et al. 1994, PASJ, 46, 375-394
- Esin, A. A. McClintock, J. E. and Narayan, R. 1997, ApJ, 489, 865
- Hannikainen, D. et al. 2000, in "Proceedings of the Third Microquasar Workshop: Granada Workshop on galactic relativistic jet sources", ed. A. J. Castro-Tirado, J. Greiner, and J. M. Paredes, Astrophysics and Space Science, in press
- Homan, J. Wijnands, R. and van der Klis, M. IAU Circ., 7121
- Homan, J., et al. 2001, ApJ, 132, 377S
- Jain, R. K. Bailyn, C. D. Orosz, J. A. McClintock, J. E. Sobczak, G. J. and Remillard, R. A. 2001, ApJ, 546, 1086
- Kalemci, E., Tomsick, J. A., Rothschild, R. A., Pottschmidt, K., & Kaaret, P., 2001, ApJ subm., astro-ph/0105395
- Levine, A. M. Bradt, H. Cui, W. Jernigan, J. G. Morgan, E. H. Remillard, R. Shirey, R. E. & Smith, D. A. 1996, ApJ, 469, L33
- Masetti, N. and Soria, R. 2000, IAU Circ., 7399
- Miller, J. M. et al. 2001a, ApJ, 546, 1055
- Miller, J. M. et al. 2001b, MNRAS, submitted, astro-ph/0103215
- Miller, M. C. Lamb, F. K. and Psaltis, D. 1998, ApJ, 508, 791
- Mitusda, K. et al. 1984, PASJ, 36, 741
- Morgan, E. H. Remillard, R. A. & Greiner, J. 1997, ApJ, 482, 993
- Orosz, J. A. van der Klis, M. McClintock, J. E. Jain, R. K. Bailyn, C. D. & Remillard, R. A. 2001, ATEL 70
- Remillard, R. A. McClintock, J. E. Sobczak, J. G. Bailyn, C. D. Orosz, J. A. Morgan, E. H. and Levine, A. M., 1999a, ApJ, 517, L127
- Remillard, R. A. Morgan, E. H. McClintock, J. E. Bailyn, C. D. and Orosz, J. A. 1999b, ApJ, 522, 397
- Shahbaz, T. van der Hooft, F. Casares, J. Charles, P. A. & van Paradijs, J. 1999, MNRAS, 306, 89
- Smith, D. A. 1998, IAU Circ., 7008
- Smith, D. A. Levine, A. M. Remillard, R. A. Fox, D. & Shaefer, R. 2000, IAU Circ., 7399
- Sobczak, G. J. et al. 2000, ApJ, 544, 933
- Stella, L. Vietri, M. and Morsink, S. M. 1999, ApJ, 524, L63
- Strohmayer, T. E. 2001a, ApJ, 522, L49
- Strohmayer, T. E. 2001b, ApJ, in press, astro-ph/0105338
- Tanaka, Y. and Lewin, W. H. G. 1995, in X-ray binaries, ed. W. H. G. Lewin, J. van Paradijs, & E. P. J. van den Heuvel (Cambridge: Cambridge Univ. Press), 126
- Tomsick, J. A. Smith, E. Swank, J. Wijnands, R. and Homan, J. 2001, IAU Circ., 7575
- van der Klis, M. Wijnands, R. Horne, K. & Chen, W. 1997, ApJ, 481, L97
- Zhang, S. N. Cui, W. & Chen, W. ApJ, 482, L155

Chapter 4

Chandra and *RXTE* Spectroscopy of the Galactic Microquasar XTE J1550–564 in Outburst

This chapter is based on the original paper:

“*Chandra* and *RXTE* Spectroscopy of the Galactic Microquasar XTE J1550–564 in Outburst,” Miller, J. M., Marshall, H. L., Wijnands, R., Di Matteo, T., Fox, D. W., Kommers, J., Pooley, D., Belloni, T., Casares, J., Charles, P. A., Fabian, A. C., van der Klis, M., and Lewin, W. H. G., 2002, submitted to *The Monthly Notices of the Royal Astronomical Society*,

with the permission of the publisher, Blackwell Science.

4.1 Abstract

On two occasions, we obtained nearly simultaneous $\simeq 4$ kilosecond snapshot observations of the Galactic black hole and microquasar XTE J1550–564 with *Chandra* and *RXTE* near the peak of its May, 2000 outburst. The low-energy sensitivity of *Chandra* and the resolution of the High Energy Transmission Grating Spectrometer (HETGS),

coupled with the broad energy range and large collecting area of *RXTE*, have allowed us to place constraints on the outburst accretion flow geometry of this source in the “intermediate” X-ray state. The 0.65–25.0 keV continuum spectra are well-described by relatively hot ($kT \simeq 0.8$ keV) accretion disk and hard ($\Gamma \simeq 2.3$) coronal power-law components. Broad, relatively strong Fe $K\alpha$ emission line ($W_{K\alpha} \simeq 170$ eV) and smeared absorption edge components consistent with Fe XXV are strongly required in joint spectral fits. The resolution of the *Chandra*/HETGS reveals that the broad Fe $K\alpha$ emission lines seen clearly in the individual *RXTE* spectra are not due to an intrinsically narrow line.

4.2 Introduction

XTE J1550–564 is a transient Galactic black hole. At the time of writing, four outbursts — each separated by clear quiescent periods — have been observed from this source. Radio observations during its 1998–1999 outburst revealed optically thick emission, with apparent superluminal motion ($v_{\text{jet}} > 2c$) (Hannikainen et al. 2000). As a result, XTE J1550–564 was further classified as a “microquasar.” Recently, Orosz et al. (2002) have constrained the mass of the black hole primary in this system through optical observations of the source in quiescence ($9.86 M_{\odot} < M_{BH} < 11.58 M_{\odot}$).

The accretion flow geometry of Galactic black holes in outburst may change considerably with the mass accretion rate (\dot{m}), which is often assumed to be traced directly by the soft X-ray luminosity (see, however, Homan et al. 2001). In transient outbursts, the soft X-ray luminosity may suddenly rise, and decay over a period ranging between days and months; from quiescence to the outburst peak, the luminosity may increase by a factor of 10^6 or more. In all such systems, periods of characteristic X-ray timing and spectral behaviors and correlated multi-wavelength properties are observed which are known as “states” (for reviews, see Tanaka & Lewin 1995, Belloni 2001, Done 2002; for a critical discussion see Homan et al. 2001). The existence of states likely indicates that only certain accretion modes and geometries are allowed

in Galactic black hole systems.

At luminosities below $L_X \sim 10^{34-35} \text{ erg s}^{-1}$, the geometry is particularly uncertain; the accretion disk may be recessed to $R_{in} \simeq 10^{2-4} R_g$, $R_g = GM_{BH}/c^2$ (see, e.g., Esin, McClintock, & Narayan 1997; for a competing description see Ross, Fabian, & Young 1999). In contrast, near peak outburst luminosity — $L_X \sim 10^{37-38} \text{ erg s}^{-1}$ — there is general agreement that the accretion disk may extend to the marginally stable circular orbit. In such cases, the disk may serve as a probe of the general relativistic regime around the black hole.

This regime can be explored through continuum spectroscopy (e.g., through the multi-color disk blackbody model, Mitsuda et al. 1984), studies of high frequency quasi-periodic oscillations (QPOs) in the X-ray lightcurve (likely associated with the Keplerian frequency at the marginally stable circular orbit), and through studies of Fe K α line profiles and X-ray reflection spectra (Fabian et al. 1989, Miller et al. 2002a; George & Fabian 1991, Ross, Fabian, & Young 1999). XTE J1550–564 and GRO J1655–40 are the only two dynamically-constrained Galactic black holes for which each of these tools has revealed evidence of an accretion disk at the marginally stable orbit, and perhaps evidence of black hole spin (Sobczak et al. 1999, Sobczak et al. 2000; Remillard et al. 1999a, Homan, Wijnands, & van der Klis 1999; Strohmayer 2001, Miller et al. 2001a).

We obtained two nearly-simultaneous observations of XTE J1550–564 with *Chandra* and *RXTE* near the peak of its May, 2001 outburst, at source luminosities of $L_X \simeq 0.8 \times 10^{38} \text{ erg s}^{-1}$ and $L_X \simeq 1.0 \times 10^{38} \text{ erg s}^{-1}$ (0.65–10.0 keV) for $d = 5.3 \text{ kpc}$ (Orosz et al. 2002). Our short $\simeq 4$ kilosecond observations with *Chandra* were designed for a much brighter source; the sensitivity achieved does not permit detailed studies of the Fe K α line region. However, we are able to confirm that broad Fe K α emission lines in the *RXTE* spectra are not due to an intrinsically narrow line.

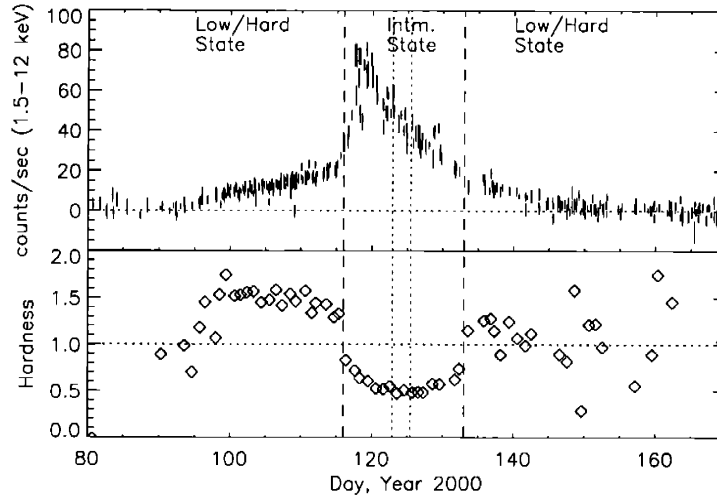


Figure 4-1 The ASM 1.5-12 keV lightcurve and (5-12 keV)/(3-5 keV) count-rate ratio for the April-May 2000 outburst of XTE J1550–564. Dotted vertical lines indicate the approximate start times of our *Chandra* observations. Dashed vertical lines separate X-ray states. State identifications based on the ASM hardness ratio, and radio observations reported by Corbel et al. (2001).

4.3 Outburst History and Observation

XTE J1550–564 was discovered on 7 September 1998 (Smith 1998), by the *All Sky Monitor* (ASM) aboard the *Rossi X-ray Timing Explorer* (RXTE). A radio (Campbell-Wilson et al. 1998) and optical counterpart (Orosz, Bailyn, & Jain 1998) was quickly identified. The ensuing outburst lasted until June 1999, and displayed some of the most remarkable behavior yet seen in an X-ray nova, e.g. an initial flare which reached a flux level equivalent to 6.8 Crab (1.5–12 keV, *RXTE*/ASM), very rapid state transitions, and strong (7% rms) QPOs at frequencies as high as 285 Hz (Sobczak et al. 2000, Homan et al. 2001).

On 2 April, 2000, new source activity was noticed by the *RXTE* ASM (Smith et al. 2000). XTE J1550–564 was active in X-rays for nearly 70 days thereafter, and reached a peak flux of ~ 1 Crab (ASM, 1.5-12 keV); it was also seen out to 300 keV with BATSE aboard *CGRO*, and simultaneously in optical bands (Masetti & Soria 2000, Jain & Bailyn 2000). Spectrally-inverted radio emission, likely from a compact jet, is detected in the low/hard state, as well as a possible discrete ejection event at the low/hard – intermediate state transition (Corbel et al. 2001). The ASM light

curve and (5–12 keV)/(3–5 keV) hardness ratio of this outburst is shown in Figure 4-1. The lightcurve of the first outburst of XTE J1550–564 departed radically from a typical profile (Homan et al. 2001), but the second outburst is more similar to a fast-rise exponential-decay (or, “FRED”) envelope.

Near the peak of this outburst, Miller et al. (2001a) report simultaneous high-frequency QPOs at 188 Hz and 276 Hz. These QPOs appear in an approximate 2:3 ratio like the 300 Hz and 450 Hz QPOs found in observations of GRO J1655–40 (Strohmayer et al. 2001). If these QPOs are tied to the Keplerian frequency at the marginally stable circular orbit, they provide evidence for black hole spin. Tomsick et al. (2001a) and Kalemci et al. (2001) discuss the spectral and timing properties, respectively, of the declining phase of this outburst.

On 28 January, 2001, *RXTE* found XTE J1550–564 to be in the low/hard state, with timing noise of 40% rms and a spectrum well-described by a power-law with $\Gamma = 1.52$ (Tomsick et al. 2001b). On 10 January, 2002, *RXTE* again found XTE J1550–564 to be in the low/hard state. Belloni et al. (2002) report that the timing and spectral properties typical of the low/hard state in this short outburst.

The second outburst of XTE J1550–564 met the trigger criteria for our approved *Chandra* AO-1 target of opportunity (TOO) program, as well as our *RXTE* AO-5 TOO program. In all, we made seven observations of XTE J1550–564 with *Chandra* (18 observations with *RXTE*). Of these, here we report on the first two observations only (see Table 4.1), when the source was brightest. Of the remaining *Chandra* observations, in two cases the HETGS failed to insert, and in two other cases the source intensity was too faint for our graded, continuous-clocking observational mode to yield good spectra, but the source was clearly detected (for a good discussion of continuous clocking mode, see Marshall et al. 2001). Imaging data from a final observation will be presented in separate work.

Table 4.1 *Chandra* and *RXTE* Observation Log

No.	Obs.ID	Date, UT	Start Time	Day (year 2000)	Exp. (s)	Good Time (s)
C1	680	05/03/00	21:10:40	122.9	3380	2670
C2	681	05/06/00	12:54:09	125.5	3770	2170
R1	50134-02-04-00	05/03/00	16:33:20	122.7	4860	4860
R2	50134-02-06-00	05/06/00	12:50:08	125.5	3960	3960

Note. — These observations were made shortly after outburst maximum, during the “intermediate” X-ray state. “Good Time” is non-slewing observation time. C1 and C2 are the *Chandra* observations, R1 and R2 are the *RXTE* observations.

4.4 Data Reduction

4.4.1 *RXTE* Modes and Selections

The *RXTE* data we report here were obtained through pointed observations of the proportional counter array (PCA), which consists of five individual proportional counter units (PCUs). Due to gain uncertainties in PCU-0 following the loss of its propane layer, we exclude data from this detector. With this exception, we include data from all layers of all active detectors (see Table 4.1; for observation R1 this includes PCUs 2, 3, and 4; for observation R2 this includes PCUs 1, 2, 3, and 4). The data was reduced using the LHEASOFT suite (version 5.1). We apply the standard “goodtime” and detector “deadtime” corrections. The background was calculated using the “bright source” model within LHEASOFT. Response matrices were made using the tool “pcarsp.”

At the resolution of the PCA, the spectrum of the Crab nebula is known to be a simple power-law. We fit a spectrum from the Crab obtained on 14 May 2000 (as close to our observations as possible), with a power-law index for the pulsar component of 1.8 (Knight, 1982) and a column density of $3.2 \times 10^{21} \text{ cm}^{-2}$ (Massaro et al, 2000). Below 3 keV, residuals are very large, and so we fix 3 keV as our lower fitting bound. Similarly, above 25 keV, residuals in fits to the Crab are large, and our data from XTE J1550–564 becomes dominated by the background flux, so we

adopt this energy as an upper fitting bound. As we wish to address the iron line region in XTE J1550–564, we consider residuals as a function of energy in power-law fits to this Crab observation. We find that with the addition of 0.4% systematic errors in the 3–8 keV band, and 0.8% systematic errors in the 8–25 keV band, the reduced χ^2 fitting statistic drops to 1.0 (similar results were obtained by Tomsick et al. 2001a). Therefore, we add this energy-dependent systematic error to our PCA data from XTE J1550–564.

4.4.2 *Chandra* Modes and Selections

XTE J1550–564 was observed with the *Chandra* HETGS using the ACIS-S CCD array operating in continuous clocking (CC) mode. Because XTE J1550–564 had flared to 6.8 Crab (1.5–12 keV) during its 1998 outburst, avoiding damage to the ACIS array was a paramount concern. To this end, we employed a large dither (20" amplitude) to spread the most intense parts of the zeroth order over many pixels. Furthermore, the zeroth order aim point was shifted toward the top of the chip via a SIM-Z translation of +10.0mm from the nominal S3 aim point. A +1.33' Y-offset was used to place the iron K_α region of the HEG –1 order on ACIS-S3. Finally, we blocked-out rows 367–467, eliminating any read-out of zeroth-order photons. This blocking acted to limit any telemetry saturation that would result from the zeroth-order counts. The CC mode was employed to limit pile-up of the dispersed spectrum and to achieve 3 msec time resolution.

As our observing mode is non-standard, the data is not well-suited to reduction via the tools available in the CIAO suite. We have managed to build robust, custom software to reduce and analyse our data. We first correct for bad aspect times (e.g. slewing, see Table 4.1). The events are then examined in projected chip-x space to correct for “hot” pixels which report erroneously large event numbers (a list of bad pixels is available through CIAO). ACIS-S4 sometimes produces “streaks” which appear in the ACIS chip image (see <http://asc.harvard.edu>); the events were removed using a 50 column median filter, rejecting deviations greater than 3σ . The spacecraft dither pattern is removed by calculating the mean chip-x position as a function of

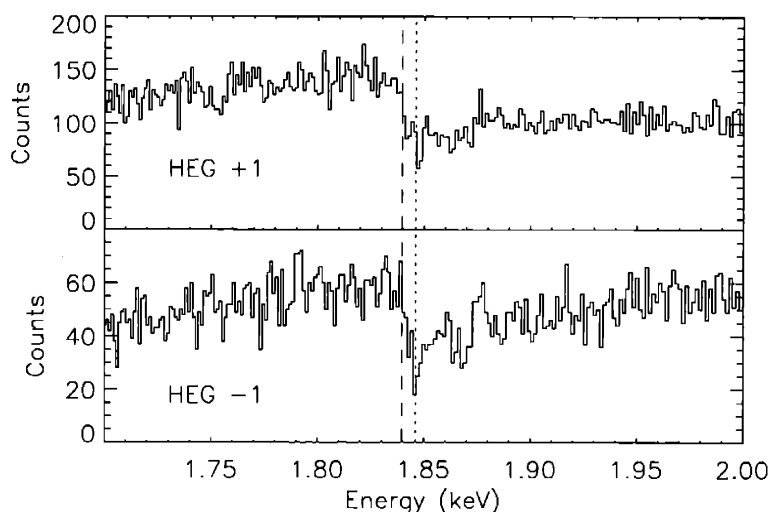


Figure 4-2 The count spectrum of XTE J1550–564 near the instrumental silicon absorption edge. The dashed line is the laboratory edge energy (1.8395 keV). The dotted line is the edge minimum, which we can align to within the instrumental resolution. This provides an effective means of establishing the zeroth-order position, and therefore energy as a function of position on the ACIS-S array. This is necessary as we blocked the zeroth-order photons with a spatial window to prevent telemetry saturation.

time, which is a sine wave. We are able to interpolate the dither-corrected chip x position of each event by removing this sine wave. With the dither removed, it is possible to calculate the wavelength corresponding to each chip- x value via the grating equation. A linear gain correction is performed on each of the four independent read-out and amplifier nodes on each ACIS-S chip. Finally, we extract first-order MEG and HEG events and background regions, and apply the appropriate response matrices.

Indeed, although we have blocked-out the zeroth-order photons, we are able to accurately locate the position of the zeroth-order, and therefore able to convert accurately from chip x space to wavelength or energy space via the grating equation. To do this, we make use of the fact that the ACIS chips are silicon-based, and that silicon has an absorption edge at 1.8395 keV. For an assumed zeroth-order position, then, we can examine the location of this edge in the HEG +1 and HEG –1 spectra (which are on opposite sides of the zeroth-order position) and iterate the assumed zeroth-order position until the edge is seen at the same energy in both (see Figure 4-2).

As per Marshall et al. (2001), we perform an effective area correction, and add 5% systematic errors to the dispersed spectra. Due to the fact that our *Chandra* observations were offset towards the top of the ACIS-S array, less of the HEG -1 and MEG $+1$ orders were read-out in comparison to the HEG $+1$ and MEG -1 orders. Moreover, with the spacecraft dither, the portions of the HEG -1 and MEG $+1$ spectra dispersed far from the zeroth order were moved onto and off of the ACIS-S array. This is reflected in the spectra we obtained from the truncated orders, which show significant deviations from the shape expected based on the spectra obtained with *RXTE*. Therefore, we only consider the HEG $+1$ and MEG -1 spectra from our *Chandra* observations.

Even after rebinning by a factor of 10, flux bins below 0.65 keV in the MEG -1 spectrum are consistent with zero. The HEG $+1$ spectrum suffers from low effective area below 1.0 keV, displaying a flux trend inconsistent with the MEG -1 spectrum. These energies serve as lower fitting bounds. We exclude data from regions near gaps in the ACIS-S CCD array. In the MEG -1 spectrum we exclude the 0.74–0.80 keV band. There is another gap between 2.2–3.0 keV in this grating order, and at higher energies the effective area of the HEG is higher. We therefore adopt 2 keV as an upper fitting bound for the MEG -1 order. We exclude the 1.3–1.4 keV and 3.2–4.2 keV bands in the HEG $+1$ spectrum, and set 10.0 keV as an upper fitting bound (this is the effective upper energy limit of the HEG).

4.5 Analysis and Results

The reduced spectra were analyzed using XSPEC version 11.1.0 (Arnaud et al. 1996). All errors quoted in this paper reflect the difference between the best-fit value, and the value of the parameter at its 90% confidence limits.

We fit the spectra from the *Chandra*/HETGS and the *RXTE*/PCA spectra simultaneously; spectra R1 and C1 are nearly simultaneous, and spectra R2 and C2 are simultaneous (see Table 4.1). Joint fits are desirable to characterize the continuum emission, as the range of the *Chandra*/HETGS is well-suited to measuring the soft

Table 4.2 Joint Spectral Fit Results

Obs.	N_H (10^{21} cm^{-2})	kT_{MCD} (keV)	N_{MCD} (10^3)	Γ_{pl}	N_{pl}	N_{line} (10^{-3})	EW_{line} (eV)	τ_{edge}	red. χ^2
R1+C1	$8.0^{+0.2}_{-0.1}$	0.790(8)	2.1(1)	2.36(1)	2.38(7)	5.7(7)	160 ± 20	$1.34^{+0.06}_{-0.07}$	0.996
R2+C2	$8.0^{+0.4}_{-0.3}$	$0.753^{+0.007}_{-0.008}$	3.2(2)	2.32(1)	$2.90^{+0.07}_{-0.08}$	$7.7^{+0.7}_{-0.9}$	180 ± 20	$1.39^{+0.06}_{-0.05}$	1.017

Note. — The results of fitting the *RXTE*/PCA and *Chandra*/HETGS spectra (rebinned by a factor of 10) jointly. There are 334 bins and 321 degrees of freedom for each joint fit. The model consists of photoelectric absorption, a multi-color disk blackbody component, a power-law component, and a broad Gaussian plus smeared edge (“smedge”) in the iron K_α region. The Gaussian and smeared edge energies are fixed at 6.68 keV and 8.83 keV, respectively, corresponding to Fe XXV. Neutral Fe features and spectral models without a broad line and edge give significantly worse fits to the data.

spectral component expected from an accretion disk, and the *RXTE*/PCA range is well-suited to constraining the hard power-law spectral component.

Fits with a model consisting of interstellar absorption (“phabs” in XSPEC), a multi-color disk (MCD) blackbody component (Mitsuda et al. 1984), and a power-law component did not yield acceptable fits ($\chi^2/\nu > 5$). Fits with Comptonization models such as “compTT” (Titarchuk 1994) and the “bulk motion Comptonization” model (Shrader & Titarchuk 1999) gave slightly worse fits. This is principally due to strong residuals in the Fe K_α region. We therefore add a broad Gaussian line and smeared edge (“smedge” within XSPEC; Ebisawa et al. 1994). This is the same model used by Sobczak et al. (2000) in fits to the 1998–1999 outburst of XTE J1550–564, and to be consistent with this prior work we fix the width of the edge to 7.0 keV, and the width (FWHM) of the line to 1.2 keV. The addition of a relatively neutral line plus edge combination ($E_{\text{line}} = 6.40$ keV, $E_{\text{edge}} = 7.1$ keV) does improve the fit considerably ($\chi^2/\nu \simeq 3$), but this is not an acceptable fit. When the Gaussian and smeared edge energies are allowed to float, values consistent with helium-like Fe XXV ($E_{\text{line}} = 6.68$ keV, $E_{\text{edge}} = 8.83$ keV) are preferred statistically. We fix these values in our final model, and acceptable fits are achieved: $\chi^2/\nu = 0.996$ (R1+C1), $\chi^2/\nu = 1.017$ (R2+C2). As a first test of whether or not the line is intrinsically narrow, we also made fits with a Gaussian of zero width. The fit obtained is not statistically

Table 4.3 Unabsorbed Fluxes Measured in Joint Spectral Fits

Obs.	Range (keV)	Total (10^{-8} cgs)	MCD (10^{-8} cgs)	Power-law (10^{-8} cgs)	Line (10^{-11} cgs)
R1+C1	0.5–10.0	$2.4^{+0.2}_{-0.1}$	$1.5^{+0.1}_{-0.1}$	$0.90^{+0.02}_{-0.03}$	$6.1^{+0.7}_{-0.7}$
R1+C1	0.65–25.0	$2.3^{+0.1}_{-0.1}$	$1.4^{+0.1}_{-0.1}$	$0.89^{+0.02}_{-0.03}$	$6.1^{+0.7}_{-0.7}$
R2+C2	0.5–10.0	$3.0^{+0.2}_{-0.2}$	$1.9^{+0.1}_{-0.1}$	$1.12^{+0.02}_{-0.03}$	$8.3^{+0.7}_{-0.8}$
R2+C2	0.65–25.0	$2.9^{+0.1}_{-0.2}$	$1.7^{+0.1}_{-0.1}$	$1.12^{+0.03}_{-0.04}$	$8.3^{+0.7}_{-0.8}$

Note. — The unabsorbed fluxes measured via the fits detailed in Table 2. We quote fluxes for both the “standard” soft X-ray band (0.5–10.0 keV) and the full fitting range (0.65–25.0 keV) for joint fits to the *Chandra* and *RXTE* data; they are very similar. For a distance of 5.3 kpc (Orosz, priv. comm.), XTE J1550–564 was observed at luminosities of approximately 8×10^{37} and 1×10^{38} ergs/sec (0.65–10 keV) in the first and second observations, respectively.

acceptable ($\chi^2/\nu \simeq 5$), suggesting that the observed line is not merely instrumentally broadened.

We report the best-fit model parameters in Table 4.2; the data and the best-fit model is shown in Figure 4-3. We measure an equivalent neutral hydrogen column density of $N_H = 8.0^{+0.4}_{-0.3} \times 10^{21} \text{ cm}^{-2}$. Relatively high inner disk color temperatures are found with the MCD model ($kT = 0.790 \pm 0.008 \text{ keV}$ and $kT = 0.753 \pm 0.008 \text{ keV}$, respectively). We measure power-law indices of 2.36 ± 0.01 and 2.32 ± 0.01 , respectively. The unabsorbed fluxes measured via our model are listed in Table 4.3; in the energy range we consider the disk flux is approximately 60% of the total. These spectral results are consistent with the XTE J1550–564 being in the intermediate state at the time of our observations (this is confirmed by X-ray timing results, see Miller et al. 2001a). The broad Fe $K\alpha$ emission line is relatively strong and highly significant; we measure equivalent widths of $160 \pm 20 \text{ eV}$ and $180 \pm 20 \text{ eV}$, respectively. We measure the optical depth of the smeared edge to be 1.34 ± 0.07 and 1.39 ± 0.06 , respectively.

For a known source distance and inclination, the MCD model gives a measure of the inner disk radius via the model normalization. Assuming the mean values for the black hole mass ($M_{BH} \simeq 10.7 M_\odot$), system inclination ($i \simeq 73.1^\circ$), and distance ($d \simeq 5.3 \text{ kpc}$) reported by Orosz et al. (2002), we measure inner disk radii of $\simeq 45 \text{ km}$

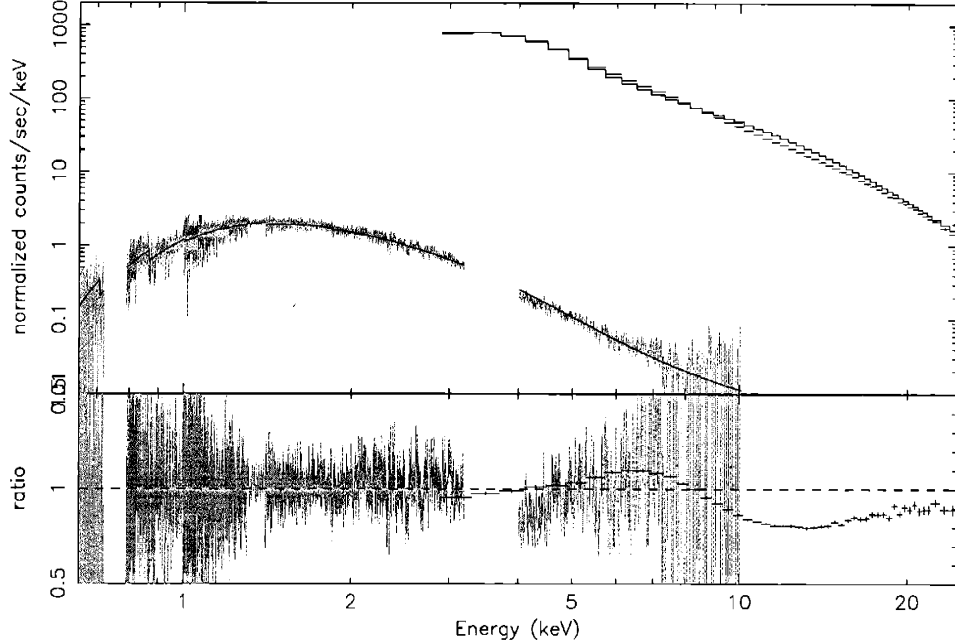


Figure 4-3 The *Chandra* and *RXTE* spectra (C1 and R1) fit with the model described in Table 4.2, and the resulting data/model ratio. The *Chandra* data are shown in gray and cover the 0.65–10.0 keV band, and the *RXTE* data in blue and cover the 3.0–25.0 keV band; the model is shown in red. The Gaussian line normalization and smeared edge depth have been set to zero to show their strengths more clearly. For visual clarity, the *Chandra* spectra have been rebinned by a factor of two and are not plotted with systematic errors. Gaps in the *Chandra* spectra are due to gaps in the CCD array which could not be recovered in this observing mode. The spectra and data/model ratio obtained from fits to the observation made 2.5 days later (C2 and R2, see Table 4.1 and Table 4.2) are indistinguishable in this representation.

and $\simeq 56$ km (corresponding to $R_{in} \simeq 2.8 R_g$ and $R_{in} \simeq 3.5 R_g$, respectively). As these values are within the marginally stable circular orbit ($R_{in} = 6 R_g$) for a non-spinning (Schwarzschild) black hole, they may imply a black hole with significant angular momentum in XTE J1550–564.

4.5.1 Testing for narrow features.

To further examine whether or not a single emission line might merely be smeared by the PCA response to produce the broad Fe $K\alpha$ line required in joint fits, we calculated the 95% confidence upper-limits on the strength of single-bin emission lines in the *Chandra*/HETGS spectra (see Figure 4-4). Due to Auger destruction, intermediate Fe ion species are not likely to be observed; relatively few narrow Fe $K\alpha$ lines (e.g., Fe I, XXV, XXVI at 6.40, 6.68, and 6.97 keV, respectively) are expected. It is clear

that the upper-limits on line features at these energies are a fraction of the $\simeq 170$ eV equivalent width of the broad lines required in joint fits. The spectra we obtained are of too coarse a sensitivity to detect narrow emission or absorption features like those found in the high/soft state of XTE J1650–500 (Miller et al. 2002b).

4.6 Discussion

We have analyzed spectra from two nearly-simultaneous *Chandra*/HETGS and *RXTE* observations of the Galactic microquasar XTE J1550–564. We jointly fit the 0.65–25.0 keV spectra with a continuum model consisting of two components: a multi-color disk blackbody (likely from an accretion disk) and a power-law (likely from a corona). This simple model described the data better than Comptonization models. The data strongly require the addition of a broad Gaussian emission line and smeared edge features consistent with Fe XXV (see Table 4.2). This model may be regarded as an approximation to a full reflection model in the 0.65–25.0 keV band.

The multi-color disk blackbody model yields a measure of the inner accretion disk edge. Our fits give inner disk radii of $R_{in} \simeq 2.8 R_g$ and $R_{in} \simeq 3.5 R_g$, which suggests that XTE J1550–564 may harbor a spinning black hole. If the Shimura & Takahara (1995) color correction is applied ($R_{in,ST} = f^2 \times R_{in,MCD}$, $f = 1.7$ for stellar-mass black holes) black hole spin is not required. However, this correction may be overly simplified. Merloni, Fabian, & Ross (2000) have detailed more systematic difficulties with the inner disk estimates of this model, but suggest that the MCD model may give acceptable inner disk measures at high \dot{m} . The 284 Hz QPO found in the 1998–1999 outburst of this source (Homan et al. 1999, 2001) and the 276 Hz QPO found in this outburst (Miller et al. 2001a) also suggest a spinning black hole.

Broad Fe K α emission line studies may provide another means of diagnosing the accretion flow geometry and black hole spin, as these lines are plausibly produced by irradiation of the inner disk (Fabian et al. 1989). We find that lines with widths of 1.2 keV (FWHM) adequately describe our data. Intrinsically narrow lines (with widths fixed at zero, as per a line with a FWHM less than the *RXTE*/PCA resolution)

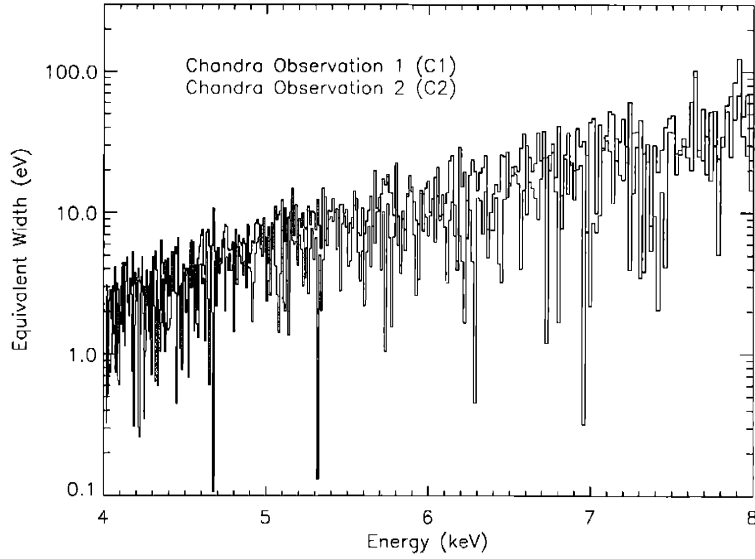


Figure 4-4 The 95% confidence upper-limits on the equivalent width of single-bin emission lines in the Fe $K\alpha$ line region. In calculating the upper-limits, broad emission line and smeared edge components are not included in the fit. It is clear that the $W_{K\alpha} \simeq 170$ eV line required in joint fits is not likely due to an intrinsically narrow line, or even a few lines.

give significantly worse fit results. Moreover, the *Chandra*/HETGS spectra confirm that the line is not likely due to an intrinsically narrow line which is smeared by the resolution of the *RXTE*/PCA (see Figure ??). The sensitivity achieved with our *Chandra*/HETGS snapshot observations is not sufficient to constrain the parameters of more sophisticated line models which can estimate the inner disk extent more directly (and thereby black hole spin, e.g. Miller et al. 2002a). The 1.2 keV (FWHM) width we adopt in fits with a Gaussian model is not broad enough to require black hole spin, but it does suggest significant Doppler shifting. Compton broadening may also contribute to the observed line width.

Our best-fit spectral model is the same as that adopted by Sobczak et al. (2000) in fits to *RXTE* spectra from the 1998–1999 outburst. The parameters we measure are broadly consistent with those reported previously when XTE J1550–564 was found to be in the very high or intermediate states. The properties of these states are quite similar, and they are only be distinguished by relative luminosity (if multiple such states are observed, the most luminous may be called the “very high” state, and the

others “intermediate” states). The Fe $K\alpha$ emission line equivalent widths we measure ($W_{K\alpha} = 160 \pm 20$ and 180 ± 20 eV) are consistent with the strongest lines reported by Sobczak et al. (2000). We speculate that the sensitivity and energy range of the *Chandra*/HETGS spectra have allowed for a better characterization of the continuum spectrum, and therefore a better characterization of the line parameters as well.

At present, few very high and intermediate states have been observed relative to the more common high/soft and low/hard states. The spectra we have observed are similar to other very high and/or intermediate states observed in the *RXTE* and *BeppoSAX* era, including: XTE J1650–500, GRO J1655–40, GRS 1739–278, XTE J1748–288, and XTE J2012+381 (Miller et al. 2002, Sobczak et al. 1999, Borozdin et al. 1998, Miller et al. 2001b, Campana et al. 2002).

4.7 Bibliography

- Arnaud, K. A., 1996, in ASP Conf. Ser. 101, *Astronomical Data Analysis Software and Systems V.*, eds. G. H. Jacoby & J. Barnes (San Francisco: ASP), 17
- Belloni, T., in "X-ray Emission from Accretion onto Black Holes," 2001, eds. T. Yaqoob & J. H. Krolik, available at <http://www.pha.jhu.edu/groups/astro/workshop2001/>
- Belloni, T., Colombo, A. P., Homan, J., Campana, S., van der Klis, M., 2002, *A & A*, in press
- Borozdin, K., N., Revnivtsev, M. G., Trudolyubov, S. P., Aleksandrovich, N. L., Sunyaev, R. A., & Skinner, G. K., 1998, *AstL*, 24, 435
- Campbell-Wilson, D., McIntyre, V. Hunstead, R., Green, A., Wilson, R. B., & Wilson C. A., 1998 *IAU Circ.*, 7010
- Campana, S., et al., 2002, *A & A*, 384, 163
- Corbel, S., et al., 2001, *ApJ*, submitted
- Done, C., 2002, in "Philosophical Transactions of the Royal Society," Series A: Mathematical, Physical, and Engineering Sciences, astro-ph/0203246
- Ebisawa, K., et al., 1994 *PASJ* 46, 375-394
- Esin, A. A., McClintock, J. E., and Narayan, R., 1997, *ApJ* 489, 865
- Fabian, A. C., Rees, M. J., Stella, L., & White, Ne. E., 1989, *MNRAS*, 238, 729
- George, I. M., & Fabian, A. C., 1991, *MNRAS*, 249, 352
- Hannikainen, D., et al. 2000, in "Proceedings of the Third Microquasar Workshop: Granada Workshop on galactic relativistic jet sources", Eds: A. J. Castro-Tirado, J. Greiner and J. M. Paredes, *Astrophysics and Space Science*, in press
- Homan, J., Wijnands, R., & van der Klis, M., 1999, *IAU Circ.* 7121, 2
- Homan, J., et al., 2001, *ApJS*, 132, 377-402
- Kalemci, E., Tomsick, J. A., Rothschild, R. E., Pottschmidt, K., & Kaaret, P., 2001, *ApJ*, 563, 239
- Knight, F. K., 1982, *ApJ*, 260, 538
- Marshall, H. L., et al., 2001, *AJ*, 122, 21
- Masetti, N., and Soria, R., 2000, *IAU Circ.*, 7399
- Massaro, E., Susumano, G., Litterio, M., & Mineo, T., 2000, *A & A*, 361, 695
- Merloni, A., Fabian, A. C., & Ross, R. R., 2000, *MNRAS*, 313, 193
- Miller, J. M., et al., 2001a, *ApJ* 563, 928
- Miller, J. M., et al., 2001b, *ApJ* 546, 1055
- Miller, J. M., et al., 2002a, *ApJ*, 570, L69
- Miller, J. M., et al., 2002, *ATEL* 81
- Mitusda, K., et al., 1984, *PASJ*, 36, 741
- Orosz, J. A., Bailyn, C., & Jain, R., 1998, *IAU Circ.*, 7009
- Orosz, J. A., et al., 2002, *ApJ*, 568, 845
- Remillard, R. A., et al., 1999a, *ApJ*, 517, L127
- Ross, R. R., Fabian, A. C., & Young, A. J., 1999, *MNRAS*, 306, 461
- Shahbaz, T., van der Hooft, F., Casares, J., Charles, P. A., & van Paradijs, J., 1999, *MNRAS*, 306, 89
- Shimura, T., & Takahara, F., 1995, *ApJ*, 445, 780
- Shrader, C., & Titarchuk, L., 1999, *ApJ*, 521, L21

- Smith, D. A., 1998, IAU Circ., 7008
- Smith, D. A., Levine, A. M., Remillard, R. Fox, D., & Shaefer, R., 2000, IAU Circ., 7399
- Sobczak, G. J, et al. 1999, ApJ, 520, 776
- Sobczak, G. J., et al. 2000, ApJ, 544, 993
- Strohmayer, T., E., 2001, ApJ, 552, L49
- Tanaka, Y., and Lewin, W. H. G., 1995, in "X-Ray Binaries," ed. W. H. G. Lewin, J. van Paradijs, & E. P. J. van den Heuvel (Cambridge, UK: Cambridge University Press)
- Titarchuk, L, 1994, ApJ, 434, 314
- Tomsick, J. A., Corbel, S., and Kaaret, P., 2001a, ApJ 563, 229
- Tomsick, J. A., Smith, E., Swank, J., Wijnands, R., and Homan, J., 2001b, IAU Circ., 7575

Chapter 5

XMM-Newton Grating

Spectroscopy of GRS 1758–258 in a Peculiar Off/Soft State

This chapter is based on the original paper:

“*XMM-Newton* Spectroscopy of the Galactic Microquasar GRS 1758–258 in the Peculiar Off/Soft State” Miller, J., M., Wijnands, R., Rodriguez-Pascual, P. M., Ferrando, P., Gaensler, B. M., Goldwurm, A., Lewin, W. H. G., and Pooley, D., 2002, *The Astrophysical Journal*, Vol. 566, p. 358,

with the permission of the publisher, *The Astrophysical Journal*.

5.1 Abstract

We report on an *XMM-Newton* Reflection Grating Spectrometer observation of the black hole candidate and Galactic microquasar GRS 1758–258. The source entered a peculiar “off/soft” state in late February, 2001, in which the spectrum softened while the X-ray flux – and the inferred mass accretion rate – steadily decreased. We find no clear evidence for emission or absorption lines in the dispersed spectra, indicating that most of the observed soft flux is likely from an accretion disk and not from

a cool plasma. The accretion disk strongly dominates the spectrum in this lower-luminosity state, and is only mildly recessed from the marginally stable orbit. These findings may be difficult to explain in terms of advection-dominated accretion flow, or “ADAF” models. We discuss these results within the context of ADAF models, simultaneous two-flow models, and observed correlations between hard X-ray flux and jet production.

5.2 Introduction

The source GRS 1758–258 was discovered with the *GRANAT*/SIGMA hard-X-ray/soft- γ -ray telescope (Sunyaev et al. 1991). It is often referred to as a “twin” source with 1E 1740.7–2942. Both are in the vicinity of the Galactic Center region, are strong emitters at hard-X-ray/soft- γ -ray energies, and display relativistic jets in the radio band (Mirabel et al. 1992; Rodriguez, Mirabel, & Marti 1992; Mirabel 1994). The hard spectrum of GRS 1758–258 extends to 300 keV and is similar to that of Cygnus X-1, and on that basis it is considered a black hole candidate (for a review of BHCs, see Tanaka & Lewin 1995).

The soft X-ray component in this source is usually very weak when the hard X-ray flux is at a typical strength. The soft component was too weak to be positively detected with *ASCA* (Mereghetti et al. 1997). However, a soft component below 2 keV, modeled with a power-law ($\Gamma_{\text{PL}} \sim 3$) was observed with *ROSAT* in 1993 when the hard power-law flux was less intense (Mereghetti et al. 1994). Similarly, the soft X-ray component was detected with *XMM-Newton* during a short, softer episode in September, 2000 (Goldwurm et al. 2001). In this observation, the soft component could be fit with a simple blackbody spectrum ($kT = 0.32$ keV).

In late February of 2001, observations with *RXTE* revealed a sharp drop in the hard (>10 keV) flux from GRS 1758–258, with no corresponding drop in the soft flux (Smith et al. 2001a,b,c). Smith et al. (2001c; hereafter, SHMS) report a steady decline in the 3–25 keV flux for 50 days following 27 February 2001. The soft component is clearly detected with the *RXTE*/PCA, and can be fit by both simple blackbody

and multicolor disk (MCD; Mitsuda et al. 1984) blackbody models. This state is qualitatively similar to the “off” state observed by *GRANAT*/SIGMA between fall 1991 and spring 1992 (Gilfanov et al. 1993), during which the hard X-ray flux of GRS 1758–258 decayed beneath detection limits. We therefore refer to the present X-ray spectral state as the “off/soft” state.

We requested a *XMM-Newton* target of opportunity (TOO) observation of GRS 1758–258 for three principal reasons: to better understand the nature of the soft component, to understand the implications of the off/soft state for current accretion flow models, and to place the off/soft state within the context of emerging connections between spectral flux components and jets in BHCs (Fender 2001). Herein we report the results obtained with the *XMM-Newton* Reflection Grating Spectrometer (RGS).

5.3 Observations and Data Analysis

Following our TOO request, GRS 1758–258 was observed for ~ 22 ksec starting at UT 09:48:12 on 22 March, 2001. RGS1 and RGS2 were operated in “spectral+Q” mode. The EPIC-MOS cameras were operated in “partial window, 100×100 ” mode, and the EPIC-PN camera in “large partial window, 200×384 ” mode. For the OM, “grism 1,” optimized for the ultraviolet band, was used.

Accurate analysis of bright sources like GRS 1758–258 requires a careful treatment of pile-up when dealing with the EPIC data. This in turn requires a good knowledge of the mirror response; the EPIC calibration team is developing a description of the in-flight calibration. The results presented in this work are therefore restricted to analysis of the RGS data, and results from the EPIC data analysis will be presented in future work. At the time of writing, the only previous X-ray binary observations reported on with *XMM-Newton* are EXO 0748–676 (Bonnet-Bidaud et al. 2001; Cottam et al. 2001) and GRS 1758–258 (observation in September 2000, Goldwurm et al. 2001). Instrumental performance and systematic effects will become more clear as more sources with a strong soft continuum flux are observed.

We have used the spectral data and background files produced by the standard

pipeline processing system at the *XMM-Newton* Survey Science Center (SSC) using Science Analysis Software (XMM-SAS) version 5.0. We estimate that fewer than 1% of the counts in the RGS spectra are from the nearby source GX 5–1.

To obtain improved statistical constraints on fitted models and to ensure the accuracy of Poisson statistics, we rebinned the background-subtracted first-order spectra from RGS1 and RGS2 by requiring a minimum of 20 counts per bin. After rebinning, between 0.35–0.60 keV the flux bin errors include zero. The flux bins steadily increase and the errors are inconsistent with zero above 0.60 keV. We therefore adopt 0.60 keV as the lower limit of our fitting range. Similarly, above 2.3 keV the flux bins have large errors and are consistent with zero, so we adopt 2.3 keV as the upper limit to our fitting range (the full energy range of the RGS is 0.35–2.50 keV).

Using XSPEC version 11.0 (Arnaud & Dorman, 2000), the RGS1 and RGS2 spectra are fitted simultaneously to account for any cross-calibration uncertainties. An overall normalization constant is allowed to float between the data obtained from each. Values obtained for this constant are approximately 0.95 for all fits.

5.4 Results

The results of our joint fits to the RGS spectra are detailed fully in Table 5.1. In each of the six models, the continuum components are multiplied by a model for photoelectric absorption (“wabs,” in XSPEC). Model 6 is a single-component model consisting of a simple power-law. Although statistically only marginally worse than models dominated by a thermal component ($\chi^2/\nu = 1.778, \nu = 1251$), the power-law index is abnormally high ($\Gamma_{\text{PL}} = 5.2 \pm 0.2$), and inconsistent with values obtained for other BHCs regardless of spectral state (for a review, see Tanaka & Lewin 1995). We therefore conclude that models dominated by a thermal component are required to fit the data from GRS 1758–258 in the off/soft state, and concentrate on these.

In models which include thermal and power-law components, the power-law index could not be constrained. In order to be consistent with models widely fit to BHCs, and especially those recently fit to GRS 1758–258, we fix the power-law indices in

models 1–5 to those measured by SHMS via fits to *RXTE*/PCA data obtained on 12–13 March, 2001 in the 3–25 keV band using the same models. The fit results for models 1–5 indicate that the power-law component is not required in this energy range as a zero normalization is preferred. We quote 90% upper-limits for the 0.6–2.3 keV contribution from a power-law component in Table 5.1. In all cases, the power-law contributes less than 2% of the total flux in this band. This is consistent with *Chandra* measurements in the 1–10 keV band during the off/soft state (Heindl and Smith 2001).

Models 1 and 3 consist of MCD and simple blackbody components, respectively, in combination with a power-law component ($\chi^2/\nu = 1.621$, $\chi^2/\nu = 1.587$, respectively, $\nu = 1252$). The data/model ratios obtained for models 1 and 3 are nearly identical (see Figure 5-1), and neither indicates the presence of any significant line emission (indeed, line emission is not indicated regardless of continuum model). In part, the poor χ^2 statistics obtained for these models (indeed, for all models) may be due to the approximately 5% normalization discrepancy between RGS1 and RGS2. A second contributing factor may be the relatively smaller RGS effective area above ~ 2 keV; we included this region after rebinning to better-constrain any power-law flux. When the characteristics of the RGS are more clearly known for strong continuum sources like GRS 1758–258, it may be possible to improve on the fits.

Models 2 and 4 are duplicates of models 1 and 3 respectively, except in models 2 and 4 we have fixed the neutral hydrogen column density (N_H) to 1.5×10^{22} atoms/cm² as per fits to *ASCA* data of GRS 1758–258 reported by Mereghetti et al. (1997). Model 5 is like 3 and 4 in that simple blackbody and power-law components are used to model the continuum, but in this model N_H is fixed to 1.74×10^{22} atoms/cm², as measured via fits to *XMM-Newton*/EPIC-MOS data on GRS 1758–258 obtained in September, 2000 (Goldwurm et al. 2001). There are no reasons to doubt the value of N_H we measure due to instrumental effects (e. g., CCD pile-up, as the RGS is a dispersive spectrometer). Rather, these models are fit to allow for comparisons to the results of SHMS and Goldwurm et al. (2001) as directly as possible.

Via the MCD model, SHMS obtain a color temperature of $kT = 0.464 \pm 0.007$ keV.

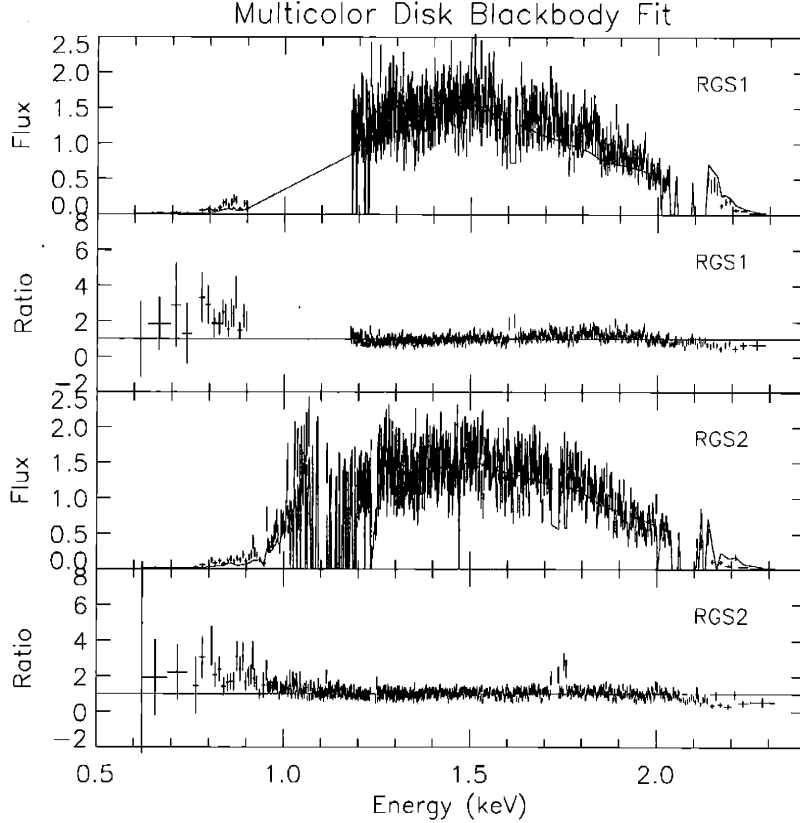


Figure 5-1 Results of fitting to RGS1 and RGS2 jointly with a model consisting of multicolor disk blackbody and power-law components. The flux (in units of normalized counts/cm²/s) and data/model ratio are shown; at top: RGS1, at bottom: RGS2. Fits with a model consisting of simple blackbody and power-law components, and of only a power-law component (see Table 5.1) yield similar results in terms of the fit and data/model ratio. The large gap seen in RGS1 (0.9–1.2 keV) is due to a failed CCD in that region of the dispersed spectrum. Points where the model goes through flux bins consistent with zero (in RGS1: near 1.2 keV, and 2.0–2.1 keV; in RGS2: between 1.0–1.3 keV, and 2.0–2.1 keV) are an artifact of our rebinning (requirement of 20 counts per channel) in regions of low or rapidly changing effective area.

Via model 1 (N_H free), we find a color temperature of $kT = 0.34 \pm 0.01$ keV. In both measurements, the errors are 90% confidence errors; these color temperatures are significantly different. Via model 2 (N_H fixed at SHMS value), we find a color temperature of $kT = 0.60 \pm 0.01$ keV. Again, this is significantly different from the value measured by SHMS. However, the fit with model 2 ($\chi^2/\nu = 2.227, \nu = 1251$) is statistically worse than that obtained via model 1 ($\chi^2/\nu = 1.621, \nu = 1252$).

SHMS report a simple blackbody temperature of $kT = 0.395 \pm 0.006$ keV. Fits with model 3 (N_H free) indicate $kT = 0.286 \pm 0.007$ keV, and via model 4 (N_H fixed at SHMS value) $kT = 0.378^{+0.005}_{-0.004}$ keV. The temperature measured via model 4 is only

slightly lower than that measured by SHMS, and only marginally inconsistent at 90% confidence. However, the fit obtained with model 3 is statistically preferred and the temperature is significantly lower.

The blackbody temperature obtained via fitting with model 5, wherein N_H is fixed to the value measured by Goldwurm et al. (2001), is $kT = 0.332^{+0.002}_{-0.001}$ keV. They measure $kT = 0.32 \pm 0.02$ keV – these temperatures are consistent at 90% confidence. Statistically, model 3 is a marginally better fit, and for this model the measured temperature is significantly lower.

We attempted to describe the spectrum in terms of a diffuse plasma by fitting with the “mekal” and “raymond” models within XSPEC. Fits which are statistically only marginally worse than those with models 1–6 are obtained, but only if the elemental abundances are allowed to assume values less than 0.2% of solar values. As this physical scenario is extremely unlikely, we do not further consider these models.

To test for the presence of narrow emission or absorption lines, we apply the continuum we measured via model 1 in fits to the rebinned data to the RGS1 and RGS2 spectra at full instrumental resolution. We selected model 1 instead of model 3 as we regard the MCD model to be more physical for BHCs than a simple blackbody model (the difference in the continuum shape from model three should be very small). In Figure 5-2, we plot the 90% confidence upper-limits on the strengths of emission or absorption features with widths less than or equivalent to the first-order RGS resolution. For visual clarity, we have rebinned the data in this plot by a factor of 10. It is clear from this plot that any narrow line features in the 0.6–2.3 keV range are very weak (equivalent width ~ 1 –5 eV for most of the bandpass) when GRS 1758–258 is in the off/soft state.

Finally, we examine the lightcurve obtained during this observation for the full RGS energy range (see Figure 5-3). Standard Shakura–Sunyaev (1973) accretion disks should vary on the viscous timescale through the disk (weeks). In sources wherein a power-law is observed (and a coronal volume therefore implied), significant short-timescale flux variations (seconds–hours) are observed (see Tanaka & Lewin 1995). Such rapid variations – both aperiodic and quasi-periodic – can be described

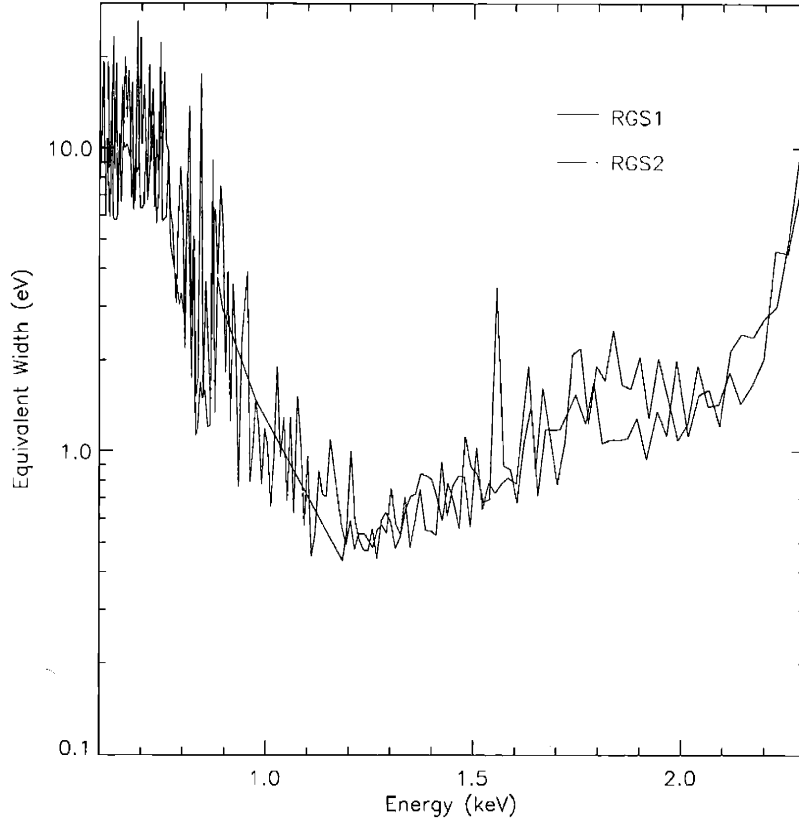


Figure 5-2 Upper limits (95% confidence) on the strength of narrow, single-bin emission or absorption features in the RGS spectrum of GRS 1758–258. RGS1 is shown in red, and RGS2 is shown in blue. The limits have been rebinned by a factor of 10 for visual clarity. These limits are based on our best fit to the continuum with the MCD multicolor disk blackbody model; results from a simple black body continuum model are very similar.

in terms of magnetic flaring between the disk and corona or within the corona itself (see, e.g., Di Matteo, Celotti, & Fabian 1999; Merloni, Di Matteo, & Fabian 2000). The lightcurve shown in Figure 5-3 is extremely steady, supporting an accretion disk interpretation for the spectrum we have observed.

5.5 Discussion

Although we have observed the soft X-ray component in the off/soft state of GRS 1758-258, no clear emission or absorption features have been observed in the joint spectra of RGS1 and RGS2 (see Figures 5-1 and 5-2). Observations of BHCs 1E 1740.7–2942 (Cui et al. 2001) and SS 433 (Marshall et al. 2001) with *Chandra* have

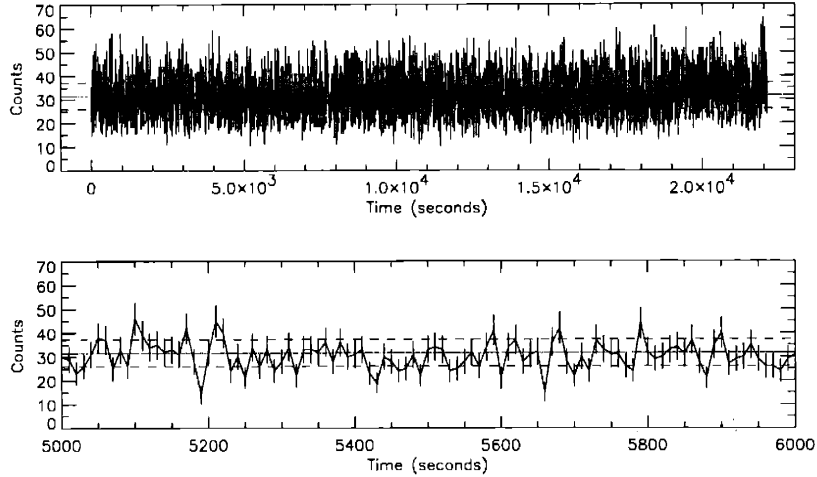


Figure 5-3 The combined RGS-1 and RGS-2 first-order lightcurve (time bins are 10 seconds, energy range: 0.3–2.5 keV). Above, the lightcurve for the full observation; below, a randomly selected segment. Plotted through the lightcurve is the mean count rate (solid red line), and 1σ deviations (individual error bars are 1σ). Standard Shakura-Sunyaev (1973) accretion disks should vary on a viscous timescale (weeks). This lightcurve is extremely steady, supporting our interpretation of the low-flux state of GRS 1758–258 as being dominated by an accretion disk.

found evidence for extended regions around the X-ray sources which are too large to be an accretion disk but too small to be a supernova remnant. A central goal of our observation was to examine the nature of such an extended region in GRS 1758–258, if one exists. Since optically-thin, cooling plasmas produce strong line features, it is unlikely that the soft component we have measured is due to such a region. The improbable abundances required by fits with models for diffuse plasmas support this interpretation.

The jets from GRS 1758–258 observed in the radio band might be another potential source for X-ray line emission. Tentative evidence for lines from a jet are found in the Chandra observation of 1E 1740.7–2942 noted above; lines are clearly detected in the spectra of SS 433. The absence of lines that might be attributed to a jet in GRS 1758–258 is consistent with a picture in which jets are extinguished in the soft state in BHCs (Fender 2001). Recently, it has also been proposed that jets might produce the power-law component observed in BHCs (Markoff, Falcke, & Fender 2001). The observed absence of lines consistent with a jet, coupled with the diminished strength of the power-law component in the off/soft state, may support

this model. Stronger conclusions must await the publication of radio data gathered during the off/soft state of GRS 1758–258.

The soft X-ray component we have measured is likely due primarily (but not necessarily entirely) to an accretion disk. This interpretation is bolstered by the lack of significant variability in the lightcurve obtained for this observation (see Figure 5-3). We measure a disk temperature which is broadly consistent with results obtained with the *RXTE*/PCA by SHMS on 12–13 March 2001, and with a short soft state only five months previous to our observation (Goldwurm et al. 2001). From Table 5.1, it is clear that the temperature of the soft component and the 0.6–2.3 keV flux are dependent upon the value of N_H which is used. Based on the results of SHMS, and our finding that a power-law component contributes less than 2% of the flux in the 0.6–2.3 keV range, it is possible that in the extended off/soft state the hard power-law flux merely turns-off and reveals the accretion disk.

The off/soft state is indicated by a steady decrease in the 3–25 keV flux from GRS 1758–258, and by a far softer spectrum than is observed when the source is in the more typical low/hard state (SHMS 2001). Such a decrease in flux is usually interpreted in terms of a decreasing \dot{m} . Advection-dominated accretion flow (ADAF) models adapted to BHCs (Esin, McClintock, & Narayan 1997; Esin et al. 1998) predict that a decrease in the mass accretion rate (\dot{m}) should be accompanied by spectral hardening. The spectral hardening may occur as the inner accretion disk is replaced by a hot, optically-thin region which may Comptonize seed photons and produce a power-law spectral component. In sharp contrast, the spectrum of GRS 1758–258 softens as the inferred \dot{m} decreases.

If the distance to a source and its inclination are known, the MCD model provides a measure of the temperature and inner radial extent of the accretion disk. In fact, the derived temperature and radius may be distorted by the Comptonization of disk photons by a coronal volume or a disk atmosphere. Shimura and Takahara (1995) have reported that a simple correction factor f_{col} can account for this effect; the effective disk temperature is given by $T_{eff} = T_{col}/f_{col}$, and the effective radius is given by $r_{eff} = f_{col}^2 r_{col}$. For BHCs, a typical value is $f_{col} = 1.7$ (see, e. g., Sobczak

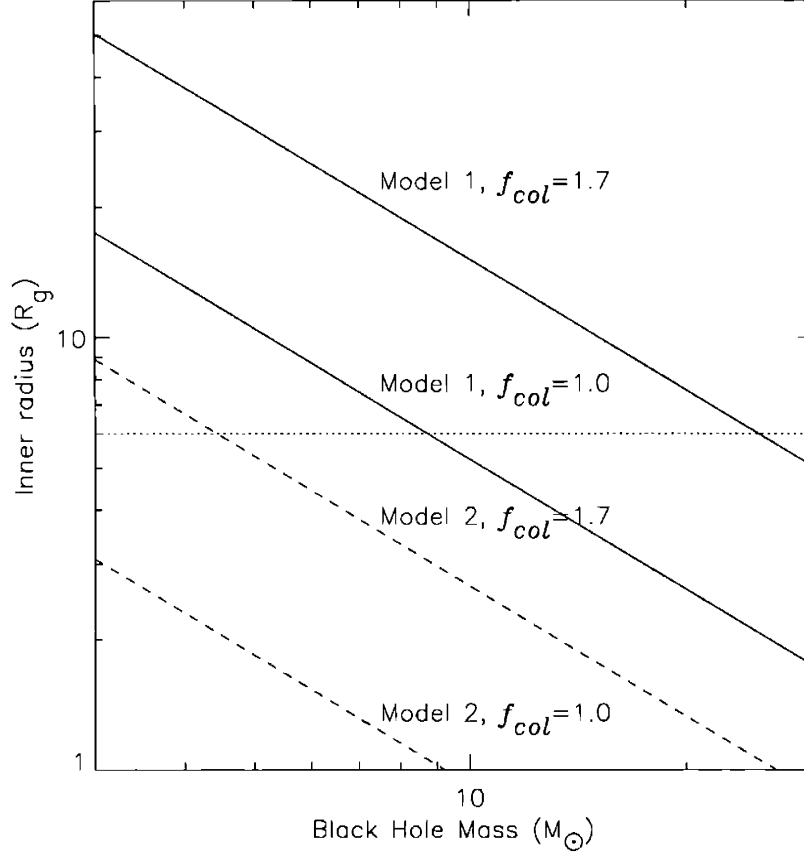


Figure 5-4 Inner accretion disk radii derived via the multicolor disk blackbody model, assuming an intermediate inclination ($\theta_{\text{incl}} = 45^\circ$) and a distance of 8.5 kpc. Fits with model 1 (N_H free) yield inner radii of 77 km and 220 km, for $f_{\text{col}} = 1.0$ and $f_{\text{col}} = 1.7$, respectively. Fits with model 2 (N_H fixed) yield inner radii of 14 km and 39 km, for $f_{\text{col}} = 1.0$ and $f_{\text{col}} = 1.7$, respectively. The marginally stable circular orbit around a Schwarzschild black hole is $6 R_g$; this radius is indicated with a dotted line.

et al. 1999).

In Figure 5-4, we present constraints on the inner radial extent of the accretion disk. The best-fit color temperature and radius measured with MCD models in Table 5.1 are used. We assume a distance of 8.5 kpc to GRS 1758–258 based on its central Galactic position and column density. The inclination of GRS 1758–258 has not yet been measured, however the detection of jets in the radio band makes it unlikely that the system is seen face-on. We therefore assume an intermediate value for the inclination angle ($\theta_{\text{incl}} = 45^\circ$). We plot constraints on the inner radii calculated using no color correction ($f_{\text{col}} = 1.0$) and the typical value for BHCs ($f_{\text{col}} = 1.7$).

Given that the hard flux is diminished greatly in the off/soft state of GRS 1758–258,

it is likely that the Comptonization of disk photons is not as strong an effect as in other BHCs and the color correction may not be required. If no color correction is applied, for reasonable values of the black hole mass in GRS 1758–258 the inner extent of the accretion disk is broadly consistent with the marginally stable circular orbit around a Schwarzschild black hole (see Figure 5-4). This finding may be inconsistent with ADAF models of other BHCs at relatively low implied values of \dot{m} (in some sources, however, X-ray flux and spectral states may be decoupled; see, e. g., Homan et al. 2001; Wijnands & Miller 2001). If the color correction is accurate, the inner disk extent is slightly recessed and consistent with ADAF models of Cygnus X-1 in the low/hard state ($r_{in} > 20 R_g$, Esin et al. 1998). However, the spectrum of Cygnus X-1 at lower implied values of \dot{m} is more consistent with an inner ADAF volume than the spectrum of GRS 1758–258. A simple ADAF interpretation might still be valid for this source if the soft component could be attributed to an extended cool volume, but our results indicate that this is very unlikely. A model in which the inner advection region is peculiarly radiatively-inefficient might describe the off/soft state of GRS 1758–258.

Smith, Heindl, and Swank (Smith et al. 2001d) have discussed the long-term spectral variability of BHCs 1E 1740.7–2942, GRS 1758–258, GX 339–4, Cygnus X-1, and Cygnus X-3 in terms of two independent accretion flows. As SHMS note, the off/soft state is adequately described by this model. The possible cooling of the accretion disk which we measure supports this picture. It is interesting to note that Chen, Gehrels, and Leventhal (1994) have proposed that 1E 1740.7–2942 and GRS 1758–258 may accrete both through an accretion disk and via Bondi-Hoyle accretion from the relatively high-density ISM in the Galactic center. Observationally, the two-flow and disk-plus-Bondi-Hoyle accretion models may be very similar.

Table 5.1 The Results of Fits to the RGS Spectra of GRS 1758–258

Multicolor Disk Blackbody Fits							
Model	N_H (10^{22} cm^{-2})	kT (keV)	N_{MCD}	PL index	N_{PL} (10^{-3})	$L_{0.6-2.3}$ (10^{36} erg/s)	χ^2/dof
1	$2.28^{+0.07}_{-0.02}$	$0.34^{+0.01}_{-0.01}$	5850^{+1900}_{-1100}	2.75	<4.5	8^{+2}_{-2}	2030/1252
2	1.50	$0.60^{+0.01}_{-0.01}$	180^{+10}_{-10}	2.75	<0.6	$2.6^{+0.2}_{-0.2}$	2786/1251
Blackbody Fits							
Model	N_H (10^{22} cm^{-2})	kT (keV)	N_{BB} (E-3)	PL index	N_{PL} (10^{-3})	$L_{0.6-2.3}$ (10^{36} erg/s)	χ^2/dof
3	$2.09^{+0.06}_{-0.06}$	$0.286^{+0.007}_{-0.007}$	$9.1^{+0.9}_{-0.8}$	2.89	<5.1	$5.0^{+0.6}_{-0.4}$	1987/1252
4	1.50	$0.378^{+0.005}_{-0.004}$	$4.30^{+0.05}_{-0.05}$	2.89	<0.6	$2.37^{+0.03}_{-0.06}$	2361/1251
5	1.74	$0.332^{+0.002}_{-0.001}$	$5.66^{+0.08}_{-0.08}$	2.89	<1.6	$3.18^{+0.07}_{-0.04}$	2096/1251
Power-law Fits							
Model	N_H (10^{22} cm^{-2})	—	—	PL index	N_{PL}	$L_{0.6-2.3}$ (10^{36} erg/s)	χ^2/dof
6	$2.9^{+0.1}_{-0.1}$	—	—	$5.2^{+0.2}_{-0.2}$	$2.2^{+0.4}_{-0.4}$	48^{+9}_{-8}	2222/1251

Note. — The results of fitting the background-subtracted, rebinned first-order RGS1 and RGS2 spectra jointly with standard models, in the 0.6–2.3 keV bandpass (90% confidence errors). The power-law indices in models 1–5 are fixed to the values obtained by Smith et al. (2001) using *RXTE* within the off/soft state as this component cannot be constrained in the limited energy range of the RGS. The power-law component is not required in fits 1–5 and the quoted normalizations and fluxes are upper-limits (90% conf.). The neutral hydrogen column density, N_H , is allowed to float in models 1, 3, and 6. In models 2 and 5, N_H is fixed to the values reported by Smith et al. (2001) to allow for more direct comparison to those results. Similarly, N_H is fixed to the value reported by Goldwurm et al. (2001) in fits to *XMM-Newton* EPIC-MOS data obtained in September, 2000. Model 6 is a simple power-law; the obtained χ^2 statistic is slightly worse than the models dominated by thermal components, but the measured index is very different than those reported in other BHCs (see, e. g., Tanaka & Lewin 1995). In fits 1–5, the power-law contribution to the 0.6–2.3 keV luminosity is <2% of the total; luminosities are calculated assuming a distance of 8.5 kpc. Luminosities quoted above are “unabsorbed” luminosities.

5.6 Bibliography

- Arnaud, K., & Dorman, B., 2000, XSPEC is available via the HEASARC on-line service, provided by NASA-GSFC
- Bonnet-Bidaud, J. M., Haberl, F., Ferrando, P., Bennie, P. J., & Kendziorra, E., 2001, *A & A*, 365L, 282B
- Chen, W., Gehrels, N., & Leventhal, M., 1994, *ApJ*, 426, 586
- Cottam, J., Kahn, S. M., Brinkman, A. C., den Herder, J. W., & Erd, C., 2001, *A & A*, 365L, 277C
- Cui, W., et al., 2001, *ApJ*, 548, 394C
- Di Matteo, T., Celotti, A., Fabian, A. C., 1999, *MNRAS*, 304 809
- Esin, A. A., McClintock, J. E., & Narayan, R., 1997, *ApJ*, 489, 865E
- Esin, A. A., Narayan, R., Cui, W., Grove, E. J., & Zhang, S., 1998, *ApJ*, 505, 854E
- Fender, R. P., 2001, *MNRAS*, 322, 31
- Gilfanov, M., et al., 1993, *ApJ*, 418, 844
- Goldwurm, A., Israel, D., Goldoni, P., Ferrando, P., Decourchelle, A., Mirabel, I. F., & Warwick, R. S., 2001, to appear in the Proc. of the Gamma-Ray Astrophysics 2001 Symposium, AIP, astro-ph/0106310
- Heindl, W. A., and Smith, D. M., 2001, to appear in "X-rays at Sharp Focus: Chandra Science Symposium ASP Conference Series", 2002, eds. S. Vrtilek, E. M. Schlegel, and L. Kuhi, astro-ph/0107469
- Homan, J., et al., 2001, *ApJS*, 132, 377
- Markoff, S., Falcke, H., Fender, R., 2001, *A & A*, 372L, 25M
- Marshall, H. L., et al., 2001, *ApJ* subm.
- Mereghetti, S., 1994, *ApJ*, 433, L21
- Mereghetti, S., Cremonesi, D. I., Haardt, F., Murakami, T., Belloni, T., & Goldwurm, A., 1997, *ApJ*, 476, 829
- Merloni, A., Di Matteo, T., and Fabian, A. C., 2000, *MNRAS*, 318L, 15
- Mirabel, I. F., 1994, *ApJS*, 92, 369
- Mirabel, I. F., Rodriguez, L. F., Cordier, B., Paul, J., & Lebrun, F., 1992, *Nature*, 258, 215
- Mitsuda, K., et al., 1984, *PASJ*, 36, 741
- Rodriguez, L. F., Mirabel, I. F., & Marti, J., 1992, *ApJ*, 401, L15
- Shakura, N. I., and Sunyaev, R. A., 1973, *A&A* 24, 337
- Shimura, T., and Takahara, F., 1995, *ApJ*, 445, 780S
- Smith, D. M., Markwardt, C. B., Heindl, W. A., & Swank, J. H., 2001a, *IAUC* 7595
- Smith, D. M., Heindl, W. A., Markwardt, C. B., & Swank, J. H., 2001b, *ATEL* 66
- Smith, D. M., Heindl, W. A., Markwardt, C. B., & Swank, J. H., 2001c, *ApJL*, in press, astro-ph/0103381
- Smith, D. M., Heindl, W. A., & Swank, J. H., 2001d, astro-ph/0103304
- Sobczak, G. J., McClintock, J. E., Remillard, R. A., Bailyn, C. D., & Orosz, J. A., 1999, *ApJ*, 520, 776
- Sunyaev, R., et al., 1991, *A & A*, 247, L29
- Tanaka, Y., and Lewin, W. H. G., 1995, in *X-ray binaries*, ed. W. H. G. Lewin, J. van Paradijs, & E. P. J. van den Heuvel (Cambridge: Cambridge Univ. Press), 126
- Wijnands, R., & Miller, J. M., 2001, *ApJL* subm., astro-ph/0105182

Chapter 6

Extremely Weak Reflection Features in the X-ray Spectrum of XTE J1118+480: Possible Evidence for X-ray-Emitting Jets?

This chapter is based on the original paper:

“Extremely Weak Reflection Features in the X-Ray Spectrum of XTE J1118+480: Possible Evidence for X-ray-Emitting Jets?” Miller, J. M., Ballantyne, D. R., Fabian, A. C., and Lewin, W. H. G., 2002, *The Monthly Notices of the Royal Astronomical Society*, in press,

with the permission of the publisher, Blackwell Science.

6.1 Abstract

We have simultaneously fit *Chandra* and *RXTE* spectra of the Galactic black hole XTE J1118+480 with three models for X-ray reflection. We explored a range of accretion disc ionizations ($\log(\xi)=1-4$; $\xi = L_X/nR^2$) and iron abundances (0.10–1.00). Our fits with the constant density ionized disc models of Ross & Fabian

indicate that ≤ 0.5 per cent (90 per cent confidence upper-limit) of the observed flux is reflected. Fits with the “pexrav” of model Magdziarz & Zdziarski indicate that the two-dimensional solid angle ($\Omega/2\pi$) subtended by the disc relative to a central source of incident hard X-rays is $0.01^{+0.06}_{-0.01}$. A combination of the high inclination ($i = 81$ degrees), Comptonization, and bulk velocities may each contribute to the low reflection fractions we have measured. The results are also consistent with extended jets being the source of the hard X-ray flux, as the disc would then represent a small solid angle as seen from the emission region.

6.2 Introduction

Reflection geometries are well-established in AGNs, and the same basic geometry – the irradiation of an accretion disc by hard X-rays – is very likely at work in Galactic black holes (see, e.g., Gierlinski et al. 1997; Zdziarski et al. 1998; Miller et al. 2001). The shape of the reflected component in a given spectrum depends on several factors, including the height and distribution of hard X-ray sources above the accretion disc, the temperature and ionization of the disc, and how close to the black hole the reflection occurs. Thus, the reflected component of a given spectrum may be used to constrain the accretion flow geometry.

XTE J1118+480 is particularly well-suited to reflection studies. In the bright X-ray states of most Galactic black holes (GBHs), the accretion disc is an X-ray object. This soft spectral component complicates fits with reflection models. In less luminous states, the accretion disc temperature is often below the soft X-ray band. Due to the extremely high latitude of XTE J1118+480, the disc temperature could be measured via UV spectroscopy. At $kT = 24$ eV (McClintock et al. 2001a), the inner disc temperature in XTE J1118+480 is similar to, or lower than, the inner disc temperatures measured in many AGN. In any reflection analysis, the inclination of the system and the mass of the black hole are important parameters, and both have been measured in XTE J1118+480 ($i = 81 \pm 2$ degrees, Wagner et al. 2001; $M_{BH} > 6.0 M_{\odot}$, McClintock et al. 2001b), allowing us to more tightly constrain

other model parameters.

Two separate new models have been proposed to describe XTE J1118+480, which should produce different reflection signatures. Markoff, Falcke, and Fender (2001) have described a model in which synchrotron emission from the jet in this system (Fender et al. 2001) can account for the observed radio and X-ray spectra. In this model, a significant fraction of the power-law X-ray flux (perhaps all such flux) may be due to the jet. In such a geometry, one would expect very little of the flux to reflect from the accretion disc, and into the line of sight of the observer. Noting the similarity of optical and X-ray variability in this system, Merloni, Di Matteo, and Fabian (2000) have described a model wherein magnetic loops from the corona may generate hard X-rays and illuminate the accretion disc, creating the observed X-ray and optical QPOs. Although the inclination of XTE J1118+480 is high, if this process is at work, a fraction of the incident hard X-rays from the magnetic loops might scatter into the observing line of sight.

McClintock et al. (2001a) and Esin et al. (2001) describe the accretion flow geometry in terms of an advection-dominated accretion flow (ADAF). In this picture, the central accretion region is a hot, quasi-spherical, radiatively-inefficient volume, and the inner accretion disc edge is truncated at a radius far from the black hole. A central ADAF may be expected to diminish the strength of any reflection features (e.g. Gierlinski et al. 1997). In contrast, Frontera et al. (2001) have described the accretion geometry in terms of a hot accretion disc. This work considers reflection explicitly and finds that the angle ($\Omega/2\pi$) subtended by the disc ranges between 0.11–0.18 for a variety of models.

For the purpose of constraining the accretion flow geometry in XTE J1118+480, we have fit a number of reflection models, covering a large parameter space. *Chandra* and *RXTE* spectra were fit simultaneously, covering the 0.4–100 keV band. In the following sections, we detail our analysis and results. We also comment on recent models for XTE J1118+480.

Table 6.1 Observations of XTE J1118+480

Observatory	Instrument	Bandpass	Fitting Range	Date (UT)	Time (ksec)
<i>Chandra</i>	LETG/ACIS-S	0.24–7 keV	0.4–5 keV	18 Apr 18:16	27
<i>RXTE</i>	PCA	2–60 keV	2.8–25 keV	13 Apr – 15 May	46
<i>RXTE</i>	HEXTE	15–250	20–100 keV	13 Apr – 15 May	18

Note. — We fit the above data from the April–May 2000 outburst of XTE J1118+480. We summed 18 observations with *RXTE*, using all available proportional counter units (PCUs) in each observation (generally, PCUs 0, 2, and 3). The power-law slopes from the individual *RXTE* observations are consistent at the 3σ level of confidence (M. P. Munro, priv. comm.). Data from both HEXTE clusters is used.

6.3 Observation and Data Reduction

We analyzed the *Chandra* LETG/ACIS-S spectrum reported on by McClintock et al. (2001a), reduced via the methods detailed in that work. *Chandra* observed XTE J1118+480 on 18 April 2000, between 18:16–02:16 (UT), for an integrated exposure of 27.2 ksec. We consider the 0.4–5.0 keV range with 5 per cent systematic errors. Below 0.4 keV and above 5.0 keV, the data are more noisy and may require larger systematic errors (see the discussion in McClintock et al. 2001a), so we have restricted our fits to the 0.4–5.0 keV range.

We have summed 18 observations made with *RXTE* between 13 April and 15 May, 2000, for a total of 46 ksec of PCA data and 18 ksec of HEXTE data. This summation is not likely to distort any spectral features due to the extremely steady nature of XTE J1118+480: fits to individual spectra indicate that the power-law index is constant at the 3σ level of confidence across this time range (M. P. Munro, priv. comm.).

The PCA data was reduced using FTOOLS version 5. We used all available proportional counter units (PCUs; generally, PCUs 0, 2, and 3) in each observation, and selected only the top layers of the available PCUs. Response matrices were made using version 2.43 of “pcarsp.” Background spectra were made using the 2000 January 31 “blank-sky” model for gain epoch 4, and version 2.1e of “pcabackest.” Background spectra were subtracted using “mathpha.” We consider the 2.8–25 keV

energy range, as residuals below 2.8 keV are relatively large and the PCA spectrum becomes background-dominated above 25 keV. Spectra from individual observations are summed using “mathpha.” Uncertainties in the PCA response may be as large as 1 per cent (Jahoda 2000), so we have added 1 per cent systematic errors to the statistical errors before fitting the summed PCA spectrum.

The HEXTE data were also reduced using FTOOLS version 5. The standard response matrices were used. The background was estimated using “hxtback,” and source spectra were summed using “mathpha.” No systematic errors were added to this data. Although data in the 15–20 keV range are likely free of any systematic effects, we excluded this range to avoid any possible response problems at the edge of the detector energy range. Even though HEXTE is sensitive up to 250 keV, we fit only up to 100 keV. We are interested in comparing reflection models as consistently as possible, and the version of the “constant density ionized disc” reflection model (Ross & Fabian, 1993; Ross, Fabian, & Young 1999) which calculates a reflection fraction is only valid up to 100 keV. The high energy signature of reflection – the Compton-backscattering excess – peaks near ~ 30 keV (George & Fabian 1991), so an upper limit of 100 keV is high enough to allow for robust analysis.

6.4 Analysis and Results

Chandra LETG/ACIS-S, *RXTE* PCA, and *RXTE* HEXTE-A and HEXTE-B spectra are fit simultaneously, with an overall normalising constant allowed to float between each. The fitting range discussed above (0.4–100 keV) has a total of 1248 energy bins. For all fits, we fixed the neutral hydrogen column density to the value selected by McClintock et al. (2001a): $N_H = 1.3 \times 10^{20} \text{ cm}^{-2}$. We note a “notch” in the LETG/ACIS-S spectrum near 2 keV. As this feature was not seen in a *BeppoSAX* observation of XTE J1118+480 (Frontera et al. 2001), we consider this feature to be an instrumental artifact. This assessment is bolstered by the fact that a similar “notch” is seen in other *Chandra* observations of bright continuum sources (e.g., Patel et al. 2001, Miller et al. 2002, Juett et al. 2002). We modeled this feature with an

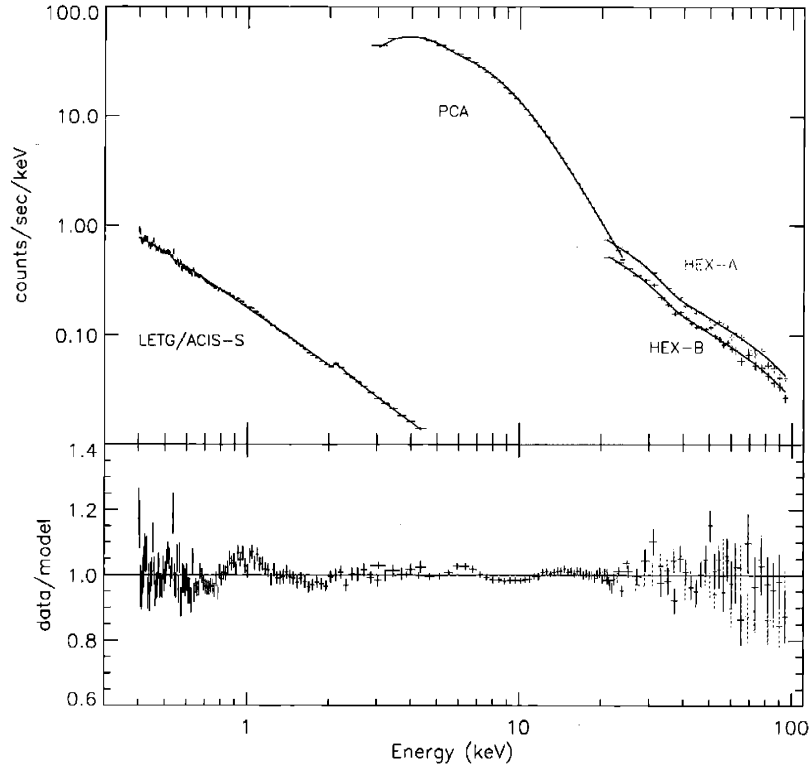


Figure 6-1 Spectra from XTE J1118+480 fit simultaneously with a simple power-law model, and the data/model ratio for that fit. Due to the small reflection fraction, fits with the reflection models are indistinguishable from that shown here. Pictured above: in black, the *Chandra* LETG/ACIS-S spectrum (rebinned by a factor of 10 for clarity); in red, the *RXTE* PCA spectrum; and in green and blue (respectively), the *RXTE* HEXTE-A and HEXTE-B spectra.

inverse edge at 2 keV ($\tau = -0.15$). With this addition, the LETG/ACIS-S spectral index becomes consistent with that of the other instruments.

Some of the fits we describe below include the effects of relativistic blurring, which is expected for regimes close to a black hole. In XSPEC, it is possible to convolve a fitting model with a Gaussian or Lorentzian profile. Instead of convolving with these profiles, we convolve with a profile appropriate for a general relativistic regime (the “diskline” model within XSPEC). Where we have blurred the spectrum, we do so for $6 R_g \leq R_{in} \leq 10^5 R_g$, $R_g = GM_{BH}/c^2$.

The “pexrav” and “pexriv” models do not include an Fe K_α line, and one must be added explicitly. The possibility of an iron line is discussed in McClintock et al. (2001a). Although we do not consider the 5–7 keV range in the *Chandra* spectrum due to larger overall effective area calibration uncertainties in that band, it is fine for

examining the possibility of narrow emission and/or absorption features. We therefore adopt the same Fe K_{α} upper-limit as McClintock et al. (2001a), and constrain the equivalent width to be less than 24 eV. We fix the width at zero as any 1–2 bin features in the LETG are unresolved at the resolution of the PCA. The line center is fixed at 6.4 keV. We also consider the possibility of an Fe under-abundance intrinsic to XTE J1118+480 in fitting “pexrav” and “pexriv” to explore the possible effects on the reflection fraction. It should be noted, however, that our fits to the *Chandra*/LETG data in the region of the Fe L_{III} edge do not indicate an under-abundance relative to solar values.

Fit parameters for each model which are not discussed below, are detailed in Table 6.2. Unless otherwise noted, all errors quoted in this paper are the difference between the best-fit value of a given parameter, and its value at the 90 per cent confidence limits.

6.4.1 Fits with a simple power-law

We first consider a simple power-law model for the spectrum (see Figure 6-1). This simple model is an excellent fit, yielding a very good reduced fit statistic ($\chi^2/\nu = 0.982, \nu = 1243$). We obtain a power-law index of $\Gamma = 1.777 \pm 0.004$, which is consistent with the values reported by McClintock et al. (2001) for the *Chandra* LETG/ACIS-S and combined *RXTE* spectra ($\Gamma = 1.77 \pm 0.4$, and $\Gamma = 1.782 \pm 0.005$, respectively). Frontera et al. (2001) measure a slightly harder power-law index with *BeppoSAX* ($\Gamma = 1.722^{+0.003}_{-0.005}$). Whereas we fit an energy range (0.4–100 keV) which does not require a blackbody component or a cut-off in the power-law slope at high energy, the *BeppoSAX* results cover the 0.1–200 keV range, and include a blackbody component and a cut-off. Even without these considerations, it is striking how well these spectral characterisations agree.

6.4.2 Fits with “Pexrav” and “Pexriv”

We next made fits with “pexrav” (Magdziarz & Zdziarski 1995). This model describes the reflection of hard, power-law X-rays from a cool, neutral accretion disc. The parameters of this model include: the index of the incident power-law flux, the energy cut-off of the power-law, the reflection fraction ($0 \rightarrow 2\pi$, normalised to 1, corresponding to an isotropic source above the disc), the source redshift, the abundance of elements heavier than He, the abundance of Fe, the cosine of the inclination angle, and component normalisation (photon flux at 1 keV). In our fits, the power-law index and cut-off, the reflection fraction, and flux were allowed to float. We fixed the redshift at zero, the lower abundances at solar, the Fe abundance at 0.10 and 1.00 relative to solar (see below), and the cosine of the inclination angle to 0.156 ($i = 81$ degrees; Wagner et al. 2001, McClintock et al. 2001b). We considered this model with and without incorporating the effects of relativistic blurring on the overall spectrum.

With the iron abundance set to 1.00 relative to solar abundances, fits with pexrav return a best-fit reflection fraction of $f = 0.01^{+0.06}_{-0.01}$. Relativistic blurring does not affect this result. However, as XTE J1118+480 is a halo object, it is possible that it has a significant Fe under-abundance. We therefore also made fits with the Fe abundance fixed at 0.10 relative to solar abundance. Again, the best-fit values for f , with blurring and without, were consistent with zero. The upper limits with this lower abundance are $f \leq 0.04$ for both blurred and unblurred models.

We conclude that the upper-limits we have obtained with this model may be imprecise and dominated by the fact that the best-fit reflection fractions are consistent with zero. The most reliable upper-limit on the reflection fraction is likely the largest, $f \leq 0.04$. With these low reflection fractions, “pexrav” is a good fit to the data (e.g., without blurring and with Fe at solar abundance, $\chi^2/\nu = 0.960, \nu = 1241$).

“Pexriv” (Magdziarz & Zdziarski 1995) is a cousin to “pexrav,” meant to cover regimes in which the accretion disc is ionized. An ionized accretion disc might be expected when the inner edge extends close to the black hole, and is therefore more strongly irradiated by incident hard X-rays. For this reason, we only consider this

model with the effect of relativistic blurring. The parameters of this model in addition to those for “pexrav” include the disc temperature, and the disc ionization parameter ξ . We fix the disc temperature to 24 eV, as per McClintock et al. (2001a), and examine the extreme ionization cases: $\xi = 0.0, 5000$ (5000 is the upper-limit for this model), and Fe abundances of 0.10 and 1.00 relative to solar.

For solar iron abundances and $\xi = 0$, $f = 0.01^{+0.06}_{-0.01}$ – this is exactly what we obtain with “pexrav” for the same values. For all other combinations of Fe abundance and ξ , the upper-limit on the reflection fraction is $f \leq 0.001$. In all cases, “pexriv” was an acceptable fit (even for $\xi = 5000$); for the $\xi = 0$ and Fe abundance at full solar value, $\chi^2/\nu = 0.966, \nu = 1240$.

We note that a very small error may be introduced by fitting “pexrav” and “pexriv” with a gaussian iron line model for which the maximum equivalent width is constrained to be less than 24 eV. Based on George & Fabian (1991), in the limit where all of the observed spectrum is reflected, the Fe K_α line equivalent width expected at an inclination of 81 degrees is approximately 40 eV. However, as we measure only a very small fractional reflection with “pexrav” and “pexriv,” we regard any error introduced by constraining the Fe K_α line $EW \leq 24$ eV to be negligible.

6.4.3 Fits with the “Constant Density Ionized Disc Model”

This model is designed to handle a large range of disc ionizations ($\log(\xi) = 1 \rightarrow 6$), assuming a constant density accretion disc and a power-law irradiating spectrum. The parameters for this model include the incident power-law flux, the disc ionization, the source redshift, the reflection fraction, and the component normalisation (related to photon flux at the detector, but *not* diluted by $1/d^2$, and therefore on the order of 10^{-25} ph/cm²/s). In our fits, the redshift was fixed at zero, and all other parameters were allowed to float simultaneously. We considered this model with the effects of relativistic blurring.

Extremely tight constraints are obtained with this model. A very low ionization is indicated: $\log(\xi) = 1.056 \pm 0.002$. As with the other models, the best-fit reflection fraction is zero; an upper limit of $R \leq 0.002$ is obtained. Here, R is the fraction of

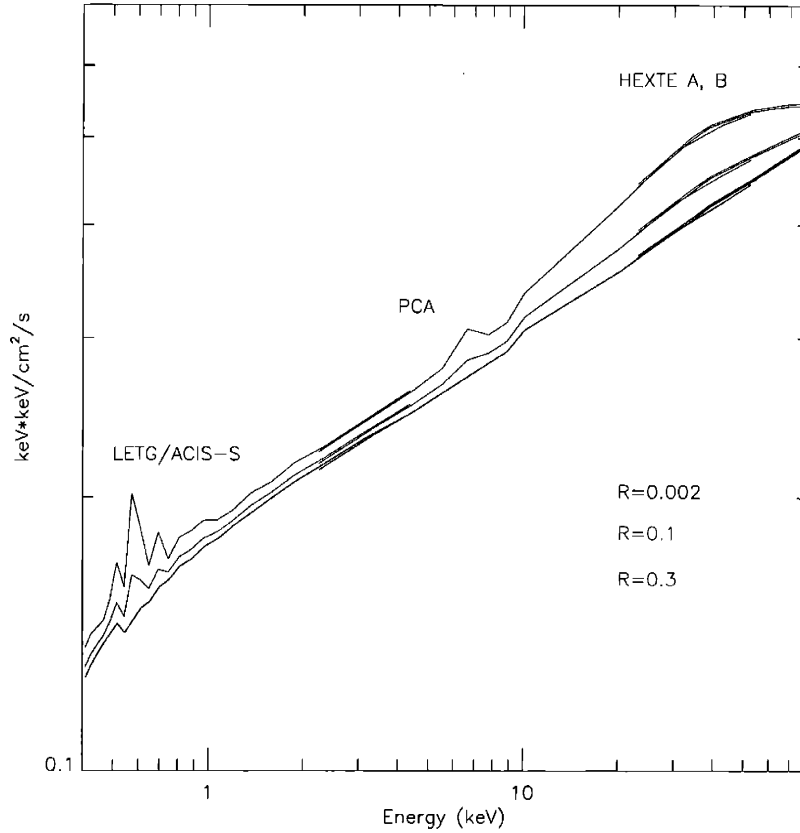


Figure 6-2 Different reflection fractions produce different curvatures (R is the fraction of the observed flux that was reflected). In fits with the constant-density ionized disc model, a reflection fraction of $R = 0$ is preferred. Here, we have plotted the 90 per cent confidence upper-limit $R = 0.002$. Plotted in red and blue (assuming the same unreflected normalization): the model for $R = 0.1$ and $R = 0.3$, respectively. Models are rebinned by a factor of 50 for visual clarity. Note that within the text, we discuss why an upper limit of $R \leq 0.005$ may be more appropriate.

the total flux that is reflected (not an angle, like f). The fit achieved with this model is also good ($\chi^2/\nu = 1.034$, $\nu = 1241$). We tested the robustness of the low values for the ionization parameter and reflection fraction by fixing these parameters at higher values; this resulted in large changes in the fit statistic ($\Delta\chi^2/\nu \simeq 1 - 3$), indicating that a low ionization and reflection fraction are strongly preferred with this model. In Figure 6-2, we plot the constant-density ionized disk model with $R = 0.002, 0.1$, and 0.3 to illustrate the extremely weak nature of the reflection component we have measured in XTE J1118+480.

The R value measured by this model is an angle-averaged result. By inspection of the reflection components calculated in George & Fabian (1991), it is clear that at

Table 6.2 The Results of Fits to the XTE J1118+480 Spectra with Reflection Models

Model	Blurring ^a	Fe ^b (fixed)	Γ ^c	E_c ^d (keV)	ξ ^f	f_{refl} ^g	Norm. ^h	ν ^j	χ^2/ν
power-law	No	1.0	1.777(4)	—	—	—	0.1823(7)	1243	0.982
pexrav	No	1.0	1.767(3)	900^{+500}_{-300}	—	$0.01^{+0.06}_{-0.01}$	0.182(1)	1241	0.960
pexrav	Yes	1.0	1.767(5)	900^{+500}_{-300}	—	$0.01^{+0.06}_{-0.01}$	0.178(1)	1241	0.965
pexrav	No	0.1	1.764(4)	1000^{+300}_{-300}	—	<0.04	0.182(7)	1241	0.961
pexrav	Yes	0.1	1.767(4)	900^{+500}_{-300}	—	<0.04	0.178(1)	1241	0.966
pexriv	Yes	1.0	1.767(4)	900^{+500}_{-300}	0 [†]	$0.01^{+0.06}_{-0.01}$	0.178(3)	1240	0.966
pexriv	Yes	1.0	1.768(4)	1100^{+600}_{-300}	5000 [†]	<0.001	0.180(3)	1240	0.987
pexriv	Yes	0.1	1.767(5)	900^{+600}_{-300}	0 [†]	<0.001	0.178(3)	1240	0.964
pexriv	Yes	0.1	1.767(5)	900^{+600}_{-300}	5000 [†]	<0.001	0.178(3)	1240	0.964
CDID	Yes	1.0	1.776(2)	—	11.3(1)	<0.002	$3.33(1) \times 10^{-24}$	1241	1.035

Note. — All errors are 90 per cent confidence. ^a Blurring is a relativistic convolution. ^b The iron abundance relative to solar. ^c The irradiating power-law index. ^d The high energy cut-off of the irradiating flux. ^f The ionization parameter, $\xi = L_X/nR^2$. ^g The reflection fraction. ^h The component normalization. ^j The degrees of freedom when fitting the given model as shown here. There were 1248 energy bins in total for every fit. [†] These values were fixed, as “pexriv” was not able to constrain the ionization. Our favored model is the constant density ionized disc model (CDID), which was able to simultaneously fit the reflection fraction and ionization.

81 degrees the strength of the reflected component is actually 2-3 times higher than we measure. Based on this comparison, the most appropriate upper-limit is slightly higher: $R \leq 0.005$.

6.5 Discussion

Each of the fits to XTE J1118+480 with “pexrav” or “pexriv” wherein the strength of the reflection component is measured prefer $f = 0.01^{+0.06}_{-0.01}$ – consistent with zero. These measurements are an order of magnitude lower than those found by Frontera et al. (2001) in fits to *BeppoSAX* spectra. Fitting these models on a range extending to 200 keV for a more direct comparison to the *BeppoSAX* results only minimally increases the upper limit on the reflection fraction: $f = 0.01^{+0.07}_{-0.01}$. “Pexriv” is not able to simultaneously constrain the ionization parameter and reflection fraction, and so we regard results from this model cautiously. Indeed, based on the very low inner accretion disk temperatures measured by McClintock et al. (2001a) and Frontera et al. (2001) – $kT \simeq 24$ eV and $kT = 32 - 52$ eV, respectively – we expect a largely

neutral accretion disk and therefore “pexrav” may be a more appropriate model. Fits made with the CDID model were able to constrain the parameters simultaneously, and indicate very little (if any) reflection component from a neutral accretion disk ($\xi = 11.3 \pm 0.1$, $R < 0.005$), in good agreement with expectations based on the accretion disk temperature.

A flaring geometry for XTE J1118+480 like that described by Merloni et al. (2000) is partially supported by our results. Beloborodov (1999) examined the effects of irradiating sources with large bulk velocity on the strength of X-ray reflection. Such a scenario might arise if a magnetically-active corona above an accretion disk is producing flares, and the flares are pushed away from the disk (e.g., by the radiation pressure from reprocessed radiation). For the measured inclination of XTE J1118+480 ($i = 81$ degrees), there is no bulk velocity ($\beta = 0 - 1$, $\beta = v/c$) which can explain a reflection fraction as small as the one we measure. However, it is possible that flaring of the kind described by Merloni et al. (2000) at large scale heights, especially if the flares have a bulk velocity, might produce a very small reflection fraction.

The effects of an inner ADAF geometry might also diminish the strength of reflected features. McClintock et al. (2001a) and Esin et al. (2001) find ADAF/disc transition radii of $R_{tr} \geq 35 R_{Schw.}$ and $R_{tr} \geq 55 R_{Schw.}$, respectively. The degree to which reflection is diminished due to an inner ADAF can be addressed via fits to observations of Cygnus X-1. The model proposed by Esin et al. (1997) suggests that as the mass accretion rate falls between the “high/soft” state and “low/hard” states of black hole X-ray binaries, the inner disc may recede and be replaced by an inner ADAF. Esin et al. (1998) fit an ADAF model to these states in Cygnus X-1; in the high/soft state $R_{tr} \sim 3.5 R_{Schw.}$, and in the low/hard state $R_{tr} \geq 20 R_{Schw.}$, with a best-fit of $R_{tr} \sim 100 R_{Schw.}$. Gierlinski et al. (1999) and Gierlinski et al. (1997) fit reflection models to the high/soft and low/hard states, respectively. The angle subtended by the disc ($\Omega/2\pi$) reduces from ~ 0.6 to ~ 0.3 between these states. Thus, although an inner ADAF region of a size comparable to that reported in XTE J1118+480 reduces by half the strength of the reflected components observed in Cygnus X-1, it does not reduce the reflection to *zero*. It therefore seems unlikely

that an ADAF description of the accretion geometry in XTE J1118+480 can account for our reflection results.

If a hot, optically-thin corona partially covers the inner accretion disk, then at least a fraction of the reflected spectrum must pass through the corona along a given line of sight. Petrucci et al. (2001) examined the effects of this scenario as a function of inclination angle, assuming a corona which blankets the accretion disk. For high inclinations, the strength of the observed reflection component may be diminished considerably by the effects of Comptonization. If the corona covers the accretion disk, then Comptonization may at least partially explain the very low reflection fraction in XTE J1118+480. Such a geometry is not necessarily favored for this source, however. Fits to the *BeppoSAX* spectrum with a number of Comptonization models by Frontera et al. (2001) find that the optical depth (τ) of the corona is *lower* for a “slab” geometry than a spherical geometry. If the corona is spherical and central, and of a size similar to the ADAF geometry suggested by McClintock et al. (2001a) and Esin et al. (2001), then the effects of Comptonization on the reflection spectrum would likely be rather small. If the corona were larger and more diffuse, then a smaller optical depth might be expected for a spherical volume than for a slab geometry.

Finally, we consider the possibility that the hard, power-law X-ray flux observed in XTE J1118+480 is due primarily to synchrotron self-Comptonization in the jet observed in this source (Markoff, Falcke, & Fender 2001). As seen from such an extended emission region, the accretion disk would subtend a smaller solid angle than the geometries we consider above. Of the explanations for a small reflection fraction that we consider here, this interpretation can most easily explain why we have measured reflection fractions consistent with *zero*.

If the jets are a source of the hard X-ray flux in XTE J1118+480 as our fits may suggest, a number of interesting questions arise. Are the X-ray QPOs seen in this source (0.08 Hz; Revnivtsev, Sunyaev, & Borozdin 2000) manifested within the jet? How can the correlated X-ray and optical variability be explained? Why is XTE J1118+480 different than other GBHs, wherein non-zero reflection fractions are measured (see, e.g., Zycki, Done, & Smith 1997; Gilfanov, Churazov, & Revnivtsev

2000), and the jet does not seem to be the major source of hard X-ray flux? The answers to these questions can be partially given by studies of reflection in other GBHs, but may only be answered definitively by subsequent outbursts of XTE J11118+480 itself.

6.6 Bibliography

- Arnaud K.A., 1996, in Jacoby G., Barnes J., eds, *Astronomical Data Analysis Software and Systems V*, ASP Conference Series, 101, 17
- Beloborodov, A. M., 1999, *ApJ*, 510L, 123B
- Esin, A. A., McClintock, J. E., and Narayan, R., 1997, *ApJ*, 489, 865
- Esin, A. A., Narayan, R., Cui, W., Grove, E. J., and Zhang, S., 1998, *ApJ* 505, 854
- Esin, A. A., McClintock, J. E., Drake, J. J., Garcia, M. R., Haswell, C. A., Hynes, R. I., and Munro, M. P., 2001, *ApJ*, 555, 483
- Fender, R. P., Hjellming, R. M., Tilanus, R. J., et al., 2001, *MNRAS*, 322, L32
- Gierlinski, M., et al., 2001, *MNRAS* 288, 958
- Gierlinski, M., et al. 2001, *MNRAS* 288, 958
- George, I. M., & Fabian, A. C., 1991, *MNRAS*, 249, 352
- Frontera, F., et al., 2001, *ApJ*, in press, astro-ph/0107199
- Gierlinski, M., et al., 1997, *MNRAS*, 288, 958
- Gilfanov, M., Churazov, E., and Revnivtsev, M., 2000, *Proc. of the 5th CAS/MPG Workshop on High Energy Astrophysics*, astro-ph/0002415
- Jahoda, K., 2000, unpublished talk presented 2000 March 22 at the Rossi 2000 Symp. (Greenbelt, MD:GSFC/NASA)
- Juett, A., et al., 2002, *ApJL*, subm.
- Magdziarz, P., and Zdziarski, A. A., 1995, *MNRAS*, 273, 837
- Markoff, S., Falcke, H., and Fender, R., 2001, *A & A*, 272L, 25
- McClintock, J. E., et al., 2001a, *ApJ*, 555, 477
- McClintock, J. E., Garcia, M. R., Caldwell, N., Falco, E. E., Garnavich, P. M., and Zhao, P., 2001, *ApJ*, 551, L147
- Mitsuda, K., et al., 1984, *PASJ*, 36, 741
- Merloni, A., Di Matteo, T., and Fabian, A. C., 2000, *MNRAS*, 318, L15
- Miller, J. M., et al., 2001, *ApJ*, 546, 1055
- Miller, J. M., et al., 2002, *ApJ*, subm., astro-ph/0202083
- Narayan, R., and Yi, I., 1994, *ApJ*, 428L, 13
- Nayakshin, S., Kallman, T. R., and Kazanas, D., 2001, available at <http://lhea-www.gsfc.nasa.gov/users/serg/ms.ps>
- Patel, S. K., et al., 2001, *ApJL*, in press, astro-ph/0110182
- Petrucchi, P. O., Merloni, A., Fabian, A., Haardt, F., and Gallo, E., 2001, *MNRAS* subm., astro-ph/0108342
- Ross, R. R., & Fabian, A. C., 1993, *MNRAS*, 261, 74
- Ross, R. R., Fabian, A. C., & Young, A. J., 1999, *MNRAS*, 306, 461
- Wagner, R. M., Foltz, C. S., Shahbaz, T., Casares, J., Charles, P. A., Starrfield, S. G., and Hewett, P., 2001, *ApJ*, 556, 42
- Zdziarski, A. A., Poutanen, J., Mikolajewska, J., Gierlinski, M., Ebisawa, K., and Johnson, W. N., 1998, *MNRAS*, 301, 435
- Zycki, P. T., Done, C., and Smith, D. A., 1997, *ApJ*, 488, L113

Chapter 7

Resolving the Composite Fe $K\alpha$ Line in the Galactic Black Hole Cygnus X-1 with *Chandra*

This chapter is based on the original paper:

“Resolving the Composite Fe $K\alpha$ Line in the Galactic Black Hole Cygnus X-1 with *Chandra*,” Miller, J. M., Fabian, A. C., Wijnands, R., Remillard, R. A., Woźdowski, P., Schulz, N. S., Di Matteo, T., Marshall, H. L., Canizares, C. R., Pooley, D., and Lewin, W. H. G., 2002, *The Astrophysical Journal*, in press,

with the permission of the publisher, the *The Astrophysical Journal*.

7.1 Abstract

We observed the Galactic black hole Cygnus X-1 with the *Chandra* High Energy Transmission Grating Spectrometer for 30 kiloseconds on 2001 January 4. The source was in an intermediate state, with a flux that was approximately twice that commonly observed in its persistent low/hard state. Our best-fit model for the X-ray spectrum includes narrow Gaussian emission line ($E = 6.415 \pm 0.007$ keV, FWHM = 80^{+28}_{-19} eV,

W= 16_{-2}^{+3} eV) and broad line ($E=5.82_{-0.07}^{+0.06}$ keV, FWHM= $1.9_{-0.3}^{+0.5}$ keV, W= 140_{-40}^{+70} eV) components, and a smeared edge at 7.3 ± 0.2 keV ($\tau \sim 1.0$). The broad line profile is not as strongly skewed as those observed in some Seyfert galaxies. We interpret these features in terms of an accretion disk with irradiation of the inner disk producing a broad Fe K α emission line and edge, and irradiation of the outer disk producing a narrow Fe K α emission line. The broad line is likely shaped predominantly by Doppler shifts and gravitational effects, and to a lesser degree by Compton scattering due to reflection. We discuss the underlying continuum X-ray spectrum and these line features in the context of diagnosing the accretion flow geometry in Cygnus X-1 and other Galactic black holes.

7.2 Introduction

Cygnus X-1 was the first object to be classified as an X-ray binary system, and also the first to be recognized as a black hole, via optical radial velocity measurements (Webster & Murdin, 1971; Bolton, 1972). Correlated X-ray and radio intensity variations led to the identification of “X-ray states” — periods of high X-ray intensity and spectral softness, or low X-ray intensity and spectral hardness — in Cygnus X-1 (Tananbaum et al. 1972). Since then, states have become an essential part of how Galactic black holes are discussed and understood (for reviews, see Tanaka & Lewin 1995 and Done 2001; see also Homan et al. 2001). Cygnus X-1 has been active in X-rays since its discovery, and presently is the only known persistent Galactic black hole system with a high mass companion (an O9.7 Iab supergiant; Gies et al. 1982, 1986). The black hole mass is dynamically constrained to a lower limit of $M_{BH} \geq 9.5 M_{\odot}$ (Paczynski 1974); Herrero et al. (1995) suggest that the most probable mass is $M_{BH} \geq 10.1 M_{\odot}$.

The bright, persistent nature of Cygnus X-1, its constrained inclination ($i \simeq 35^{\circ}$, Gies & Bolton 1986), modest distance (2.5 kpc, Bregman et al. 1973), and state transitions have made it a favorite source for observers and theorists. In particular, it is a testbed for models aiming to describe links between states and accretion flow

geometries, and how these are related to the mass accretion rate (\dot{m}). In general, “high/soft” states are associated with high \dot{m} , and “low/hard” states are associated with low \dot{m} . State identifications usually also rely upon fast X-ray variability analysis.

A variety of models connecting states and the accretion geometry have performed well, but two show particular promise while making very different predictions. Esin et al. (1998) have described the behavior of Cygnus X-1 in terms of an advection-dominated accretion flow (ADAF). This model predicts that when \dot{m} is relatively high, the disk may extend to the marginally stable orbit (the high/soft state). When \dot{m} is lower, the disk is recessed, and the inner region is a hot, quasi-spherical, optically-thin ADAF. In contrast, Young et al. (2001) have described the behavior of Cygnus X-1 in terms of a disk which always extends to the marginally stable orbit but with a changing surface ionization that determines the X-ray state.

Fe $K\alpha$ emission lines may trace bulk velocities, temperatures, and even strong gravitational effects. Therefore, such lines may serve as tools for placing observational constraints on accretion flow models. In some Seyfert galaxies, characteristic broad (sometimes double-peaked) Fe $K\alpha$ emission lines have demonstrated the presence of an accretion disk down to the innermost stable circular orbit around the central black hole (see, e.g. Weaver, Gelbord, & Yaqoob 2001). In Galactic black holes, line profiles are often less distinct; among these systems, the lines observed in Cygnus X-1 are among the strongest. Barr, White, and Page (1985) discovered the broad Fe $K\alpha$ line ($E=6.2$ keV, $\text{FWHM}=1.2$ keV, $W=120$ eV) in an *EXOSAT* spectrum of Cygnus X-1. This measured centroid energy was slightly lower than the neutral value of 6.40 keV (Kaastra & Mewe 1993). Because such features are broad and relatively weak compared to lines in Seyfert galaxies, one might worry that the profiles are artifacts of poor continuum models or poor instrumental response. However, an Fe $K\alpha$ line has been required to obtain statistically acceptable fits to spectra observed from Cygnus X-1 with a number of instruments, and for a variety of continuum models and source luminosities (for recent *ASCA* results, see Ebisawa et al. 1996 and Cui et al. 1998; for *BeppoSAX* results, see Di Salvo et al. 2001 and Frontera et al. 2001).

In 2000 November, Cygnus X-1 entered a high-intensity, spectrally-soft state (see,

e. g., Cui, Feng, & Ertmer 2002; Pottschmidt et al. 2002). Although short high/soft states are often seen in this source, extended high/soft states are rare, previously occurring in 1980 (Ogawara et al. 1982) and 1996 (Cui 1996). The *Chandra* High Energy Transmission Grating Spectrometer (HETGS; Canizares et al. 2002, in prep.) is uniquely suited to resolving structure within broad Fe K α lines. To test models for how accretion geometries change with source intensity (and therefore \dot{m}), we requested a *Chandra* observation of Cygnus X-1 to obtain a high-resolution spectrum in the Fe K α line region during this high intensity state. We were granted a Director’s Discretionary Time observation for this purpose and present results from that observation here.

Section 7.3 describes the instrumental configuration we used to observe Cygnus X-1. Section 7.4 details the models we used to fit the spectrum; the fit results are presented in Section 7.5. We discuss the implications of our fits for accretion flow models and compare our results on Cygnus X-1 to other Galactic black holes in Section 7.6. Finally, we summarize the main points of our work in Section 7.7. Future work will focus on the rich line spectrum below 2 keV, which has been noted in related work (Miller et al. 2001a, 2001b; see also Schulz et al. 2001, Marshall et al. 2001a), and modeling the broad-band X-ray spectrum with a variety of reflection models via simultaneous *RXTE* observations. Preliminary results from fits with the “constant-density ionized disk model” (Ross, Fabian, & Young 1999; hereafter RFY) to the 0.65–100 keV spectrum indicate an ionized accretion disk: $\log(\xi) = 3.0 - 3.5 \text{ erg cm s}^{-1}$, (where $\xi = L_X/nR^2$, ξ is the ionization parameter, L_X is the X-ray luminosity, n is the hydrogen number density, and R is radius). We also find that 40-50% of the observed X-ray flux may be reflected from the accretion disk.

7.3 Observation and Instrumental Configuration

We observed Cygnus X-1 on 2001 January 4, from 06:03:47 to 14:49:20 (UT) – a total of 32.1 ks. Near the time of our observation, the source was flaring to some of the highest intensity levels since the 1996 “high/soft” state (see Figure 7-1). We identify

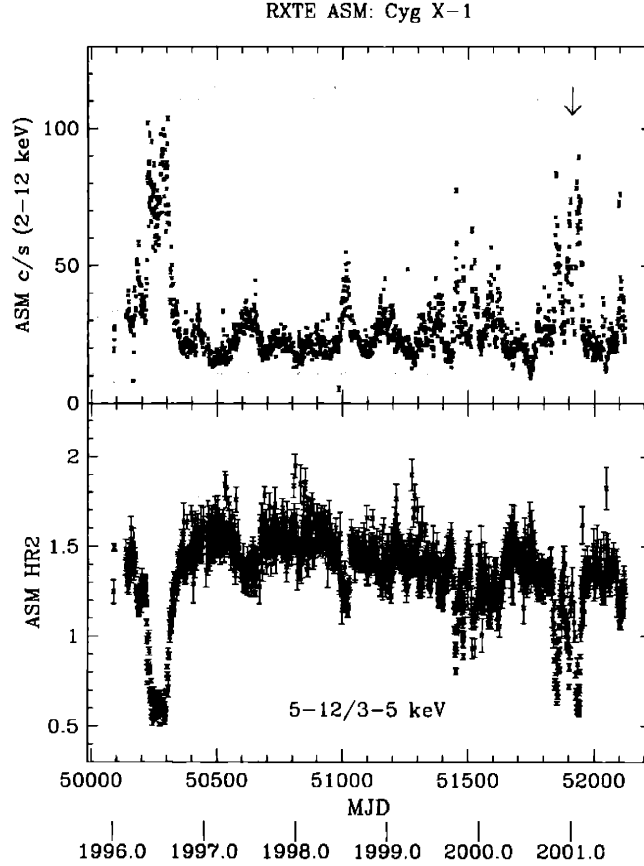


Figure 7-1 The *RXTE*/ASM lightcurve and (5-12 keV)/(3-5 keV) hardness ratio for Cygnus X-1. The curves shown here span a time interval from the start of the mission until shortly after our *Chandra* observation on 4 January 2001 (indicated by the arrow in the lightcurve). On this day, Cygnus X-1 was observed at 34 c/s with the ASM. The source was the midst of the softest, highest-intensity period observed until that point since the 1996 high/soft state.

the source state we observed as an “intermediate” state. The observatory was still slewing onto the source during the first 0.9 ks of this observation; this time span is not included for spectral analysis. A 0.5 ks dip in the X-ray lightcurve occurs 25.7 ks into this observation; during this time the count-rate drops to approximately half of the mean rate (such dips are common in Cygnus X-1; see Bałucińska-Church et al. 2000). We do not include data from within the dip for this analysis; the characteristics of the dip will be reported in a separate paper. The remaining 30.7 ks was selected for analysis. Based on the ephemeris of La Sala et al. (1998), this observation spanned a binary phase of $\phi = 0.76 - 0.82$ in the 5.6-day orbital period (with the black hole moving away from us; for a second recent ephemeris, see Brocksopp et al. 1999).

We used the HETGS to disperse the incident X-ray flux, which was read-out by the Advanced CCD Imaging Spectrometer (ACIS) spectroscopic array (ACIS-S) in continuous-clocking (CC) mode. This step was taken to reduce photon pile-up in the dispersed spectrum: the framerate in CC mode is about 2.8 ms, far less than the nominal 3.2 s in standard modes. Approximately half of the incident photons are not dispersed by the HETGS. We prevented these zeroth-order photons from being read-out with a 100-column blocking filter on the ACIS-S3 CCD. This step was taken to avoid possible telemetry saturation and dropped CCD frames. The aimpoint was moved +4 mm in the Z-direction (away from the read-out nodes) to prevent possible radiation damage to the nominal aimpoint. A Y-coordinate translation of -80 arcseconds was used to place as much of the dispersed spectrum on the ACIS-S3 CCD as possible.

At the time we conducted our analysis, the standard CIAO processing tools were unable to handle data taken in this mode. We have developed a robust set of custom processing routines. This processing method is described in detail in a paper reporting results from a *Chandra* HETGS observation of the Rapid Burster in outburst (Marshall et al. 2001b). All aspects of how the spectral grating orders and background were selected and how the data were corrected for the instrument response are as those previously reported. The only important difference between that observation and our observation of Cygnus X-1 is that the zeroth-order was blocked. The location of the zeroth order is needed to determine event wavelengths, which are a function of the dispersion distance. Without a precise measure of the location of the zeroth order, we instead use a different method to establish this relationship. We examined the locations of the neutral Si absorption edges (due to the Si-based CCDs) in opposite grating orders. In raw counts spectra, we were able to determine the zeroth order position by iterating its location until the Si edges appeared at the same wavelength in every order. This position was fine-tuned by fitting the most prominent absorption lines in opposite grating orders and requiring that the centroid wavelengths agree to within 0.05% uncertainty (0.05% is the uncertainty in the official HETGS wavelength calibration; Canizares et al. 2002, in prep.). We are confident that our wavelength

calibration is equivalent to that for standard observing modes.

We estimate that photon pile-up in our observation is negligible. Marshall et al. (2001a) report that systematic flux errors across the HETGS band are likely less than 5% in this mode. Future observations in this mode will enable better calibration and will likely make significant improvements. We find a “jump” at 2.05 keV previously seen in the spectra of bright sources observed with *Chandra* (e.g. Miller et al. 2001c; Patel et al. 2001, Juett et al. 2002). We regard this as an instrumental effect and fit it with an inverse edge ($\tau = -0.176$). We also make note of two single-bin features near 1.85 keV (6.7 Å), which are also instrumental artifacts.

7.4 Analysis

We considered the four first-order dispersed spectra for this analysis: the two High Energy Grating (HEG) and the two Medium Energy Grating (MEG) spectra on opposite sides of the zeroth order (hereafter, the +1 and −1 orders). An examination of these spectra revealed that the HEG +1 and MEG −1 orders are less affected by the spectrum dithering off the CCD array and relative CCD gain differences than their counterparts (due to the Z-coordinate translation). In characterizing the broad band spectrum, we therefore considered only these grating orders, with 5% systematic flux errors added in quadrature. We exclude data affected by chip gaps. Within these narrow energy ranges we included data from the HEG −1 and MEG +1 orders, normalized to the continuum level in the HEG +1 and MEG −1 orders.

Although we examined the spectrum at energies as low as 0.5 keV to understand how our absorption model fit the photoelectric oxygen absorption edge from the interstellar medium (ISM, see below), the MEG −1 spectrum is poorly detected below 0.65 keV. Therefore, we only fit the MEG −1 spectrum at energies above 0.65 keV. For the same reason, we only considered energies above 1.0 keV in fitting the HEG +1 spectrum. At 2.4 keV, the MEG −1 order has a chip gap, and above this energy the HEG has a higher effective area; we only consider the MEG spectra for energies below 2.4 keV. The effective upper-limit to the sensitivity of the HEG is 10.0 keV; our fits

to the HEG +1 extended to this energy.

The spectra were fit using XSPEC version 11.1.0 (Arnaud 1996). The MEG -1 and HEG +1 spectra were fit jointly, allowing an overall normalization constant to float between them (generally, the constant indicated that the normalization agreed to within 2% or better). Systematic errors were added to the flux values using the FTOOL “grppha.” Significances quoted in this paper were calculated using the F-statistic with the “ftest” task within XSPEC.

All spectral models were multiplied by a model for photoelectric absorption in the ISM, with variable elemental abundances. Local fits to the absorption edges agree with the absorption model reported in a previous *Chandra* observation of Cygnus X-1 by Schulz et al. (2001). We used the “vphabs” model in all fits with the abundances adjusted to agree with Schulz et al. (2001), with the minor distinction that we used the Verner et al. (1993) cross-sections to fit the Fe L3 edge, and that we found no evidence for the Fe L1 edge. Several components of this model should be noted: the neutral hydrogen column density is $6.21 \times 10^{21} \text{ cm}^{-2}$, oxygen is 7% under-abundant (relative to solar) and a better fit is obtained for an edge at 0.536 keV rather than the predicted 0.532 keV, iron is 25% under-abundant, neon is 11% over-abundant, and all other edges are consistent with solar values (relative to the abundances stated by Morrison & McCammon 1983; $A_{\text{Fe}}/A_{\text{H}} \simeq 3.3 \times 10^{-5}$) and expected wavelengths. These absorption values were not allowed to vary in fits to the 0.65–10.0 keV spectrum.

A wide variety of models have been used to fit the X-ray spectrum of Cygnus X-1. These range from models which attempt to describe Compton-upscattering of seed photons in a corona, to more phenomenological models. Often, these cannot be distinguished on the basis of a goodness-of-fit statistic (see, e.g., Nowak, Wilms, & Dove 2002). As an example of the former, we attempted to fit the observed 0.65–10.0 keV spectrum with the “compTT” model (Titarchuk et al. 1994). We also fit the spectrum with a model consisting of the multicolor disk blackbody (hereafter, MCD; Mitsuda et al. 1984) model and a power-law. This additive model is commonly a good fit to Galactic black hole spectra, and provides a standard for comparison to other sources. The breadth and strength of Fe $K\alpha$ line and K edge features are sufficient

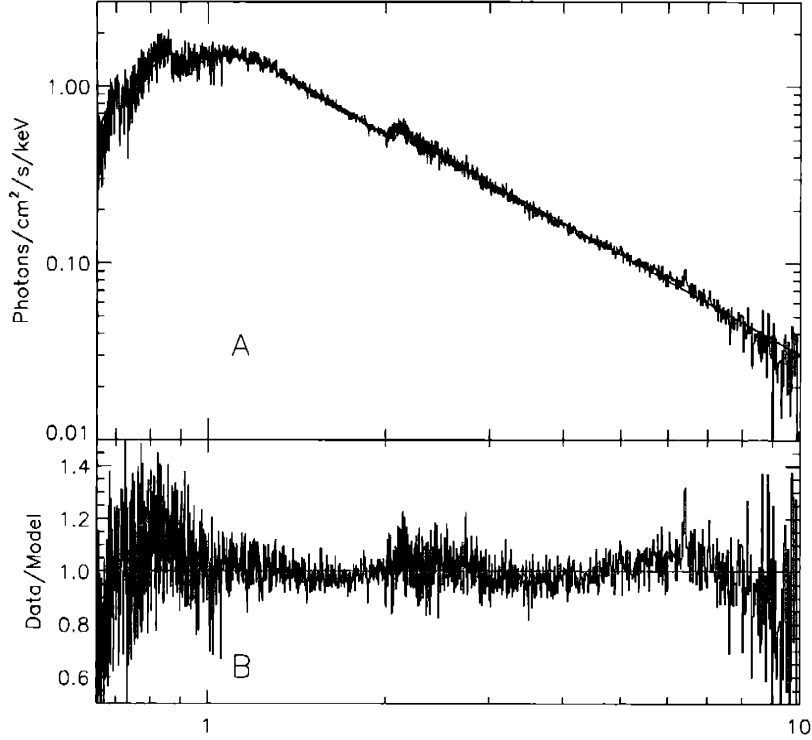


Figure 7-2 In panel A, the 0.65-10.0 keV spectrum is fit with a multicolor disk blackbody plus power-law continuum model (Model 1 in Table 7.1). The data/model ratio for this model is shown in panel B. We have suppressed a narrow instrumental feature at 1.85 keV. The notch at 2.05 keV is also an instrumental artifact. To portray the spectrum with greatest clarity, we have plotted the spectrum and ratio without errors. However, all errors are small compared to the deviations except below 0.7 keV and above 8.5 keV.

to affect fits to the underlying continuum, and so we have analyzed the continuum and Fe $K\alpha$ line region jointly.

7.5 Results

7.5.1 The Continuum Spectrum

In Figure 2, we show the results of fitting an MCD plus power-law model to the spectra (Model 1 in Table 7.1, but without a narrow Gaussian line component). A soft, thermal component is not required in some low/hard state spectra observed with other instruments. However, in this observation such a component is strongly required. In Panels A and B of Figure 7-2, structure is apparent in the Fe $K\alpha$ line

region – most notably a very narrow emission line.

Fits with the compTT model were not statistically acceptable. The seed photon temperature and electron temperature of the Compton-upscattering corona could not be constrained (errors on these parameters were several times larger than the values measured). Fitting only this model, $\chi^2/\nu > 8$ (where ν is the number of degrees of freedom in the fit). Fitting an MCD component simultaneously with compTT yielded a better but still unacceptable fit ($\chi^2/\nu > 3$). Moreover, the data/model ratio shows the same structure in the Fe $K\alpha$ line region that is seen in Panel B of Figure 7-2. Hereafter, we restrict our discussion to MCD plus power-law models. We note that compTT may still be a good description of spectra from Cygnus X-1 in different states.

In Table 7.1, we list the parameters obtained by fitting a series of MCD plus power-law models with different local models for the Fe $K\alpha$ line region. Model 1 includes a narrow Gaussian to fit the narrow line evident in Panel B of Figure 7-2 (see also Figures 7-3 and 7-4). Model 2 adds a smeared edge component (“smedge,” Ebisawa et al. 1994). Model 3 adds a Gaussian to Model 2 to fit a broad emission line. Model 4 adds the “diskline” model (Fabian et al. 1989) to Model 2 instead of a Gaussian. The diskline model explicitly takes into account the Doppler and general relativistic shifts expected for a line produced via the irradiation of an accretion disk near to a black hole.

These models yield apparently poor fits: $\chi^2/\nu \simeq 1.8$. This is due to the fact that we have not fit a model for the complex absorption spectrum below 2 keV (Miller et al. 2001a, 2001b; Schulz et al. 2001; Marshall et al. 2001b). We include this energy range because it is critical for accurately characterizing the overall continuum shape. Fitting the same models to the spectrum in the 1.8–10.0 keV band (chosen to include the instrumental jump at 2.05 keV), statistically acceptable fits are obtained: $\chi^2/\nu \simeq 0.85$ –1.15. Thus, we believe that the fits obtained on the 0.65–10.0 keV band are meaningful.

The peak color temperatures of the inner accretion disk measured via the MCD model ($kT = 0.236 \pm 0.002$ keV with Model 3) are above those which have been

measured in the low/hard state (e.g. Ebisawa et al. 1996), and below those measured in the high/soft state (e.g. Cui et al. 1998). The power-law indices we measure ($\Gamma = 1.84 \pm 0.01$ with Model 3) are similarly intermediate. Assuming a distance of 2.5 kpc to Cygnus X-1, we measure $L_X = 1.03 \pm 0.02 \times 10^{37}$ ergs/s (0.5-10.0 keV) with Model 3. This luminosity is approximately twice that commonly measured in low/hard state, but not as high as the luminosities observed during the high/soft states observed previously in 1980 and 1996. Indeed, Belloni et al. (1996) identify the activity in 1996 as an “intermediate” state based partially on a blackbody temperature of $kT = 0.36 \pm 0.01$ keV and a power-law index of $\Gamma = 2.15 \pm 0.02$ (the latter being intermediate between canonical low/hard and high/soft state values). As the spectrum and luminosity we have observed with *Chandra* are between typical low/hard and high/soft states values, we characterize this as an “intermediate” state. However we note that it is a different kind of intermediate state than described by Belloni et al. (1996) in that it is spectrally harder.

If the distance towards a source and its inclination are known, the MCD model provides a measure of the innermost extent of the accretion disk. Assuming a distance of 2.5 kpc and $i = 35^\circ$, and $M_{BH} = 10 M_\odot$, our fits indicate the inner disk may extend very close to the marginally stable circular orbit: $R_{in} = 8.7 \pm 0.2 R_g$ (where $R_g = GM_{BH}/c^2$) via Model 3. As R_{in} scales directly with the source distance in the MCD model, if the distance to Cygnus X-1 is uncertain at the 25% level the inner disk extent should have approximately the same fractional uncertainty. Errors in the inclination are less important, but non-negligible for intermediate values. Therefore, we regard the inner disk extent measured via the MCD model to be consistent with the marginally stable circular orbit for a Schwarzschild black hole ($6 R_g$) for a small range of masses near $10 M_\odot$.

Shimura and Takahara (1995) have proposed corrections to the MCD model to account for Comptonization of the inner disk flux. They suggest that $kT_{in,corrected} = kT_{MCD}/f$ and $R_{in,corrected} = f^2 \times R_{in,MCD}$; $f = 1.7$ is suggested as appropriate for Galactic black holes. If such a correction is valid, the inner disk may be somewhat larger than the marginally stable orbit in the intermediate state. Merloni, Fabian,

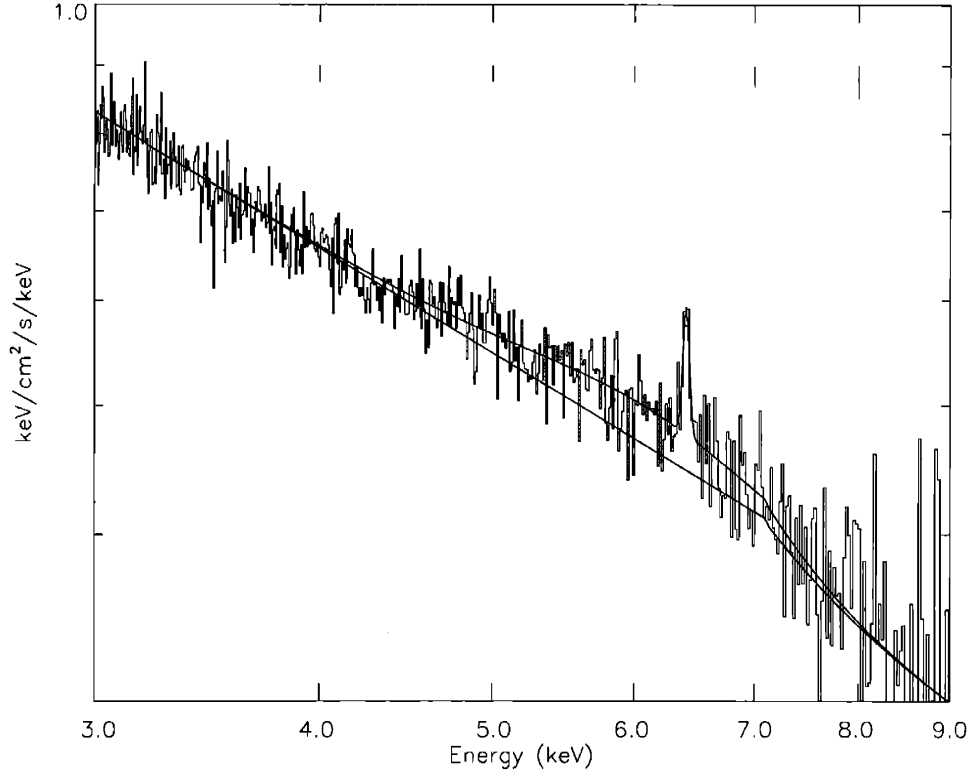


Figure 7-3 The HEG spectrum in the Fe $K\alpha$ line region at full resolution. The fit in red corresponds to Model 3 in Table 7.1 (the continuum model is that of a multicolor disk blackbody plus a power-law). The fit includes broad and narrow Gaussian line components and a smeared Fe K edge. The continuum *not* including the lines is shown by the fit in blue. Representative error bars are indicated along the top of the plot. The resolution of the HEG reveals that the Fe $K\alpha$ line in Cygnus X-1 is a composite of narrow and broad lines.

& Ross (2000) have noted that the MCD model may systematically underestimate the inner disk extent and imply a changing inner disk radius at low \dot{m} , but yield acceptable measures at relatively high \dot{m} . As we have observed Cygnus X-1 at a soft X-ray luminosity approximately twice as high as its persistent luminosity, the MCD model may give acceptable estimates of the inner disk extent. In principle, the Fe $K\alpha$ line can serve as a check on the inner accretion disk extent. The FWHM of the broad Fe $K\alpha$ line we discuss below is consistent with Keplerian velocities expected if the inner accretion disk extends near to the marginally stable circular orbit, suggesting $f \simeq 1.0$ may be more appropriate in this state than $f = 1.7$.

7.5.2 The Fe $K\alpha$ Line Region

The complexity of the Fe $K\alpha$ line region can be seen clearly via two methods. In Figure 7-3, the fit to the spectrum in the Fe $K\alpha$ line region with Model 3 is shown in detail. In Figure 7-4, we show the data/model ratio for a model which does not include components to fit the Fe $K\alpha$ line region, following the procedure that Iwasawa et al. (1996) used to represent the Fe $K\alpha$ line in MCG -6-30-15.

Relative to a model with no component to fit the narrow emission line, the narrow Gaussian included in Model 1 is significant at the 6.0σ level of confidence in the 0.65–10.0 keV band and above 8.0σ in the 1.8–10.0 keV band. The line measured via Model 1 is centered at 6.415 ± 0.007 keV; this value is fixed in Models 3 and 4. If this line were due mostly to Fe I, this centroid energy would represent a blue-shift of 560 ± 330 km/s. The FWHM width of the line varies slightly depending on the underlying continuum model, but is easily resolved with the HEG. Via Model 3, we measure a FWHM of 59^{+24}_{-14} eV, or 2800^{+1100}_{-660} km/s; a FWHM of 80^{+28}_{-19} eV, or 3700^{+1300}_{-890} km/s is obtained via Model 1. The equivalent width of the line also depends slightly on the underlying continuum: via Model 1 we obtain $W = 22 \pm 4$ eV; Model 3 gives $W = 16^{+3}_{-2}$ eV.

The apparent blue-shift of the narrow line from Fe I at 6.401 keV may be explained in terms of a line mostly comprised of Fe II, and partially comprised of species below Fe IX (Kaastra & Mewe 1993). Similarly, the measured FWHM of the line can be partially explained in these terms. Alternatively, one may want to argue that the line is due mostly to Fe I, and that the blue-shift and FWHM velocities are physical. However, the blue-shift is less than the terminal velocity expected for a type-O stellar wind (1500 km/s; Castor, Abbot, & Klein 1975); it is reasonable to assume that a neutral part of the wind must be relatively far from the ionizing flux originating near the black hole, and therefore close to terminal velocity. Moreover, the blue shift is far less than the jet velocity ($v/c > 0.6$) inferred from a spectral model by Stirling et al. (2001) in the low/hard state of Cygnus X-1. It is more likely that the shift and FWHM are partially explained by a line produced by a few moderately ionized species at a point more internal to the system.

The measured strength of the narrow Fe $K\alpha$ line is consistent with *ASCA* measurements of 10–30 eV by Ebisawa et al. (1996), made during low/hard states. Assuming solar Fe abundances, Ebisawa et al. estimated that the maximum narrow line equivalent width expected due to excitation of the companion star surface and wind is ≤ 11.1 eV. On this basis, Ebisawa et al. suggested that the narrow line was most likely due to the irradiation of the outer accretion disk. This scenario is consistent with the reflection geometry many authors have claimed in Cygnus X-1 (see, e.g., Gierlinski et al. 1997, 1999). Schulz et al. (2001) measured Fe to be 25% under-abundant in Cygnus X-1 ($A_{Fe}/A_H \simeq 3.3 \times 10^{-5}$; as per Morrison & McCammon 1983); if this under-abundance is intrinsic to the system, the maximum expected line equivalent width due to excitation of the companion wind and surface is ≤ 8.3 eV. We conclude that approximately half of the strength of the line we observe must be produced via other means. We conclude that the irradiation of the cool outer accretion disk is likely to account for the extra line strength.

Upper-limits on the strength of an Fe $K\beta$ emission line at 7.06 keV (assuming the same FWHM measured for the $K\alpha$ line) are not very constraining. The broad emission line and smeared edge both contribute at 7.06 keV, and these components may obscure a weak $K\beta$ line. The $K\beta/K\alpha$ line ratio is consistent with the expected value of 0.13.

We regard the broad Gaussian plus smeared edge of Model 3, and diskline plus smeared edge in Model 4, as approximations to a self-consistent treatment of the Doppler and GR effects expected near to a black hole, and to broadening effects expected if reflection is important. The smeared edge in Models 2, 3, and 4 has a fixed width of 7.0 keV, as observed in other Galactic black holes (see, e.g., Sobczak et al. 1999). We fix the smearing width because the energy range of Chandra is not sufficient to constrain this parameter. The edge energy is fixed at 7.11 keV (for Fe I) in Model 2, but is allowed to vary in Models 3 and 4 (edge energies of 7.3 ± 0.1 keV and 7.2 ± 0.1 keV are measured, respectively). In Model 3, the maximum optical depth is $\tau = 1.0 \pm 0.2$. The addition of the smeared edge component in Model 2 is significant at the 5.2σ level of confidence in the 0.65–10.0 keV band, and at 7.2σ in

the 1.80–10.0 keV band.

The addition of the diskline component Model 4 is only significant the 3.1σ level of confidence in the 0.65–10.0 keV band, but is significant at more than 8.0σ in the 1.80–10.0 keV band. The centroid energy measured is 5.85 ± 0.06 keV. The inclination was moderately-well constrained: $i = 40^\circ \pm 10^\circ$. We note that this measurement is broadly consistent with optical measurements of the inclination ($i = 35^\circ$, Gies & Bolton 1986, Herrero et al. 1995). Assuming an accretion disk emissivity profile with an outer line excitation radius of $1000 R_g$, the inner disk extent measured by the inner disk model is $R_{in} = 7_{-1}^{+6} R_g$. This value is consistent with the values we measured with the MCD model and consistent with the marginally stable orbit around the black hole. Note that this model does not assume a black hole mass, or a distance to the source, which are necessary to derive inner disk radii in units of R_g with the MCD model. Fits with the “Laor” model (Laor 1991) for a line produced at the inner accretion disk around a Kerr black hole did not require an inner disk edge inside the marginally stable circular orbit for a Schwarzschild black hole.

Model 3 provides a better fit to the data, using a simple Gaussian to model (see Figure 7-3) a broad Fe $K\alpha$ emission line. This Gaussian component is significant at the 4.3σ level of confidence in the 0.65–10.0 keV band, and at more than 8.0σ in the 1.80–10.0 keV band. The measured Gaussian centroid energy is $5.82_{-0.07}^{+0.06}$ keV and the FWHM is very broad: $1.9_{-0.3}^{+0.5}$ keV. The line is relatively strong: $W = 140_{-40}^{+70}$ eV, but consistent with many previous measurements of this feature. As strong Doppler shifts and gravitational red-shifts may be expected from the inner accretion disk, it is likely that this line is produced via irradiation of the inner accretion disk.

We have addressed the significance of the broad Fe $K\alpha$ emission line statistically, but an additional note is merited. One would expect that if an instrumental response error falsely creates a broad line profile, that it should be seen in all observations of bright sources made with *Chandra*. A review of the literature reveals that this is not the case. Moreover, *Chandra* observations of the Galactic black holes XTE J1550–564 at a flux of 0.6 Crab using our instrument mode (Miller et al. 2001d), and GRS 1915+105 at a flux of 0.4 Crab using a standard instrument mode (Lee et

al. 2001), do *not* reveal clear evidence for narrow or broad Fe $K\alpha$ emission lines. These facts give us additional confidence that the line we have observed is intrinsic to Cygnus X-1, and not due to the instrumental response.

The FWHM of the broad line implies Doppler shifts which are a significant fraction of c and consistent with Keplerian velocities near the marginally stable orbit around a Schwarzschild black hole. As noted above, gravitational effects may also shape the line profile. However, other effects may be important. As Fe $K\alpha$ line photons produced through disk reflection propagate through the disk and/or an ionized disk skin, they may undergo Compton scattering. Here, we estimate the degree of line broadening due to this process. The broadening per scattering is given by: $\frac{\Delta E}{E} = (\frac{2kT}{m_e c^2})^{0.5}$. The inner accretion disk color temperature we have measured with the MCD model is < 0.3 keV. RFY find that an thin ionized atmosphere above the disk in Cygnus X-1 may have a temperature of approximately $kT \sim 1.3$ keV. These values give a broadening per scatter of 3% and 7%, respectively. For an Fe $K\alpha$ line with a FWHM similar to that of the narrow line we observe, approximately 50 scattering events in a $kT \sim 1.3$ keV disk skin are required to reproduce the full width of the broad line we observe. For $\xi = 10^4$ (slightly above what we observe in Cygnus X-1 in this state), RFY find that Fe XXV has a maximum ion fraction for $\tau_{Thomson} \sim 5$, suggesting as many as ~ 25 scattering events. A hot coronal volume (with $kT \sim 30$ keV, or higher) is not expected to contribute to line broadening significantly as such volumes are likely to be optically thin. As the FWHM of the line we observe corresponds to $\Delta E/E \sim 0.3$, for a range of disk temperatures and ionized skin temperatures Compton scattering is likely to be a relatively small but non-negligible broadening mechanism compared to Doppler shifts and gravitational effects.

7.6 Discussion

A combination of an elevated source intensity, the resolution of the *Chandra* HETGS, and a ~ 30 ks exposure have allowed us to resolve the Fe $K\alpha$ line region in the X-ray spectrum of Cygnus X-1 for the first time. We clearly detect a narrow Fe $K\alpha$ emission

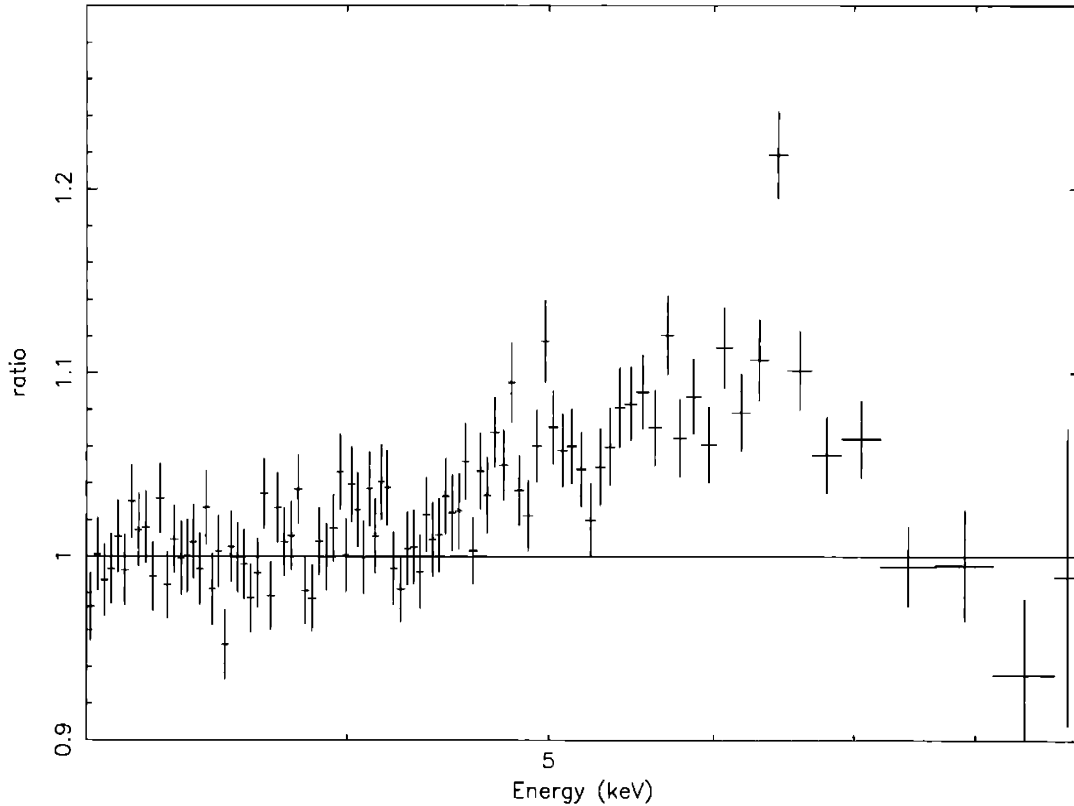


Figure 7-4 The data/model ratio of the Fe $K\alpha$ line region, rebinned by a factor of 50 for visual clarity. The spectrum was fit with a simple multicolor disk blackbody plus power-law model (see Table 7.1), but ignoring the 4.0–7.2 keV region (following Iwasawa et al. 1996 for the Seyfert galaxy MCG –6–30–15). The data/model ratio above clearly displays an iron line profile which is very similar to profiles seen in active galactic nuclei.

line, a broad Fe $K\alpha$ emission line, and a smeared Fe K edge (see Figures 7-3 and 7-4).

These features can be explained in terms of an accretion disk illuminated by a source of hard X-rays, with the broad line and edge due to irradiation of the inner accretion disk, and the narrow line due to irradiation of the outer accretion disk. This scenario is predicted by reflection models for AGNs and Galactic black holes (see, e.g., George & Fabian 1991; Ross, Fabian, & Young 1999, Nayakshin & Dove 2001). The broad components are consistent with previous observations of Cygnus X-1 (see Ebisawa et al. 1996, Cui et al. 1998, and Frontera et al. 2001, among others). The narrow line is consistent with upper-limits from *ASCA* (Ebisawa et al. 1996).

The broad emission line is broader than that reported in most previous observa-

tions of Cygnus X-1 and other Galactic black holes and may be slightly red-shifted. The broad line is not clearly double-peaked or skewed like those observed in AGNs with *ASCA* (for a review, see Weaver, Gelbord, & Yaqoob 2001; Yaqoob et al. 2002), or in an *XMM-Newton* observation of MCG -6-30-15 by Wilms et al. (2001). The broad line has a centroid energy of $E = 5.82^{+0.06}_{-0.07}$ keV, which differs significantly from Fe I at 6.40 keV. The line profile we have observed may be regarded as evidence for a line which is shifted and/or partially shaped by strong gravitational effects.

Previous observations of Cygnus X-1 with the *Chandra* HETGS have not clearly revealed similar structure in the Fe $K\alpha$ line region. Schulz et al. (2001) observed this source at a similar flux level for 15 ks (half of the exposure time we report on), though with an observing mode less suited to this work and suffering heavily from CCD pile-up, forcing the use of higher-order spectra with lower sensitivity. Cygnus X-1 was observed for 15 ks in the low/hard state, at a flux approximately half of the intensity we measured. Preliminary results have been reported by Marshall et al. (2001b). The low/hard state observation does not reveal a narrow emission line, but may show evidence for a weak, broad emission line and smeared edge. If the outer accretion disk is relatively more flared in the intermediate state than the low/hard state, this could explain why a narrow line is only detected in our observation. The lack of clearly detected lines in other *Chandra* observations of Cygnus X-1 may indicate that the line is variable. However, it is possible that long exposures in the future with well-suited instrument modes will reveal structure in the Fe $K\alpha$ line region across a range of source intensities.

Previous observations of transient Galactic black holes have also revealed evidence for broad Fe $K\alpha$ emission lines, though few are as clear as the profiles observed in Cygnus X-1. Among the sources recently observed, broad lines have been detected in XTE J1550-564 (Sobczak et al. 2000), GRO J1655-40 (Sobczak et al. 2000, Bałucińska-Church & Church 2000), GX 339-4 (Nowak, Wilms, & Dove 2002), XTE J1748-288 (Miller et al. 2001e), V4641 Sgr (in't Zand et al. 2000), and XTE J2012+381 (Campana et al. 2001). These lines have been observed in the “very high” state and in intermediate states. In both of these states, the inner accretion

disk temperature in these transient systems is relatively high: $kT = 0.7 - 1.2$ keV is common. Moreover, the inclinations of GRO J1655–40 (Greene, Bailyn, & Orosz 2001) and XTE J1550–564 (Orosz et al. 2001) are $i = 70^\circ \pm 2^\circ$ and $i = 72^\circ \pm 5^\circ$, respectively. The relatively cool inner disk we have observed in the intermediate state of Cygnus X-1 ($kT = 0.236 \pm 0.002$ keV) makes continuum flux from the disk less important in the Fe $K\alpha$ line region than in transient systems. The low inclination ($i \simeq 35^\circ$) of Cygnus X-1 may also reveal irradiation of the inner disk more clearly than transient black holes with high inclinations.

The Fe $K\alpha$ line provides an important diagnostic of the innermost extent of the accretion disk. The breadth of the line and edge we have observed — if produced at the inner accretion disk — require a disk which extends close to the marginally stable circular orbit. The line profile is consistent with the values of the inner disk extent we have measured with the MCD model. This finding supports the ionized disk model of Young et al. (2001) for X-ray states in Cygnus X-1 (for another discussion of ionized transition layers, also see Życki, Done, & Smith 2001). The inner disk extent in the intermediate state may be particularly incisive in evaluating the ADAF model. Esin et al. (1998) found that the disk may extend to the marginally stable orbit in the high/soft state of Cygnus X-1, but may have recessed to $200 R_g$ in the low/hard state. That the inner disk extent is consistent with the marginally stable orbit in this intermediate state suggests the inner disk may not recede smoothly as a function of the mass accretion rate in Cygnus X-1. In commenting on the ionized disk and ADAF models, it must be noted that within the larger set of states and behaviors observed in Cygnus X-1, this state may prove to be peculiar. Several future observations of Cygnus X-1 at high resolution are required to further evaluate these models.

7.7 Conclusions

The main results of this paper may be summarized as follows:

- We have resolved the Fe $K\alpha$ line region into a narrow line consistent with the excitation of low ion species, and a very broad emission line and edge combination.

The lines are likely produced via the irradiation of the accretion disk, with the broad line produced at the inner accretion disk and the narrow line excited at the outer accretion disk. This is consistent with models for X-ray reflection in Galactic black holes and AGNs. The broad line shape may be determined predominantly by a combination of Doppler shifts, the gravitational field of the black hole, and also by Compton scattering in the accretion disk and/or an ionized disk skin as part of the reflection process.

- Based on the accretion disk temperature, the photon power-law index, and the X-ray flux observed, we conclude that we observed Cygnus X-1 in an intermediate state.
- In this intermediate state, the MCD model suggests that the inner accretion disk extends close to the marginally stable orbit. This finding is supported by the broad Fe $K\alpha$ line and edge profiles. Thus, an inner ADAF is not required to describe this state of Cygnus X-1.
- When well-suited observational modes and long exposures are used to observe bright galactic sources, the *Chandra* HETGS is capable of resolving composite lines into components. This result holds great promise for understanding the accretion flow geometry in Galactic black holes and neutron stars via Fe $K\alpha$ line diagnostics.

Table 7.1 Models for the 0.65-10.0 keV Spectrum of Cygnus X-1

	Model 1	Model 2	Model 3	Model 4
(MCD ^a)				
kT (keV)	0.240(3)	0.241(2)	0.236(2)	0.239(2)
Norm. (10^5)	2.04(8)	1.99(7)	2.14(9)	2.07(7)
R_{in} (R_g)	8.5(2)	8.4(2)	8.7(2)	8.5(2)
Flux (10^{-8} cgs)	0.36(1)	0.36(1)	0.35(1)	0.36(1)
(Power-law)				
Γ	1.789(9)	1.78(1)	1.84(2)	1.80(1)
Norm.	2.009(9)	1.98(2)	2.09(2)	2.03(2)
Flux (10^{-8} cgs)	1.040(5)	1.014(8)	1.04(1)	1.03(1)
L_x (10^{37} cgs)	1.05(2)	1.03(2)	1.03(2)	1.04(2)
(Narrow Line)				
E (keV)	6.415(7)	$6.415^{+0.007}_{-0.003}$	6.415	6.415
σ (eV)	34^{+12}_{-8}	36^{+6}_{-11}	25^{+10}_{-6}	30(6)
W (eV)	22(4)	20(4)	16^{+3}_{-2}	22(3)
Norm. (10^{-3})	1.6(3)	$1.6^{+0.2}_{-0.1}$	1.2(3)	1.6(2)
Flux (10^{-11} cgs)	1.7(3)	$1.7^{+0.2}_{-0.4}$	1.2(3)	1.7(2)
(Broad Line)				
E (keV)	—	—	(Gaussian) $5.82^{+0.06}_{-0.07}$	(Diskline ^c) 5.85(6)
σ (keV)	—	—	$0.8^{+0.2}_{-0.1}$	—
W (eV)	—	—	140^{+70}_{-40}	60^{+12}_{-6}
Norm. (10^{-3} cgs)	—	—	12^{+6}_{-3}	$4.5^{+0.9}_{-0.4}$
Flux (10^{-11} cgs)	—	—	12^{+6}_{-3}	$4.0^{+0.8}_{-0.4}$
R_{in} (R_g)	—	—	—	7^{+6}_{-1}
i (degrees)	—	—	—	40(10)
(Smeared Edge)				
E (keV)	—	7.11	7.3(2)	7.2(1)
τ	—	1.5(3)	1.0(2)	1.2(2)
(1.80–10.0 keV)				
χ^2	1176.94	1130.69	1104.20	1114.45
d.o.f.	1293	1292	1289	1287
$P^b_{F-statistic}$	8.5×10^{-21}	6.2×10^{-13}	2.6×10^{-19}	5.0×10^{-18}
	(> 8.0 σ)	(7.2 σ)	(> 8.0 σ)	(> 8.0 σ)
(0.65–10.0 keV)				
χ^2	6576.86	6527.52	6482.62	6493.93
d.o.f.	3614	3613	3610	3608
$P^b_{F-statistic}$	2.0×10^{-9}	1.8×10^{-7}	1.6×10^{-5}	2.3×10^{-3}
	(6.0 σ)	(5.2 σ)	(4.3 σ)	(3.1 σ)

Note. — Errors on the MCD and power-law components are 90% confidence errors, and errors on line parameters are 1σ errors. Where errors are symmetric, they are indicated in parentheses. Single-digit errors reflect the error in the last significant digit. Where errors are not quoted, the parameter was fixed at the value indicated. The ISM absorption model of Schulz et al. (2001) was used in fitting the spectra. ^a We assume $i = 35^\circ$ and $d = 2.5$ kpc (see text for references). ^b P is the F-statistic probability that the improvement in the χ^2 fitting statistic is due to random fluctuations. For Model 1, P is quoted for the addition of the Gaussian model for the narrow Fe K α line to the same model with no lines. For Model 2, P relates to the addition of the smeared Fe K edge model “smedge” versus Model 1. For Models 3 and 4, P is quoted for the addition of Gaussian and “diskline” models (respectively) for the broad Fe K α line component, relative to Model 2. P was calculated using the “ftest” task within XSPEC version 11.1.0 (Arnaud 1996). Underneath each P value, the significance of the feature is indicated in parentheses. The apparently poor fits in the 0.65–10.0 keV band ($\chi^2/\nu \sim 1.80$) are due to complex absorption below 2 keV. We also quote the results of fitting these models on the 1.8–10.0 keV range, which avoids much of the absorption but allows the instrumental feature at 2.0 keV to be constrained. ^c An accretion disk emissivity profile was assumed for the diskline model.

7.8 Bibliography

- Arnaud, K. A., 1996, *Astronomical Data Analysis Software and Systems V*, eds. Jacoby G. and Barnes J., p17, ASP Conf. Series volume 101
- Bałucińska-Church, M., & Church, M. J., 2000, MNRAS, 312L, 55
- Bałucińska-Church, M., Church, M. J., Charles, P. A., Nagase, F., LaSala, J., & Barnard, R., 2000, MNRAS 311, 861
- Barr, P., White, N. E., and Page, C. G., 1985, MNRAS 216, 65
- Belloni, T., Mendez, M., van der Klis, M., Lewin, W. H. G., and van Paradijs, J., 1996, ApJ, 472, L107
- Beloborodov, A. M., 1999, ApJ, 510L, 123
- Bolton, C. T., 1972, Nature, 235, 271
- Bregman, J., Butler, D., Kemper, E., Koski, A., Kraft, R. P., & Stone, R. P. S., 1973, ApJ, 185, L117
- Brocksopp, C., et al., 1999, MNRAS, 309, 1063
- Campana, S., et al., 2001, A & A, in press, astro-ph/0112485
- Castor, J. I., Abbot, D. C., & Klein, R. I., 1975, ApJ, 195, 157
- Cui, W., 1996, IAU Circ. 6404
- Cui, W., Ebisawa, K., Dotani, T., and Kubota, A., 1998, ApJ, 493, L75
- Cui, W., Feng, Y., & Ertmer, M., 2002, ApJ, 564, 77L
- Di Salvo, T., Done, C., Życki, P. T., Burderi, L., and Robba, N. R., 2001, ApJ, 547, 1024
- Done, C., 2001, AdSpR, 28, 255
- Ebisawa, K., et al., 1994, PASJ, 46, 375
- Ebisawa, K., Ueda, Y., Inoue, H., Tanaka, Y., and White, N. E., 1996, ApJ, 497, 419
- Esin, A. A., Narayan, R., Cui, W., Grove, E. J., and Zhang, S. N., 1998, ApJ, 505, 854
- Fabian, A. C., Rees, M. J., Stella, L., and White, N. E., 1989, MNRAS, 238, 729
- Frontera, F., et al., 2001, ApJ, 546, 1027
- George, I. M., & Fabian, A. C., 1991, MNRAS, 249, 352
- Gierlinski, M., Zdziarski, A. A., Done, C., & Johnson, W. N., 1997, MNRAS, 288, 958
- Gierlinski, M., Zdziarski, A. A., Poutanen, J., Coppi, P. S., Ebisawa, K., & Johnson, W. N., 1999, MNRAS, 309, 496
- Gies, D. R., & Bolton, C. T., 1982, ApJ, 260, 240
- Gies, D. R., & Bolton, C. T., 1986, ApJ 304, 371 & 389
- Greene, J., Bailyn, C. D., & Orosz, J. A., 2001, ApJ, 554, 1290
- Herrero, A., Kudritzki, R. P., Gabler, R., Vilchez, J. M., & Gabler, A., 1995, A & A, 297, 556
- Homan, J., et al., 2001, ApJS, 132, 377
- Iwasawa, K., Fabian, A. C., Young, A. J., Inoue, H., Matsumoto, C., 1999, MNRAS 306L, 19
- Juett, A., et al., 2002, ApJL, subm.
- Kaastra, J. S., & Mewe, R., 1993, A & AS, 97, 443
- Laor, A., 1991, ApJ, 376, 90
- LaSala, J., Charles, P. A., Smith, R. A. D., Bałucińska-Church, M., & Church, M. J., 1998, MNRAS, 301, 285

- Marshall, H. L., Schulz, N. S., Fang, T., Cui, W., Canizares, C. R., Miller, J. M., & Lewin, W. H. G., 2001a, Proc. of "X-ray Emission from Accretion onto Black Holes," Eds. T. Yaqoob and J. Krolik, astro-ph/0111464
- Marshall, H. L., et al., 2001b, AJ, 122, 21
- Merloni, A., Fabian, A. C., & Ross, R. R., 2000, MNRAS, 313, 193
- Miller, J. M., et al., 2001a, AAS 198.8001
- Miller, J. M., et al., 2001b, in "X-ray Emission from Accretion onto Black Holes," eds. T. Yaqoob and J. H. Krolik, published electronically
- Miller, J. M., Ballantyne, D. R., Fabian, A. C., and Lewin, W. H. G., 2001c, MNRAS, subm., astro-ph/0111027
- Miller, J. M., et al., 2001d, MNRAS, subm., astro-ph/0103215
- Miller, J. M., et al., 2001e, ApJ, 546, 1055
- Mitsuda, K., et al., 1984, PASJ, 36, 741
- Morrison, R., & McCammon, D., 1983, ApJ, 270, 119
- Nayakshin, S., and Dove, J. B., 2001, ApJ, 560, 885
- Nowak, M. A., Wilms, J., & Dove, J. B., 2002, MNRAS, in press
- Ogawara, Y., et al., 1982, Nature, 295, 675
- Orosz, J. A., et al., 2001, ApJ, in press, astro-ph/0112101
- Paczynski, S., 1974, A & A, 34, 161
- Patel, S. K., et al., 2001, ApJL, in press, astro-ph/0110182
- Pottschmidt, K., et al., 2002, A & A, subm., astro-ph/0202258
- Ross, R. R., Fabian, A. C., & Young, A. J., 1999, MNRAS, 306, 461
- Schulz, N. S., Cui, W., Canizares, C. R., Marshall, H. L., Lee, J. C., Miller, J. M., and Lewin, W. H. G., 2001, ApJ, in press
- Shimura, T., & Takahara, F., 1995, ApJ, 445, 780
- Sobczak, G. J., McClintock, J. E., Remillard, R. A., Bailyn, C. D., & Orosz, J. A., 1999, ApJ 520, 776
- Sobczak, G. J., et al., 2000, ApJ, 544, 993
- Stirling, A. M., Spencer, R. E., de la Force, C. J., Garrett, M. A., Fender, R. P., Ogle, R. N., 2001, MNRAS, 327, 1273
- Tanaka, Y., et al., 1995, Nature, 375, 659
- Tanaka, Y., & Lewin, W. H. G., 1995, X-ray Binaries, ed. W. H. G. Lewin et al. (Cambridge: Cambridge Univ. Press), 126
- Tananbaum, H., Gursky, H., Kellogg, E., Giacconi, R., & Jones, C., 1972, ApJ, 177L, 5
- Titarchuk, L., 1994, ApJ, 434, 570
- Verner, D. A., Yakovlev, D. G., Band, I. M., & Trzhaskovskaya, M. B., 1993, At. Data Nucl. Data Tables, 55, 252
- Weaver, K., Gelbord, J., & Yaqoob, T., 2001, ApJ, 550, 261
- Webster, B. L., & Murdin, P., 1971, Nature, 250, 183
- Wilms, J., et al., 2001, MNRAS, in press, astro-ph/0110520
- Yaqoob, T., Padmanabhan, U., Dotani, T., & Nandra, K., 2001, ApJ, in press, astro-ph/0112318
- Young, A. J., Fabian, A. C., Ross, R. R., and Tanaka, Y., 2001, MNRAS, 325, 1045
- In 't Zand, J. J., M., 2000, A & A, 357, 520

Życki, P., Done, C., & Smith, D. A., 2001, MNRAS, 326, 1380

Chapter 8

Evidence of Spin and Energy Extraction in a Galactic Black Hole Candidate: The *XMM-Newton*/EPIC-pn Spectrum of XTE J1650–500

This chapter is based on the original paper:

“Evidence of Spin and Energy Extraction in a Galactic Black Hole Candidate: The *XMM-Newton*/EPIC-pn Spectrum of XTE J1650–500,” Miller, J. M., Fabian, A. C., Wijnands, R., Reynolds, C. S., Ehle, M., Freyberg, M. J., van der Klis, M., Lewin, W. H. G., Sanchez-Fernandez, C., and Castro-Tirado, A. J., 2002, *The Astrophysical Journal*, Vol. 570, p. L69,

with the permission of the publisher, *The Astrophysical Journal*.

8.1 Abstract

We observed the Galactic black hole candidate XTE J1650–500 early in its Fall, 2001 outburst with the *XMM-Newton* European Photon Imaging pn Camera (EPIC-pn). The observed spectrum is consistent with the source having been in the “very high” state. We find a broad, skewed Fe K α emission line which suggests that the primary in this system may be a Kerr black hole, and which indicates a steep disk emissivity profile that is hard to explain in terms of a standard accretion disk model. These results are quantitatively and qualitatively similar to those from an *XMM-Newton* observation of the Seyfert galaxy MCG–6-30-15. The steep emissivity in MCG–6-30-15 may be explained by the extraction and dissipation of rotational energy from a black hole with nearly-maximal angular momentum or material in the plunging region via magnetic connections to the inner accretion disk. If this process is at work in both sources, an exotic but fundamental general relativistic prediction may be confirmed across a factor of 10^6 in black hole mass. We discuss these results in terms of the accretion flow geometry in stellar-mass black holes, and the variety of enigmatic phenomena often observed in the very high state.

8.2 Introduction

The accretion flow geometry in stellar-mass black holes may change considerably with the mass accretion rate (\dot{m}). Characteristic periods of correlated intensity, energy spectral hardness, and fast variability in the X-ray band are identified as “states” (for a review, see Tanaka & Lewin 1995; see also Homan et al. 2001). These states are observed in all stellar-mass black holes, and are thought to be driven primarily by changes in \dot{m} .

Of five common states, the “very high” state is perhaps the least-understood. Often the first state observed in a transient outburst and usually very luminous, a variety of phenomena are observed that indicate a unique inner accretion flow environment. Fast quasi-periodic oscillations (QPOs; 30–450 Hz) — if tied to the

Keplerian frequency of the inner accretion disk — indicate accretion disks which extend close to the marginally stable circular orbit for a Schwarzschild black hole, and may even indicate black hole spin (e. g., Strohmayer 2001, Miller et al. 2001a). Discrete jet ejections are sometimes observed in the radio band with velocities that approach c (for a review, see Fender 2001). The X-ray energy spectra observed in the very high state are a mix of thermal and non-thermal components. The spectra suggest a disk which may extend close to the black hole, and a corona (the assumed non-thermal source) which irradiates the disk and produces a “reflection” spectrum (George & Fabian 1991; see also Gierlinski et al. 1999).

With adequate spectral resolution, Fe $K\alpha$ line profiles may provide effective tools for constraining the nature of accretion flows (e. g. Miller et al. 2002) in stellar-mass black holes. Such profiles have been used to infer black hole spin and rotational energy extraction via magnetic fields in active galactic nuclei (AGNs; Iwasawa et al. 1996, Wilms et al. 2001). Evidence for spin, based on Fe $K\alpha$ line profiles, has also been reported in stellar-mass black holes, but with gas proportional counters offering lower resolution and inhibiting stronger conclusions (Balucinska-Church & Church 2000, Miller et al. 2001b, Campana et al. 2002). The high effective area of *XMM-Newton* and short frame times available with the EPIC-pn camera are well-suited to capturing high resolution spectra of bright sources.

We were granted a target-of-opportunity observation to study the Galactic black hole candidate XTE J1650–500 (Remillard 2001) early in its Fall, 2001 outburst. Although a neutron star primary can only be ruled-out by optical radial velocity measurements, there is strong evidence in X-rays that XTE J1650–500 harbors a black hole. Based on the spectrum we obtained with *XMM-Newton* and timing properties (Wijnands, Miller, & Lewin 2001), we observed XTE J1650–500 in the very high state — the first pile-up-free CCD spectrum of a stellar-mass black hole in this state. Herein, we report the detection of a broad Fe $K\alpha$ line. We discuss the implications of this line for the accretion flow geometry in this source, and explore connections to the recent *XMM-Newton* observation of the Seyfert-I AGN MCG–6–30–15 (Wilms et al. 2001).

8.3 Observation and Data Reduction

We observed XTE J1650–500 with *XMM-Newton* on 13 September, 2001, from 15:45:25–21:41:04 (UT) for a total exposure of 21.4 ks. We did not operate the EPIC-MOS2 camera or the Optical Monitor to preserve telemetry. The EPIC-MOS1 camera was operated in timing mode but suffered a full scientific buffer nearly continuously due to the high flux. Full spectral results from the Reflection Grating Spectrometer (RGS, 0.33–2.5 keV) will be reported in a separate paper. To prevent photon pile-up, the EPIC-pn camera was operated in “burst” mode with the “thin” optical filter in place (for more information on the pn camera, see Stüder et al. 2001). Only one CCD of the pn camera is active in burst mode, and spatial information is only recorded in one dimension. Burst mode has a time resolution of 7 μ s, but a duty cycle of approximately 3%.

We extracted source counts using a box region centered on the source position (with X and Y half-widths of 1694 and 28, respectively, in DET units). Two background regions adjacent to the source position were selected. Single and double events were included for analysis. Standard pn filtering was accomplished with the procedure XMMEA_EP, assuming a source position of $16^{\circ}50'01.0''$, $-49^{\circ}57'45''$ (Castro-Tirado et al. 2001; Groot et al. 2001). We measured a source count rate of 2557.0 ± 1.9 counts s^{-1} , and a background count rate of 151.5 ± 0.5 counts s^{-1} . Calibrated event lists were custom-made at MPE using SAS-5.3 α . The source and background spectra were created with SAS-5.2.0. Spectra were grouped based both on a requirement for counts per channel (20) and on the maximum number of spectral channels sampling the pn energy resolution (3).

This is the first spectral analysis to be reported from an observation which employed burst mode. Despite the peculiarities of this mode, the instrumental effective area and the energy response, and charge transfer inefficiency (CTI) correction do not differ from more standard modes (Kirsch et al. 2002). Therefore, “full frame” mode response matrices were created to model the instrument response using SAS-5.2.0.

The spectral fits reported herein were made using XSPEC version 11.1.0 (Arnaud

1996). Quoted errors correspond to $\Delta \chi^2 = 1.0$. Below 0.5 keV and above 10.0 keV, deviations were seen in the residuals regardless of the spectral model used. We therefore restricted our analysis to the 0.5–10.0 keV band. We note a feature at 2.34 keV which appears as an emission line. The detector effective area changes sharply at this energy and the line is well-fit by a zero-width Gaussian, suggesting that the feature is instrumental.

8.4 Analysis and Results

In examining the EPIC-pn and RGS data of XTE J1650–500, we find oxygen to be $13^{+1}_{-5}\%$ under-abundant, neon to be $16^{+8}_{-6}\%$ over-abundant, and iron to be $45 \pm 5\%$ under-abundant relative to solar values along this line of sight (assuming abundances as measured by Anders & Grevesse 1989). The RGS spectrum reveals that the oxygen edge location is more consistent with 0.536 keV than the expected 0.532 keV; this has also been noted in fits to Chandra data of Cygnus X-1 (Schulz et al. 2001, Miller et al. 2002). We therefore fixed the oxygen edge to be at 0.536 keV in all fits. All other elements are found to have abundances consistent with solar values.

Absorption in the ISM was modeled using the “vphabs” model in XSPEC (with the abundance of oxygen set to zero, and an additional edge to model the oxygen absorption at 0.536 keV). We measure an effective neutral hydrogen column density of $N_H = 7.8 \pm 0.2 \times 10^{21}$ atoms cm^{-2} .

Fits with the standard multicolor accretion disk black body (hereafter, MCD; Mitusda et al. 1984) plus power-law model to the 0.5–10.0 keV spectrum were statistically unacceptable ($\chi^2 = 513.4$ for 233 d.o.f.). The data/model ratio for this model is shown in Figure 8-1. The emission line profile in this data/model ratio is similar to that observed in Cygnus X-1 with the *Chandra* High Energy Transmission Grating Spectrometer (Miller et al. 2002), and similar to line profiles seen in some AGNs with *ASCA* (see, e. g., Iwasawa et al. 1996; Weaver, Gelbord, & Yaqoob 2001).

Gaussian emission line and smeared edge (see Ebisawa et al. 1994) components were added to the model. The addition of these components improved the fit signifi-

cantly ($\chi^2 = 314.8$ for 225 d.o.f.). Using this model, we measure an inner disk color temperature of $kT = 0.322 \pm 0.004$ keV, and an MCD normalization of $3.9^{+0.3}_{-1.3} \times 10^4$. The measured power-law index is $\Gamma = 2.09^{+0.03}_{-0.09}$; the normalization of this component is measured to be 3.1 ± 0.2 ph cm $^{-2}$ s $^{-1}$ keV $^{-1}$ at 1 keV. The 0.5–10.0 keV flux of the MCD component is $0.36^{+0.03}_{-0.12} \times 10^{-8}$ erg cm $^{-2}$ s $^{-1}$, and that for the power-law component is $1.17 \pm 0.08 \times 10^{-8}$ erg cm $^{-2}$ s $^{-1}$.

The best-fit Gaussian indicates a broad line, shifted from the neutral Fe K α line energy of 6.40 keV: $E = 5.3^{+0.1}_{-0.3}$ keV, FWHM = $3.2^{+0.8}_{-0.6}$ keV, and $W = 250 \pm 50$ eV. The edge is measured to be at $E = 6.8 \pm 0.3$ keV, with a depth of $\tau = 0.5 \pm 0.1$. However, significant residuals remain in the Fe K α line region with this fit, due in part to the non-Gaussian nature of the line profile (see Figure 8-1). Moreover, on a broader energy range (one that includes the 20–30 keV “Compton hump” seen in many sources), a reflection model is often required to fit the spectra of stellar-mass black holes (see, e.g., Gierlinski et al. 1999). Broad Gaussian and smeared edge components are merely an approximation to a full reflection model in the 0.5–10.0 keV band. Therefore, we now focus on the results of fitting more sophisticated, physically-motivated reflection models. These replace the hard power-law, Gaussian, and smeared edge components discussed above.

Anticipating a highly-ionized accretion disk, we made fits with the “constant density ionized disk” reflection model (hereafter, CDID; Ross, Fabian, & Young 1999). This model measures the relative strengths of the directly-observed and reflected flux, the accretion disk ionization parameter ($\xi = L_X/nR^2$, where L_X is the X-ray luminosity, n is the hydrogen number density, and R is radius), and the photon index of the illuminating power-law flux. Fe K α line emission and line broadening due to Comptonization in an ionized disk surface layer are included in this model.

The fit obtained with this model is shown in the top panel of Figure ???. The photon index of the irradiating power law is measured to be $\Gamma = 2.08^{+0.02}_{-0.04}$. The ionization parameter is high: $\xi = 1.3^{+0.7}_{-0.1} \times 10^4$ erg cm s $^{-1}$, and the relative strength of reflected flux is measured to be $f = 0.5^{+0.7}_{-0.1}$ (where $F_{total} = F_{direct} + f \times F_{refl.}$). While the shape of the Fe K edge is reproduced by this model, the width and shape

of the Fe $K\alpha$ line is not, and a statistically-poor fit is obtained ($\chi^2 = 399.7$ for 231 d.o.f.). The ionization parameter obtained with this model corresponds to a mixture of helium-like and hydrogenic ion species of Fe (Kallman and McCray 1982).

As Doppler shifts and general relativistic smearing may be expected for lines produced in an accretion disk close to the black hole, we next made fits after convolving (or, “blurring”) the CDID model with the line element expected near a Kerr black hole. We assumed an inner disk radius of $1.24 R_g$, an outer line production radius of $400 R_g$, and an inclination of $i = 45^\circ$ (in fits with this and other models, intermediate inclinations were marginally preferred in terms of χ^2). With this blurred model, we obtained parameter constraints which differed marginally from the previous fit: $\xi = 2.5_{-0.1}^{+5.5} \times 10^4 \text{ erg cm s}^{-1}$, $f = 0.6_{-0.1}^{+0.6}$, and $\Gamma = 1.96_{-0.06}^{+0.04}$. The shape and strength of the Fe $K\alpha$ line are not fit adequately; the fit is slightly worse than the un-blurred model ($\chi^2 = 407.8$, 231 d.o.f.).

Finally, we constructed a model which allows the Fe $K\alpha$ line and reflection components to be treated separately. We fit the line with the “Laor” line model (Laor 1991), and the power-law and reflection continuum (minus the line) with the “pexriv” model (Magdziarz & Zdziarski 1995). With pexriv, $f = 1$ corresponds to a disk which intercepts half of the incident power-law flux. It should be noted that this model was also used by Wilms et al. (2001) in fits to the *XMM-Newton*/EPIC spectrum of the Seyfert galaxy MCG–6–30–15, allowing for a direct comparison. For the Laor line, we initially fixed the inner disk edge at $1.24 R_g$, the outer line production region at $400 R_g$, and the inclination at $i = 45^\circ$. The line energy, emissivity profile ($\epsilon \sim r^{-\beta}$; we fit for β), and intensity were allowed to vary. The MCD and pexriv reflection components were blurred as before.

We found that the data could not simultaneously constrain f , ξ , and the disk surface temperature with pexriv (an additional parameter for this model). We therefore fixed the ionization parameter at $\xi = 2.0 \times 10^4 \text{ erg cm s}^{-1}$, and the disk surface temperature at $kT = 1.3 \text{ keV}$ (as per Ross, Fabian, & Young 1999 in fits to Cygnus X-1, wherein a similarly low MCD disk temperature but similarly high values of ξ are reported).

The fit obtained with this model is shown in the bottom panel of Figure ??.

Statistically, this model represents a significant improvement ($\chi^2 = 319.9$ for 229 d.o.f.). A power-law index of $\Gamma = 2.04^{+0.03}_{-0.02}$ is obtained. We measure the Fe K α line to be centered at $E = 6.8^{+0.2}_{-0.1}$ keV, likely due to a blend of Fe XXV and Fe XXVI (helium-like and hydrogenic Fe) and consistent with the high ionization parameters previously measured. The line is strong, with an equivalent width of $W = 350^{+60}_{-40}$ eV and a flux of $2.2 \pm 0.3 \times 10^{-10}$ erg cm $^{-2}$ s $^{-1}$ ($3.2 \pm 0.4 \times 10^{-2}$ ph cm $^{-2}$ s $^{-1}$). When the inner disk edge is allowed to vary, an inner radius of $1.24 R_g$ (the limit of the Laor model, corresponding to $a = 0.998$) is preferred over an inner radius of $6.0 R_g$ (the marginally stable circular orbit around a Schwarzschild black hole) at the 6σ level of confidence. A steep emissivity is suggested via the Laor line model: $\beta = 5.4 \pm 0.5$. This emissivity is preferred over that for a standard accretion disk ($\beta = 3.0$) at the 5.6σ level of confidence. The pexriv reflection “fraction” is $f = 0.6^{+0.3}_{-0.1}$. This is consistent with the reflection fractions measured in the high state of Cygnus X-1 (Gierlinski et al. 1999), wherein the disk may extend to the marginally stable circular orbit.

It is not likely that these results can be explained in terms of an anomalous Fe abundance. Allowing β and A_{Fe} (in pexriv) to vary, the abundance is poorly constrained: $A_{Fe} = 1.0^{+0.5}_{-0.7}$, and the emissivity drops only slightly to $\beta = 5.0$. Fixing the emissivity at $\beta = 3.0$ and allowing the Fe abundance to vary yields a significantly worse fit ($\chi^2 = 353.1$ for 229 d.o.f.) and Fe must be more than 30 times overabundant. We note that the line strength and reflection fraction in our final fit are not strictly congruent, and that $f = 0.6^{+0.3}_{-0.1}$ is below the reflection fraction measured in MCG-6-30-15 ($f = 1.5 - 2.0$, Wilms et al. 2001) using a similar model. If we fix the $f = 1.5$ in our final model, χ^2 increases only slightly ($\chi^2 = 324.9$ for 230 d.o.f.), and the other fit parameters only change within their 1σ confidence intervals. Thus, more congruent values of f are allowed by the data.

The high χ^2 value associated with our final model could be due to unmodeled narrow spectral features, approximations in the model, and calibration issues. We note a feature at approximately 7.0 keV, which may be a narrow edge due to neutral

Fe or an Fe XXVI absorption line. Alternatively, there may be an Fe $K\beta$ emission line near 7.4 keV due to ionized Fe species, which is superimposed upon the broader smeared edge fit by the reflection models. There is also weak evidence for a narrow absorption edge feature near 9.3 keV, consistent with Fe XXVI. Modeling these features and the addition of 0.5% systematic errors below 1 keV are sufficient to make the fit acceptable.

8.5 Discussion

We have observed a broad Fe $K\alpha$ line profile in the *XMM-Newton*/EPIC-pn spectrum of the Galactic black hole candidate XTE J1650–500 in the very high state. A comparison with the broad line profile observed with *Chandra* in Cygnus X-1 is shown in Figure 8-1. That such profiles are observed in very different systems, strongly suggests that broad Fe $K\alpha$ lines in stellar-mass black holes stem from a common process. Like the broad lines observed in some Seyfert AGNs, these lines are likely produced by irradiation of the inner disk.

The Fe $K\alpha$ line we have observed in XTE J1650–500 suggests a Kerr black hole with near-maximal angular momentum ($a = 0.998$). The accretion disk emissivity profile measured with the Laor line model is inconsistent with the energy dissipation expected for standard disks. These results are very similar to those reported by Wilms et al. (2001) using the same line and reflection models for the broad Fe $K\alpha$ line observed in an *XMM-Newton*/EPIC-pn spectrum of the Seyfert galaxy MCG–6-30-15 ($E = 6.97_{-0.10}^{\text{keV}}$, $W \sim 300\text{--}400 \text{ eV}$, $f = 1.5 - 2$, $\beta \sim 4.3\text{--}5.0$). Those authors suggest that rotational energy extraction from the spinning black hole (Blandford & Znajek 1977) or material in the plunging region (Agol & Krolik 2000) may infuse the inner accretion disk with extra energy via magnetic connections, creating the steep emissivity profile indicated by the Fe $K\alpha$ line. It is possible that rotational energy extraction may be at work in XTE J1650–500 as well. If so, a fundamental general relativistic prediction may be confirmed across a factor of roughly 10^6 in black hole mass.

This observation suggests a connection between the accretion geometry of stellar-mass black holes in the very high state, and that inferred in some Seyfert galaxies. This is an important step towards understanding the nature of the very high state, and the variety of exotic phenomena observed in this state. The Blandford–Znajek process is also often invoked as a means of launching jets (Blandford 2001a, 2001b; see also Fender 2001). That we have found an emissivity which might be explained by magnetic connections to the black hole or to matter in the plunging region in the very high state of XTE J1650–500 (detected at 7.5 mJy at 0.8 GHz with MOST in this state with a spectrum indicative of jets; S. Tingay, priv. comm.), suggests that the discrete radio ejections observed in some sources in this state (see Fender 2001) may be driven by rotational energy extraction.

Martocchia, Matt, & Karas (2002) have shown that a “lamp-post” reflection model may explain the steep disk emissivity implied in fits to the Fe $K\alpha$ line in MCG–6–30–15. This model assumes a source of power-law flux which illuminates the accretion disk from a location directly above the black hole. To explain $\beta \sim 4$, this model requires $f \sim 4$ — well above the values we measure. Therefore, the lamp-post model may not adequately describe the accretion geometry of XTE J1650–500.

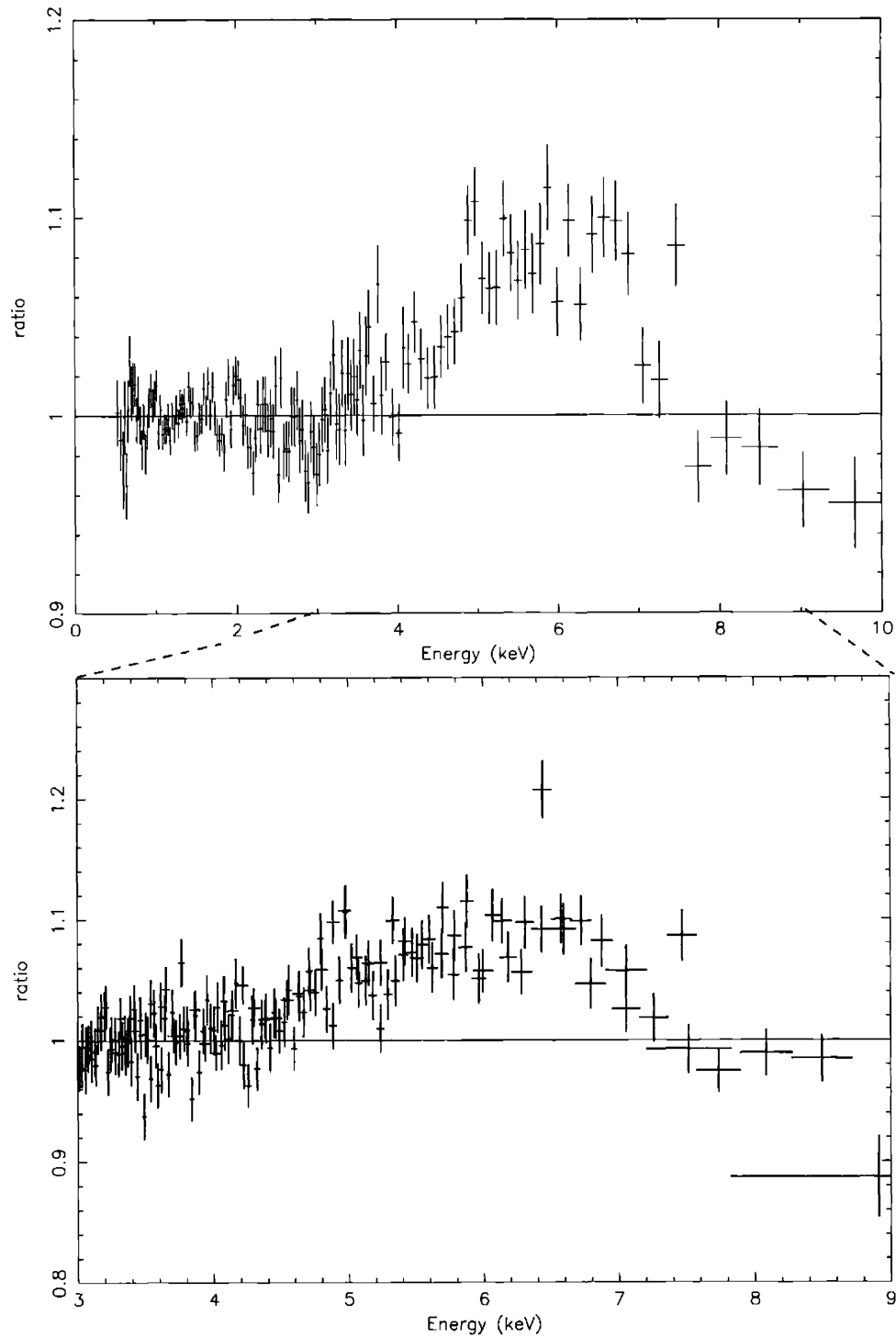


Figure 8-1 Above: The data/model ratio for a model consisting of multicolor disk blackbody and power-law components, modified by photoelectric absorption. (We have suppressed a feature at 2.34 keV; the data is fit between 0.5–10.0 keV) Below: The data/model ratio of XTE J1650–500 (in red) and that for a 30 ksec observation of Cygnus X-1 with the *Chandra* High Energy Transmission Grating Spectrometer (in blue), shown in greater detail than above. In all ratios shown above, the 4.0–7.0 keV band was ignored in fitting the model. The ratios have been rebinned for visual clarity. In both, a majority of the line profile lies below 6.40 keV, the $K\alpha$ line energy for neutral Fe.

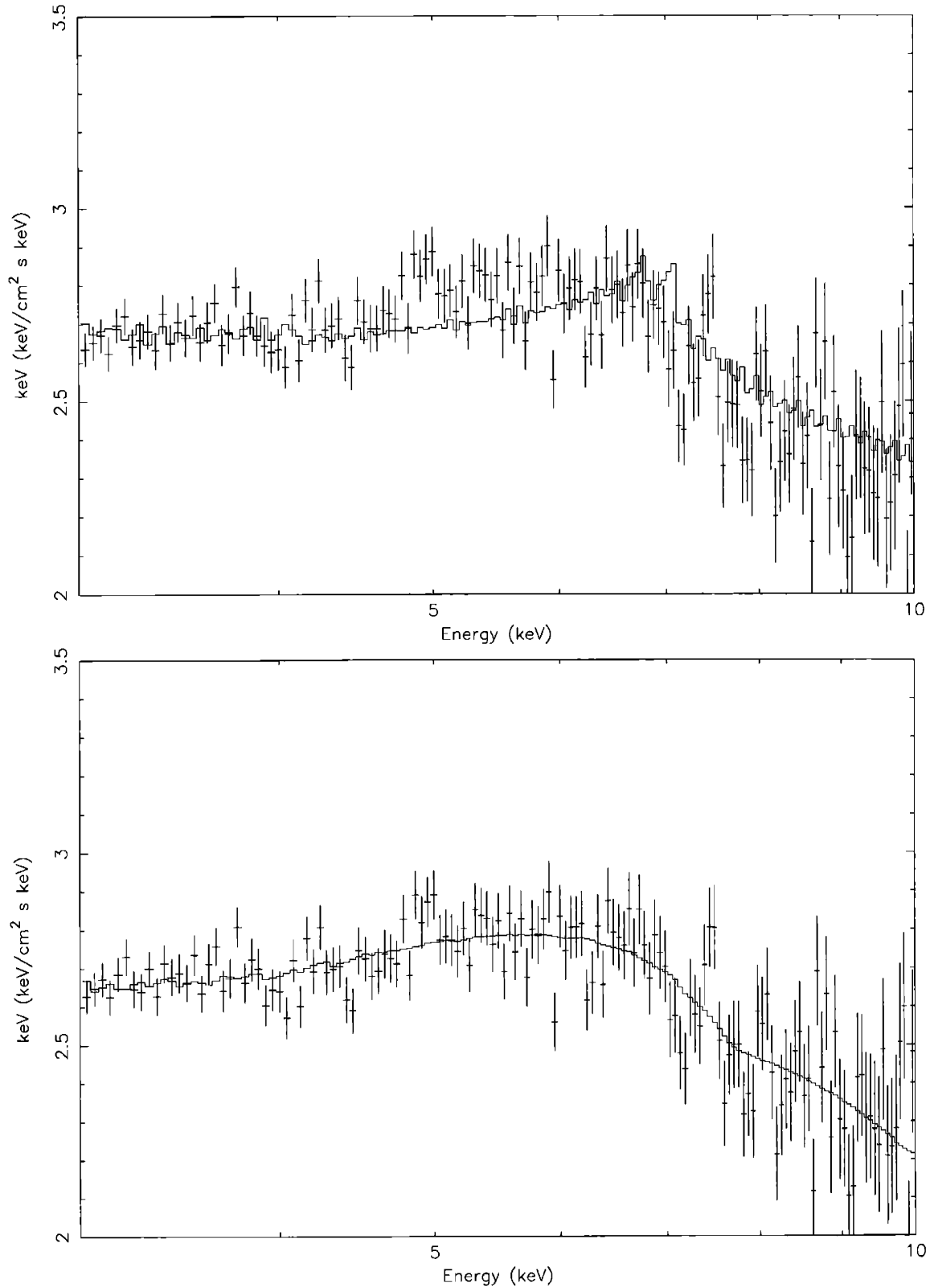


Figure 8-2 *Top*: the spectrum of XTE J1650–500 fit with a model for disk reflection (shown in red is the “constant density ionized disk” model; Ross, Fabian, & Young 1999). Clearly, the line profile is broader than is predicted with this model, indicating significant Doppler shifts and/or general relativistic skewing are required to describe the line profile. *Bottom*: The spectrum fit with the “Laor” model for line emission near a Kerr black hole (Laor 1991), and the “pexriv” reflection model (Magdziarz & Zdziarski 1995).

8.6 Bibliography

- Agol, E., & Krolik, J. H., 2000, *ApJ*, 528, 161
- Anders, E., & Grevesse, N., 1989, *GeoCoA*, 53, 197
- Arnaud, K. A., 1996, *Astronomical Data Analysis Software and Systems V*, eds. Jacoby G. and Barnes J., p17, ASP Conf. Series volume 101
- Balucinska-Church, M., & Church, M. J., 2000, *MNRAS*, 312L, 55
- Blandford, R. D., 2001a, to appear in “Particles and Fields in Radio Galaxies,” ASP Conference Series, eds. R. A. Laing and K. M. Blundell
- Blandford, R. D., 2001b, *Prog. of Th. Phys. Supplement Series*, in press
- Blandford, R. D., & Znajek, R. L., 1977, *MNRAS*, 179, 433
- Campana, S., et al., 2002, *A & A*, in press, astro-ph/0112485
- Castro-Tirado, A. J., et al., 2001, *IAU Circ.* 7707
- Ebisawa, K., et al., 1994, *PASJ*, 46, 375
- Fender, R. P., 2001, to appear in “Relativistic Flows in Astrophysics,” Springer Verlag Lecture Notes in Physics, eds. A. W. Guthmann et al.
- George, I. M., & Fabian, A. C., 1991, *MNRAS*, 249, 352
- Gierlinski, M., Zdziarski, A. A., Poutanen, J., Coppi, P. S., Ebisawa, K., and Johnson, W. N., 1999, *MNRAS* 309, 496
- Groot, P., Tingay, S., Udalski, A., & Miller, J. M., 2001, *IAU Circ.* 7708
- Homan, J., et al., 2001, *ApJ*, 132S, 377
- Iwasawa, K., Fabian, A. C., Young, A. J., Inoue, H., and Matsumoto, C., 1999, *MNRAS*, 306L, 19
- Kallman, T. R. and McCray, R., 1982, *ApJS*, 50, 263
- Kirsch, M., Kendziorra, E., Freyberg, M. J., & Edele, A., 2002, in “New Visions on the X-ray Universe in the XMM-Newton and Chandra Era”, Noordwijk, ESA SP-488
- Laor, A., 1991, *ApJ*, 376, 90
- Magdziarz, P., & Zdziarski, A. A., 1995, *MNRAS*, 273, 837
- Martocchia, A., Matt, G., & Karas, V., 2002, *A & A*, subm., astro-ph/0201192
- Miller, J. M., et al., 2001a, *ApJ*, 563, 928
- Miller, J. M., et al., 2001b, *ApJ*, 546, 1055
- Miller, J. M., et al., 2002, *ApJ*, subm., astro-ph/0202083
- Mitsuda, K., et al., 1984, *PASJ*, 36, 741
- Remillard, R., 2001, *IAU Circ.* 7707
- Ross, R. R., Fabian, A. C., & Young, A. J., 1999, *MNRAS*, 306, 461
- Schulz, N. S., et al., 2001, *ApJ*, in press
- Strohmayer, T. E., 2001, *ApJ*, 552L, 49
- Stüder, L., et al., 2001, *A & A*, 365, L18
- Tanaka, Y., and Lewin, W. H. G., 1995, *X-ray Binaries*, ed. W. H. G. Lewin et al. (Cambridge: Cambridge Univ. Press)
- Weaver, K., Gelbord, J., & Yaqoob, T., 2001, *ApJ*, 550, 261
- Wijnands, R., Miller, J. M., & Lewin, W. H. G., 2001, *IAU Circ.* 7715
- Wilms, J., et al., 2001, *MNRAS*, 328, L27

Chapter 9

Conclusions

9.1 The Impact of This Work

In broad terms, the work presented in this thesis demonstrates that the inner accretion flow in GBHs may be probed in X-rays via three means: fast variability studies, broad-band continuum spectroscopy, and Fe $K\alpha$ emission line studies. These tools were employed to investigate the effects of black hole spin (the effects of a Kerr metric), similarities between solar-mass GBHs and supermassive AGNs, and the validity of prevailing models for accretion and state transitions in GBHs. Certainly, similar analyses have been undertaken previously, but this work extended the reach and application of these tools in a number of important ways.

9.1.1 General Relativistic Effects Near the Black Hole

Keplerian orbital frequencies are the fastest frequencies expected in a GBH system. When QPOs of a few $\times 100$ Hz are observed, then, it is natural to relate the oscillation with the innermost stable circular orbit. The high frequency QPOs observed in the 2000 outburst of XTE J1550–564 (Miller et al. 2001; see Chapter 3) were also seen in the 1998–1999 outburst of this source (Remillard et al. 1999; Homan, Wijnands, & van der Klis 1999, Homan et al. 2001) — this is the first example the same high frequency QPOs being observed in distinct outbursts separated by a clear quiescent

period. This finding further indicates that such QPOs trace only the most fundamental of system parameters, such as the inner extent of the accretion disk (and thereby the mass and spin of the black hole).

Moreover, there is evidence that the 276 Hz and 188 Hz QPOs in the 2000 outburst of XTE J1550–564 are present simultaneously (Miller et al. 2001; see Chapter 3). Remillard et al. (2002) found that these QPOs may be present simultaneously in the 1998–1999 outburst as well. Strohmayer (2001) reported simultaneous high frequency QPOs in the 1996 outburst of GRO J1655–40 at 450 Hz and 300 Hz. The emergence of an approximate 3:2 ratio in simultaneous high frequency QPOs may represent a resonance between General Relativistic coordinate frequencies, and trace the spin of the black hole in each system (Remillard et al. 2002; Kluzniak & Abramowicz 2002).

The Fe $K\alpha$ line profile observed in the VHS of XTE J1748–288 (see Chapter 2; Miller et al. 2001) is strongly broadened and likely also shifted to lower energies by strong gravitational effects. This profile was one of the first indications that Fe $K\alpha$ line shapes might be used to diagnose black hole spin in a manner similar to that commonly applied to Seyfert-1 AGN (Fabian et al. 2000).

The extremely broad, skewed Fe $K\alpha$ lines observed in Cygnus X-1 (Miller et al. 2002; see Chapter 7) and XTE J1650–500 (Miller et al. 2002; see Chapter 8) represent the best spectroscopic evidence for strong gravitational effects near stellar-mass black holes yet obtained. These are the first spectra of GBHs at $L_X \sim 10^{37-38}$ erg s⁻¹ (2–10 keV) obtained with CCD-based spectrometers which are *free* of photon pile-up distortions. The line profile observed in XTE J1650–500 is even more strongly skewed than that observed in Cygnus X-1: the line model applied indicates that a non-spinning black hole is ruled-out at the 6σ level of confidence.

Moreover, the Fe $K\alpha$ line in XTE J1650–500 requires a very steep inner disk emissivity profile which may be explained by rotational energy extraction from the black hole via magnetic connections to the black hole (Blandford & Znajek 1977), or by connections to matter in the plunging region (Agol & Krolik 2001). This is the first observational evidence for this General Relativistic effect in a GBH, and suggests a striking similarity to the Seyfert-1 galaxy MCG-6-30-15 (Wilms et al. 2001).

Fe $K\alpha$ line profiles are particularly appealing diagnostics. Whereas QPOs appear and disappear on the timescale of days (e.g., XTE J1550–564, Miller et al. 2001), Fe $K\alpha$ lines are nearly always present in bright states of GBHs (Sobczak et al. 1999; Sobczak et al. 2000; Miller et al. 2001). The *Chandra* and *XMM-Newton* observatories are particularly well-suited for continuing this work. Indeed, in his "Highlights of High Energy Astrophysics" review talk at the April, 2002 American Physical Society and American Astronomical Society High Energy Astrophysics Division meeting in Albuquerque, Dr. David Helfand noted the line profiles in Cygnus X-1 and XTE J1650–500 as evidence that General Relativity can be probed effectively in these accessible Galactic systems.

9.1.2 Galactic Black Hole Accretion Flow Geometry

Homan et al. (2001) noted that in the 1998–1999 outburst of the GBH XTE J1550–564, the soft X-ray luminosity (tracing \dot{m}) and spectral hardness (tracing the X-ray state) are not directly related. Spectrally soft states — thought to indicate a relatively high \dot{m} — were sometimes observed at relatively low X-ray luminosities, and vice-versa, counter to predictions (Esin, McClintock, & Narayan 1997). Similar behavior was noted by Wijnands & Miller (2002) in the 2001 outburst of the GBH candidate SAX J1711.6–3808. The work in this thesis demonstrates in more detailed ways that simple models for state transitions and changes in the accretion flow geometry with \dot{m} are likely inadequate (although they are important starting points).

To date, the Fe $K\alpha$ line plus reflection models fit to spectra from the 1998 outburst of XTE J1748–288 remains the only systematic effort to apply such a model to a full GBH outburst (Miller et al. 2001; see Chapter 2). Moreover, this work demonstrated that Fe $K\alpha$ line profiles may require a cool disk which remains close to the black hole rather than a recessed disk (as per ADAF models) in low-luminosity states.

When luminosity of the persistent GBH candidate GRS 1758–258 decreased early in 2001, the source became spectrally soft (Smith et al. 2001). This behavior is counter to that predicted by ADAF models, wherein the inner disk is replaced by a hot, quasi-spherical, optically-thin flow (producing a hard spectrum) at low lumi-

nosities (low \dot{m}). Grating-resolution spectroscopy with *XMM-Newton* (Miller et al. 2002; see Chapter 5) confirmed that the low-luminosity emission was likely due to an optically-thick accretion disk. Moreover, the inner disk radius was found to be broadly consistent with the marginally stable circular orbit.

Similarly, fits with reflection models suggest that a simple ADAF model does not describe the accretion flow geometry in the 2000 outburst of XTE J1118+480 (Miller et al. 2002; McClintock et al. 2001; see Chapter 7). In other systems in which an inner advective region is implied at low luminosity (e.g. Cygnus X-1, Gierlinski et al. 1997), significant reflection is measured. The absence of measurable reflection in XTE J1118+480 (Miller et al. 2002) suggests a hard X-ray emission region for which an accretion disk does not subtend a large solid angle — in this case, compact radio jets may be a source of X-ray emission (Markoff, Falcke, & Fender 2001).

9.1.3 Connections Between Galactic Black Holes and AGN

Evidence for connections between black holes across the mass scale — between Galactic black holes ($M_{BH} \sim 10 M_{\odot}$) and the supermassive black holes in AGN ($M_{BH} \sim 10^6\text{--}8 M_{\odot}$) — is still scarce, but evidence is mounting slowly. Certainly, it is intriguing that the size of the radio jets observed in these systems scales with the mass (Mirabel & Rodriguez 1994). Uttley & McHardy (2000) have noted that the timing noise properties of black holes at these extremes are quite similar. The work presented in this thesis establishes other potential connections.

Most of the X-ray emission observed from AGN jets may be due to the Compton-upscattering of cosmic microwave background photons by hot electrons in the jet outflow. Yet, there are indications that X-ray emission at the base of such jets is intrinsic (e.g., M87, Marshall et al. 2001). Thus, the indications for jet-based X-ray emission in the GBH XTE J1118+480 (Miller et al. 2002, see Chapter N) may represent an important link between jet-based X-ray emission in GBHs and AGN.

The Fe K α emissions lines in XTE J1650–500 (Miller et al. 2002; see Chapter 8) and the Seyfert-1 galaxy MCG –6-30-15 (Wilms et al. 2001) bear striking similarities. This suggests a connection between the accretion flow geometry of GBHs in the VHS,

and that inferred for Seyfert-1 galaxies. The hints of rotational energy extraction from the black hole (or, matter in the plunging region inside the marginally stable orbit) suggests that the Blandford–Znajek process may act over a factor of 10^6 in black hole mass. Perhaps even more interesting is the fact that this process is cited as a means of launching relativistic jets in both GBHs and AGN; the observed similarities may indicate that both the accretion inflow and outflow processes in these systems are quite similar.

9.2 Some Possible Ways Forward

In a recent review of efforts to develop a unified picture of AGN (Elvis 2001), Martin Elvis remarked, “Stars were in a similar situation for at least 20 years (c. 1890–1911, Lawrence 1987). In fact the spectroscopic definitions of the stellar types (O B A F G K M) read quite as confusingly to outsiders as those of AGN classifications (e.g. ‘Ca II strong; Fe and other metals strong; II weaker,’ Allen 1975). We now know that the main sequence is a simple temperature progression, determined fundamentally by stellar mass. There is hope that the complexities of quasars will resolve themselves the same way.”

The situation for Galactic black holes is much the same as that for AGN presently. High-frequency QPOs, broad (skewed, in some cases) Fe $K\alpha$ lines, continuum models, and reflection models provide evidence for accretion disks extending close to the black hole in some states, but not in others. In some sources wherein a skewed Fe $K\alpha$ line indicates a spinning black hole, no QPOs are observed which support this conclusion, and vice versa. We do not understand the role of jets and outflows, or what mechanism sets v/c . It is clear that we have established a set of observational tools which allow progress; it may not be overly optimistic to expect that it is only a matter of time until the variety of sources and behaviors is understood within a coherent picture.

9.2.1 Extending Diagnostics to Lower Luminosity

Revealing the nature of accretion onto stellar-mass black holes at low \dot{m} (low L_X) will require much longer observations when sources are in this state. High-frequency QPOs, broad Fe K α lines, and reflection models require data with excellent sensitivity. At $L_X \sim 10^{35}$ erg s $^{-1}$, observations of a *few* ksec, or even *few* \times 10 ksec, do not achieve the sensitivity required to detect such features, if they are present. Although observations on the order of 100 ksec are not presently common, they are likely required to accurately diagnose the nature of accretion onto stellar-mass black holes at low luminosities.

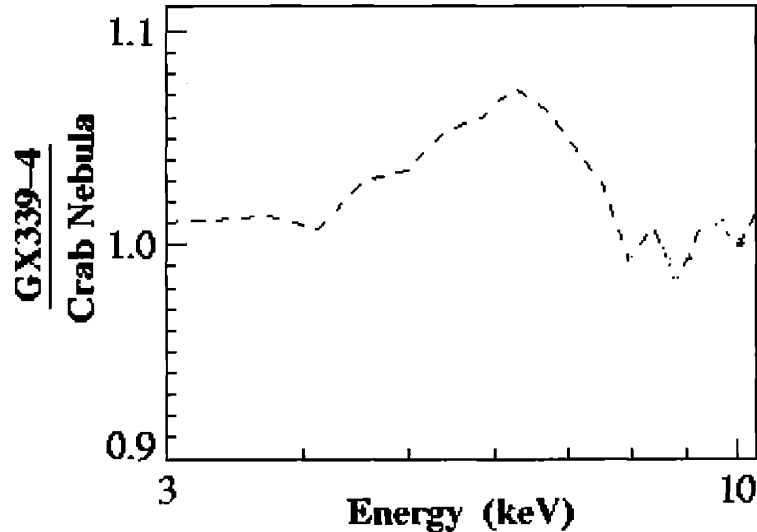


Figure 9-1 The ratio of the spectrum from the well-studied Galactic black hole candidate GX 339-4 at $L_X \sim 10^{36}$ erg s $^{-1}$ to that from the Crab nebula (Nowak, Wilms, & Dove 2002; see this work for specifics of how this data/model ratio was made). The broad Fe K α line profile — seen here at a luminosity 10 or 100 times lower than most other sources — suggests shifts consistent with a disk extending close to the black hole at this luminosity.

If broad Fe K α lines or high-frequency QPOs are detected at low luminosities, then it is likely that an accretion disk can persist at low \dot{m} and ADAF/ADIOS models may be incorrect. The detection of such features would represent strong evidence for an accretion disk at low luminosities. Recent observations of Galactic black holes at low luminosities, however, lack the sensitivity to constrain the temperature and flux of a

soft component which might be associated with an accretion disk. Therefore, strongly constraining the contribution of a disk component to the continuum flux may be the most immediate means of addressing the validity of ADAF and ADIOS models.

If such models hold for Galactic black holes at low luminosities, it may be possible to distinguish between these descriptions. Narayan & Raymond (1999) have calculated the thermal emission line strengths expected for ADAFs with outflows (similar to ADIOS models) and those without; outflowing ADAFs may have much stronger emission lines. In either case, the line fluxes are very weak, and will certainly require *few* \times 100 ksec to observe with the present generation of observatories.

Even at low luminosities — and in the absence of high-frequency QPOs and broad Fe K α emission lines — it may be possible to distinguish whether or not a given source harbors a black hole with significant spin. Medvedev and Murray (2002) suggest that low- \dot{m} flows onto a spinning black hole should display significant flux variability. For more laminar ADAF or ADIOS flows, strong flux variability is not expected.

9.2.2 High-Resolution X-ray Spectroscopy

Already, there are indications for the promise of high-resolution spectroscopy with CCD and dispersive spectrometers.

First, the nature of the corona (the region postulated to produce the hard power-law continuum) is largely unknown — its geometry, temperature, and velocity structure have only been coarsely probed using continuum models. However, features such as the Fe XXVI absorption lines seen in GRS 1915+105 (Lee et al. 2002) and XTE J1650–500 (Miller et al. 2002, see Chapter 8) may represent absorption in a hot coronal volume. Such features may be used to probe the physics of the corona. It will also be of great interest to trace the parameters of such lines across X-ray states, to probe how the corona may change.

Second, high resolution spectroscopy may be used to probe accretion disk atmospheres and outflows. The Ne IX (resonance) and Fe XVIII absorption lines seen in the high/soft state of XTE J1650–500 (see Figure 9-2, Miller et al. 2002) likely originate in a disk atmosphere. Full modeling of such spectra (for instance, assuming

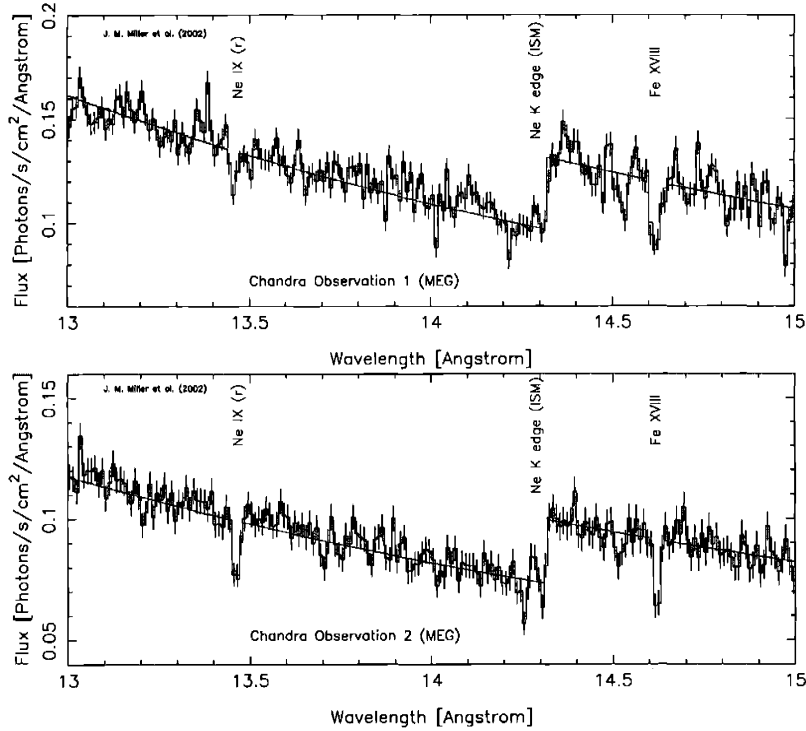


Figure 9-2 Absorption lines in the high/soft state *Chandra* spectra of XTE J1650–500 — the first such lines detected in a Galactic black hole (Miller et al. 2000). It is likely that these features represent absorption in an accretion disk atmosphere.

a gas in photo-ionization equilibrium) and a minimal set of geometric assumptions may ultimately yield an estimate of the mass in the corona and/or an outflow rate. This will be extremely important for achieving a detailed understanding of how the relative flux contributions from different structures changes across an outburst.

9.2.3 Reflection

Recent progress in modeling reflection has been rapid, and models now treat Comptonization and ionization instabilities in very sophisticated ways. It may even be possible to distinguish differences in the disk–corona geometry and interaction via such models. Two of the best models available presently are the “Constant Density Ionized Disk” (CDID) model of Ross, Fabian, & Young (1999) and the “Xion” model of Nayakshin & Kazanas (2002). Although they have only been applied to a limited number of sources at present, the promise for these models is great. The CDID

model can handle reflection from accretion disks with ionization parameters as high as $\xi = 10^5$ and above. With “Xion,” it may be possible to distinguish the reflection geometry — whether the volume irradiating the accretion disk is *a*) central and small like a lamp-post, *b*) central and quasi-spherical, or *c*) flattened and blanketing the inner accretion disk. It is interesting to note that *a* corresponds to a corona which might be the base of jet outflows, *b* corresponds to a small ADAF, and *c* corresponds to a distributed flaring structure for the corona. Thus, these new reflection models hold great promise.

9.2.4 Jet-Based X-ray Emission

Following the growing observational evidence of jet outflows in Galactic black holes obtained in radio bands, theoretical work is being undertaken to understand if jets contribute to the observed X-ray spectra. Markoff, Falcke, & Fender (2001) have suggested that synchrotron emission – likely the process causing jets to appear in the radio band – may also contribute to the hard power-law spectrum in X-rays. Memola, Fendt, & Brinkmann (2002) have suggested that jets from Galactic black holes may emit a thermal spectrum with weak line emission from Fe XXV and Fe XXVI. The predictions for line emission are qualitatively similar to the lines predicted by Narayan & Raymond (1999) for an outflowing ADAF geometry. Although contributions from jets in the X-ray band may be of theoretical interest, with present instrumentation it may be impossible to test these predictions in reasonable observing times.

9.2.5 Future X-ray Missions

The International Gamma-Ray Astrophysics Laboratory (*Integral*) is slated for launch by ESA in late 2002, and will cover the 3 keV – 10 MeV band. The imaging instrument will provide much finer resolution images than previous missions (12 arcmin FWHM) covering this band. This mission is likely to contribute to the study of Galactic black holes in two important ways. First, the corona may have a thermal or non-thermal distribution of electrons as a function of the X-ray state; if it is thermal

a break or cut-off in the hard power-law spectral slope may indicate the electron temperature of the corona. In at least one case, there is evidence that the power-law of a transient extended to 800 keV without a break (Tomsick et al. 1999). The high energy reach of *Integral* will allow more sensitive searches for power-law breaks. Second, there is speculation that electron-positron annihilation lines (at ~ 511 keV) may be produced in the inner most accretion regions of Galactic black holes, or in jet outflows, based on previous tentative detections (see, e.g., Bouchet et al. 1991, Sunyaev et al. 1992). *Integral* will provide the most sensitive coverage of the 511 keV region to date, enabling improved searches for annihilation lines.

Following the loss of Astro-E during its launch in February, 2000, a duplicate replacement observatory will be launched in 2005. Astro-E2 will simultaneously cover the 0.4–700 keV band. The major advantage of Astro-E2 will be the X-ray Spectrometer (XRS) – an X-ray calorimeter. This will provide 7 eV sensitivity in the 0.4–10 keV band. Detailed studies of structure in the Fe $K\alpha$ line band will be possible with near unity efficiency – an order of magnitude better than dispersive spectrometers (such as X-ray gratings).

Planned X-ray missions like *Constellation-X* (NASA) and the *XEUS* (ESA) will have effective areas far higher than previous missions, improved spectral resolution, and improved sensitivity. In addition, the planned energy range for *Constellation-X* extends to 60 keV, which will be sufficient to cover the “Compton hump” seen in many sources due to reflection. Two important issues remain, which will have a dramatic effect on the utility of these instruments for the study of actively-accreting stellar-mass Galactic black holes. First, it is not clear that their instrumentation will be able to support observations of bright sources. Second, the response of these instruments to transient events (specific behaviors, X-ray intensities, etc.) is certain to be longer than either *Chandra* or *XMM-Newton*.

9.3 Bibliography

- Allen, C. W., 1975, "Astrophysical Quantities" 3rd ed. (London: Athlone), 198
- Agol, E., & Krolik, J. H., 2000, *ApJ*, 528, 161
- Blandford, R. D., & Znajek, R. L., 1977, *MNRAS*, 173, 433
- Bouchet, L., et al., 1991, *ApJ*, 383L, 45
- Elvis, M., 2001, in ASP Conf. Series "Issues in the Unification of AGN", Elba, May 2001, eds. R. Maiolino, A. Marconi, and N. Nagar, astro-ph/0109513
- Esin, A. A., McClintock, J. E., & Narayan, R., 1997, *ApJ*, 489, 865
- Fabian, A. C., Iwasawa, K., Reynolds, C. S., and Young, A. J., 2000, *PASP*, 112, 1145
- Gierlinski, M., Zdziarski, A. A., Done, C., & Johnson, W. N., 1997, *MNRAS*, 288, 958
- Homan, J., Wijnands, R., & van der Klis, 1999, *IAU Circ.* 7121, 2
- Homan, J., et al., 2001, *ApJS*, 132, 377
- Kluźniak, W., and Abramowicz, M. A., 2002, astro-ph/0203314
- Lawrence, A., 1987, *PASP*, 99, 309
- Lee, J. C., et al., 2002, *ApJ*, 567, 1102
- Markoff, S., Falcke, H., and Fender, R., 2001, *A & A*, 372L, 25
- McClintock, J. E., et al., 2001, *ApJ*, 555, 477
- Medvedev, M., & Murray, N., 2002, *ApJ*, subm., astro-ph/0204254
- Memola, E., Fendt, C., and Brinkmann, W., 2002, *A & A*, in press
- Miller, J. M., et al., 2001, *ApJ*, 546, 1055
- Miller, J. M., et al., 2001, *ApJ*, 563, 928
- Miller, J. M., et al., 2002, *ApJ*, 566, 358
- Miller, J. M., Ballantyne, D. R., Fabian, A. C., & Lewin, W. H. G., 2002, *MNRAS*, in press
- Miller, J. M., et al., 2001, *ATEL* 81
- Miller, J. M., et al., 2002, *ApJ*, submitted, astro-ph/0202083
- Miller, J. M., et al., 2002, *ApJ*, 570, L69
- Mirabel, I. F., & Rodriguez, L. F., 1994, *Nature*, 371, 46
- Narayan, R., & Raymond, J., 1999, *ApJ*, 515L, 69
- Nayakshin, S., & Kazanas, D., 2002, *ApJ*, 567, 85
- Nowak, M. A., Wilms, J., & Dove, J. B., 2002, *MNRAS*, in press
- Remillard, R. A., McClintock, J. E., Sobczak, J. G., Bailyn, C. D., Orosz, J. A., Morgan, E. H., & Levine, A. M., 1999, *ApJ*, 517, L127
- Remillard, R. A., Munro, M. P., McClintock, J. E., & Orosz, J. A., 2002, *ApJ*, subm., astro-ph/0202305
- Ross, R. R., Fabian, A. C., & Young, A. J., 1999, *MNRAS*, 306, 461
- Smith, D. M., Heindl, W. A., Markwardt, C. B., & Swank, J. H., 2001, *ApJ*, 544, L41
- Sobczak, G. J., McClintock, J. E., Remillard, R. A., Bailyn, C. D., and Orosz, J. A., 1999, *ApJ*, 520, 776
- Sobczak, G. J., et al., 2000, *ApJ*, 544, 993
- Strohmayer, T. E., 2001a, *ApJ*, 552, L49
- Sunyaev, R., et al., 1992, *ApJ*, 389L, 75
- Uttley, P., & McHardy, I. M., 2000, *HEAD*, 32.0417
- Wijnands, R., & Miller, J. M., 2002, *ApJ*, 564, 974
- Wilms, J., Reynolds, C. S., Begelman, M. C., Reeves, J., Molendi, S., Staubert, R., & Kendziorra, E., 2001, *MNRAS*, 328, L27
- Winkler, C., 1995, *Exp. Astronomy*, 6, 71